Pattern Replication in Organic-Inorganic Hybrid Materials

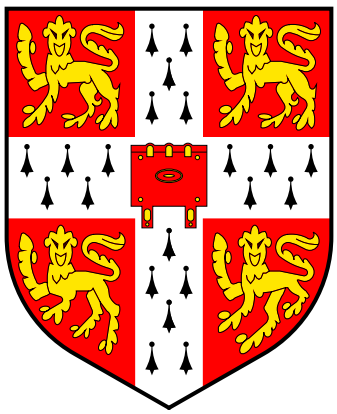

Mihaela Nedelcu

April 2008

A dissertation submitted for the degree of Doctor of Philosophy

University of Cambridge

Cavendish Laboratory

Robinson College

To my parents,
Natalia and Vasile

Declaration

This dissertation is the result of my own work and includes nothing which is the outcome of work done in collaboration except where specifically indicated in the text.

I declare that no part of this work has been submitted for a degree or other qualification at this or any other university.

This dissertation does not exceed the word limit of 60,000 words set by the Physics and Chemistry Degree Committee.

Mihaela Nedelcu, April 2008

The Summary

Pattern Replication in Organic-Inorganic Hybrid Materials

Mihaela Nedelcu

The goal of the work presented in this thesis, was to develop inorganic material systems synthesized via organic precursors and to pattern them using different lithographic techniques. The materials investigated were the ferromagnetic Ni metal and the mesoporous TiO_2 and Nb_2O_5, which have applications in dye sensitized solar cells.

The first part of the thesis presents an overview of pattern formation in organic and inorganic materials and the working principles of dye sensitized solar cells.

Next the theoretical background of block-copolymer and block-copolymer structure directing hybrid materials are described. Fundamental knowledge of magnetism and ferromagnetism are also presented. The techniques used to characterize the material and the fabricated devices are detailed. For example, the samples were characterized using magnetic force microscopy (MFM) and scanning electron microscopy (SEM), while the materials were characterized by BET.

The fabrication of Ni metal films using sol-gel process is then discussed. The Ni metal films were patterned with sub-10 nm wide lines via direct-writing electron beam lithography, and their electrical resistivity was investigated.

The influence of mesoporous TiO_2 obtained using a block-copolymer, which acted as a structure-directing agent for the metal oxide, is then presented. This material was incorporated into solid state dye sensitized solar cells. The development of a mesoporous material fabrication protocol, which has significantly influenced solar cell efficiency, is discussed.

Finally the general ideas and some preliminary results on a mesoporous Nb_2O_5 material and its application in dye sensitized solar cells are presented.

Preface

The path I have taken to becoming a doctor of Philosophy has been a very enjoyable and interesting experience. I would not have been able to produce this work without the scientific and moral support I received from various people along the way.

First of all I would like to express my gratitude to my supervisor, Prof. Ullrich Steiner, for giving me the opportunity to carry out my Ph.D. in his group. His unfailing optimism, ideas, good advice and moral support guided me throughout my project. The freedom I had during this research and his pedagogic approach enabled me to become more independent and confident in myself. Thank you Ulli!

Other people who have influenced my career and helped me to develop as a researcher include Prof. Tudor Luchian and Prof. Gheorghe Singurel from the Al. I. Cuza University of Iasi, Romania. They helped me in setting goals and encouraged me to continue my studies abroad. Thank you Tudor and Prof. Singurel!

A special mention should go to Dr. Henry Snaith from the Optoelectronics group for introducing me to the world of solar cells. Without his support, ideas, discussions and endless enthusiasm, my Ph.D. would not have been quite so successful! I would also like to thank Prof. Ulrich Wiesner, Dr. Jinwoo Lee and Chris Orilall from the Cornel University, USA, for the very successful collaboration and assistance. Thank you solar cell team !

Words of thanks go to Dr. M. S. M. Saifullah and Prof. Mark Welland from the Nanoscience Centre for discussions, help and for allowing me to use the equipment within the Nanoscience Centre. I especially want to thank Mark for also giving me the opportunity to be part of the Cambridge team in the Nanoscience - NIMS Summer Schools.

In order to perform some of the measurements, I have been helped by a number of different people. My thanks go to Dr. David Hasko for the four-point measurements and discussions about nickel films, David Anderson and Dr. Geraint Jones for the e-beam structures, Dr. Subramanian for the discussions regarding the sol-gel process, Dr. Dominik Eder from the Materials Science Department for the BET measurements and Caterina Ducati for the HRTEM images.

Many thanks also go to my groupmates Nicoleta Voicu, Edward Crossland, Rosa Poetes, Sabine Ludwigs, Katherine Thomas, Pieter wan der Wal, Mathias Kolle, Sven Huttner, David Barbero, Stefan Guldin, Urbasi Sinha and Pola Goldberg-Oppenheimer. We spent a very pleasant time together not only in the labs, but also going punting (in the rain) and having fun together. Thank you team!

I would like to acknowledge the European PolyFilm Network for the financial support and thank all the members of this network for the very successful meetings and discussions that we had.

Thank you to the Biological and Soft System Sector, in particular to Suresh

Mistry, Tracy Inman and all the secretaries we had during my research, Pete Bone, Mark Krebs, Harald Dobberstein and all the members for discussions and the fun we had. Thank you all!

I would like to thank Mihai Morariu, Stefan Harkema and Ole Gobel from the group I was part of before starting my Ph.D. at Groningen University in the Netherlands. Thank you for all your help and support!

Words of gratitude go to my friends, Iuliana and Cristi, Cristina and Cosmin, Florin, Elena, Iuliana, Florin, Liliana, Carmen, Gabriel, Adriana, Sabine, Claudia, and Angelica for always being by my side in both the good and the bad times. I would like to thank the members of the MCR Robinson College, especially Veronica Kiss, Catherine Baxter and Rachel Baker for being such nice housemates and friends. Thank you!

Finally I would like to mention my parents, they know that this thesis is dedicated to them. There are no words I can write to thank them for their unfailing support, education, and guidance. Thank you mum and dad. I could not have achieved this without you!.

Mihaela

Contents

CHAPTER 1

Introduction

The aim of this thesis was to develop inorganic material systems that can be synthesized via organic precursors and patterned by a number of lithographic techniques. These materials may be relevant for a number of technological applications: nickel is ferromagnetic, and could therefore be used in magnetic recording, whereas TiO_2 and Nb_2O_5 are semiconductors used in dye sensitized solar cells. All materials discussed in this thesis were produced using sol-gel chemistry. Starting from a sol-gel, it is possible to pattern nano-sized structures in all these materials. While nickel was patterned on the nanometer length-scale using electron beam lithography, the semiconductor materials were structured on the nanometer length-scale by the self-assembly of block-copolymer.

1.1 Patterning of Organic and Inorganic Materials

The manufacture of nano-sized structures has increased progressively in the last decade due to their applications on integrated chips, media, or energy technologies. Depending on their material properties, these devices can be made from soft (organic) or hard (inorganic) materials. The stability of a film on a substrate is the key for producing useful structures. A drop of a liquid does not always form a continuous film, but when helped by one of several coating techniques, such as spin-coating or dip-coating, a homogeneous coating can be formed. The instability of a film is called dewetting and is observed if the liquid is able to reach the thermodynamic equilibrium. This process is typically caused by the rupture of the film causing the formation of isolated drops.

A polymer film can be structured by applying external forces caused for example by an electric field [16, 24] or a temperature gradient [17, 23]. The film is sandwiched between two electrodes, one of which can be a structured electrode, and the applied electrostatic forces destabilize the film replicating the master pattern into the polymer film. Micrometer and sub-micrometer-sized structures were obtained in this way. Another successful method applied to pattern micro and nano-sized structures into a polymer film is nanoimprint lithography (NIL) [3, 5]. The structured master and the polymer film are heated above glass transition temperature of the polymer and a pressure is applied to emboss the structure into the polymer. A variation of this technique is solvent vapor assisted imprint lithography [31]. Instead of temperature annealing of the polymer, the film is swollen by exposing it to a solvent vapor. The solvent vapor lowers the glass transition temperature and the viscosity of the polymer, allowing the imprint of a mold into the polymer film at room-temperature and at low pressures. Another approach to create micrometer and sub-micrometer polymer structures is micromolding [14].

A topographically patterned rubber stamp is pressed onto a drop of a polymer solution, thereby replicating the stamp pattern.

All these systems used to pattern soft materials such as polymers, are called soft-lithography . They are cheap and easy to use. Lately, these methods have been applied to structure hard materials. An electric field can be used to pattern TiO_2 on the nanometer scale [32] while the micromolding of ceramic materials gave rise to sub-micrometer structures [8]. Micromolding was used to obtain structured epitaxially oriented lead titanate ($PbTiO_3$), extending this technique towards functionalities that cannot be achieved by using amorphous or polycrystalline materials. The ceramic materials that can be patterned with soft lithography are obtained from sol-gel solutions or polymer precursors. Other methods to fabricate ceramic materials include chemical vapor deposition (CVD), magnetron sputtering, or pulsed laser deposition (PLD). These techniques require vacuum and comparatively expensive equipment.

Mesoporous ceramic materials such as silica, TiO_2, CdSe, ZnO, etc. can be obtained by mixing metal salts with a hydrophylic-*b*-hydrophobic block copolymer that acts as structure directing agent [19, 27, 29, 34]. The block-copolymer is removed by pyrolysis at high temperatures and the oxide materials are formed.

These oxide materials can also be structured into cylinders or gyroid type structures, using the self-assembled block-copolymer morphologies as templates. By applying an electric field, the in-plane structures can be aligned normal to the substrate surface [28]. After selectively degrading one of the blocks, the required material is backfilled via electrochemical deposition into the remaining porous polymer template [6].

Sol-gel resists can be patterned using photolithography [7], focused ion beam lithography [15] or electron beam lithography [30]. The direct writing electron beam lithography provides very high resolution structures, even sub-10 nm structures can be written using this method [20 22].

1.2 History of Solar Cells

The first photovoltaic effect was seen by E. Becquerel in 1839 [1], when two electrodes immersed into an electrolytic cell were exposed to sun light. He found that certain materials give small amounts of current under sun light. The best results were obtained for the electrodes coated with AgCl, AgBr, Pt, or Ag with blue or ultraviolet light. 50 years later, the first true solar cell was constructed by C. Fritts using selenium coated with a nearly transparent layer of gold, which gave 1 % power conversion efficiency when exposed to sun light. Copper and copper oxide solar cells discovered in 1927 gave less than 1 % efficiency. R. Ohl developed solar cells with 6 % energy-conversion efficiency when used under sun light. GaAs solar cells developed in the United States have 17 % efficiency.

Since the photovoltaic effect was discovered, an enormous amount of work was focussed on developing new materials that can increase the power conversion efficiency. In 1991, the dye sensitized solar cell was discovered by O Regan and Gratzel [18] using a mesoporous TiO_2 semiconductor with a iodide/triiodide liquid electrolyte. The principle of the photovoltaic effect is that the photons that fall onto a semiconductor to create electron-hole pairs. At a junction between two different materials an electric potential difference across the interface is obtained.

A solar cell has two or more layers of a semiconductor material which absorbs the light, giving rise to electrons and holes that carry the current [25]. The cells can be made from several different semiconductor materials which can be single crystals, polycrystalline or amorphous materials. The efficiency of a solar cell, the ratio of the electrical output power to the incident sunlight, is limited by several factors: light absorption, the inability to utilize all the wavelengths of the solar spectrum, quality and type of material (crystalline, amorphous, or organic materials), carrier recombination at the junction and at interfaces, and reflection of the light from the surface.

Silicon solar cells are presently the most efficient and stable solar cells. They

were developed when it was discovered that doped silicon forms *p*-*n* junctions [10]. *p*-type silicon is doped with boron, while *n*-type silicon is doped with phosphorous. As silicon is a relatively poor light absorber, silicon-based cells require a considerable thickness, several hundreds of micrometers. These cells give an efficiency of 11-16 %, which is two-thirds of the theoretical maximum. Amorphous silicon cells have around 8 % efficiency, but their lifetime is shorter. Nevertheless, current research seeks to develop materials that can replace silicon, as silica wafers are expensive to make and the purification of silicon requires large amounts of energy.

Other materials such as $CuInSe_2$, $CuGaSe_2$, and $CuInS_2$ have been used as semiconductors in solar cell devices. They initially looked very promising, but the complexity of the material has been found to lead to complications in thin-film devices [33]. The *p*-*n* junction of thin-film solar cells based on CdTe are composed of *p*-CdTe and *n*-CdSe. At the National Renewable Laboratory, 16 % power conversion efficiency was obtained [4].

Organic or polymer based solar cells are composed of two different polymers, which have different electrical properties, to form a *p*-*n* junction. The film thickness is low, around 100 nm and the best efficiency obtained with this kind of solar cell is around 6 % [11]. The advantage of these cells is that they are inexpensive to fabricate, flexible, and that their materials can be designed on the molecular level. The disadvantage is that many of these materials are degradable upon exposure to UV light, which means their lifetime is shorter.

1.3 Dye Sensitized Solar Cells

Over recent years, with the realization of an impeding fuel shortage and the need for clean renewable sources of energy, considerable effort has been made to reduce the cost of solar cells by primarily addressing the material processing techniques. Photo-electrochemical solar cells are an emerging photovoltaic technology which

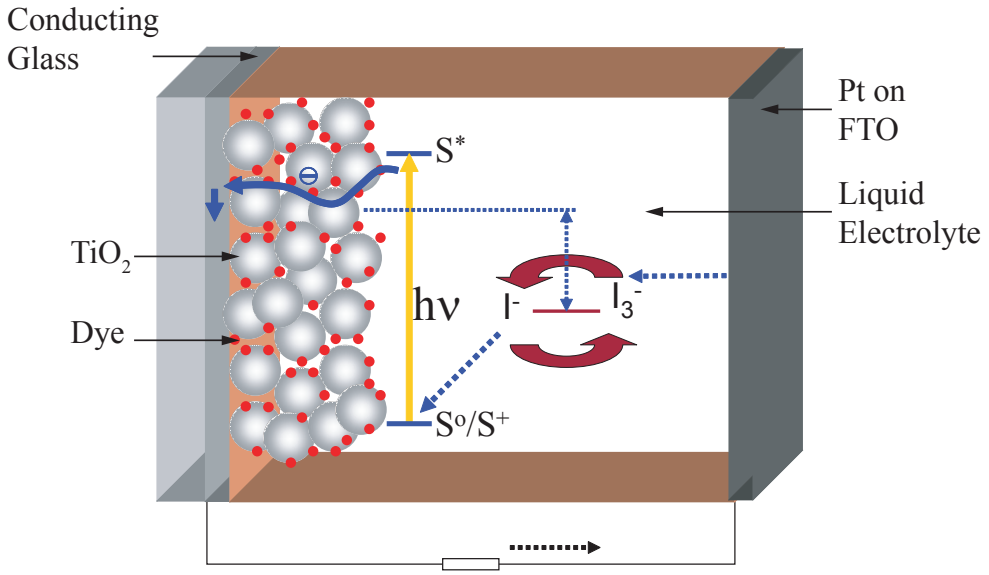

Figure 1.1: Schematic presentation of a dye sensitized solar cell with a liquid electrolyte.

could revolutionize this industry. Dye-sensitized solar cells (DSCs) invented by O Regan and Gratzel in 1991 [18], are composed of a low-cost mesoporous *n*-type metal oxide, typically TiO_2, the pigment used in some white paints. A schematic drawing of a DSC is shown in Figure 1.1

The operational principle of a DSC is as follows: a mesoporous anatase TiO_2 semiconductor oxide film prepared on a transparent and conducting substrate is sensitized with a monolayer of a dye that adsorbs to the surface of the TiO_2. The infilling with the redox-active liquid electrolyte iodide/triiodide couple and capping with a platinum counter electrode completes the device. The iodide regenerates the oxidized dye. The iodide is regenerated by the reduction of the triiodide at the counter electrode, with the holes carried back to the Pt counter electrode completing the circuit. The voltage generated under illumination corresponds to the difference between the Fermi level of the electrons in the solid and the redox potential of the electrolyte [9].

The electron transport in mesoporous TiO_2 is orders of magnitude lower than

in conventional semiconductors such as silicon [26]. The best DSCs have an efficiency of over 10 % under sun light for a 10 μm thick TiO_2 film using a volatile liquid electrolyte. Problems arise from the volatility of the electrolyte and the corrosive nature of the iodide redox couple. The critical issue for these cells is not the enhancement of the extinction coefficient of the dye, because they work efficiently in up to 20 μm thick TiO_2 layers. The critical issue is to obtain a rapid injection of electrons into TiO_2 and sufficiently fast dye regeneration. The long-term stability of DSCs is limited by the electrolyte permeability and its inertness towards the iodide, and therefore considerable research has been put into the development of materials that can replace the volatile liquid electrolyte. The most efficient approaches that can replace the volatile electrolyte are the so-called Robust liquid electrolyte that uses a non-volatile solvent [13] and an organic (polymer) hole transporter [2]

1.4 Solid-State Dye Sensitized Solar Cells

Bach *et al.* [2] showed that the organic hole transporter, 2,2 -tetrakis(N,N-di-p-methoxyphenyl-amine)-9,9 -spirobifluorene, called Spiro-MeOTAD can replace the liquid charge transporting material in so-called solid state dye sensitized solar cells. These cells have a maximum power conversion efficiency for a TiO_2 film thickness of around 2 μm. The assembly and operational principle in this case is as follows: a monolayer of dye is adsorbed onto the mesoporous semiconductor metal oxide. The organic hole conductor is spin-coated onto the device and the evaporation of silver as counter electrode closes the cell. When exposed to sun light, charge separations take place at the junction between the dye and the hole conductor. The electrons are injected into the conduction band of the semiconductor material, migrate across the mesoporous network to the anode and through an electrical circuit to the cathode. The Spiro-MeOTAD regenerates the dye and transports the positive charges to the cathode were they recombine with the electrons.

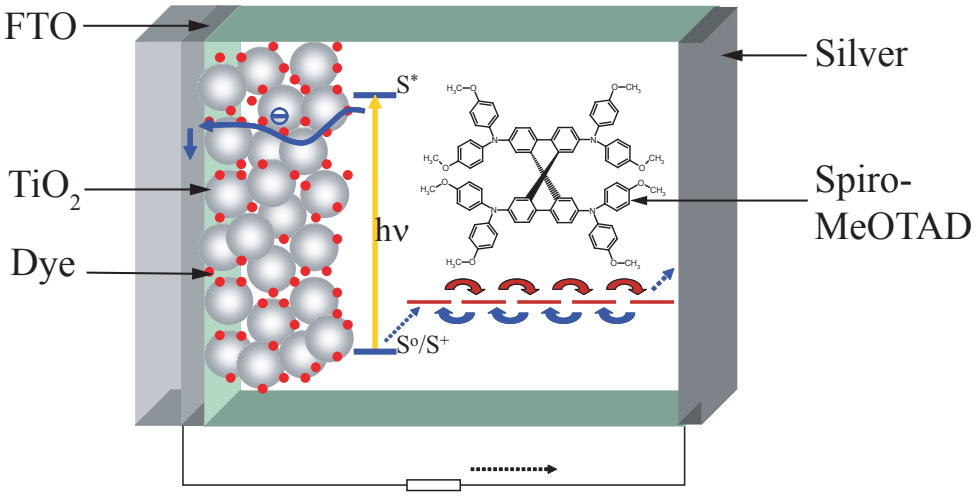

Figure 1.2: Schematic presentation of a solid state dye sensitized solar cell.

The key issues of a solid state DSC are the enhancement light absorption and the increase in pore filling with the hole transporter. Compared to liquid electrolyte DSCs, the efficiency is lower, around 5 %, because of the low hole mobility in the organic semiconductor. The lower conductivity results in a high resistance, giving rise to a voltage reduction, especially for high current densities [12]. Initially it was thought that the lower efficiency of solid state DSCs is due to the relatively fast charge recombination resulting in an electron diffusion length of only a few micrometers [26]. Further research showed that the electron diffusion length at short-circuit is between 10-20 μm, which suggests that the infiltration of the pores with the hole transporting materials causes the lower efficiency.

Dyes with a larger extinction coefficient can be used to improve the efficiency. The indoline-organic dyes, which have an extinction coefficient five times larger than conventional ruthenium-dye have been proved to enhance the performance. These dyes have 90 % absorption over the a broad spectral range, but they are not very stable for long exposure times because of a faster degradation under ultraviolet light.

Bibliography

[1] *http://www.udel.edu/igert/pvcdrom/MANUFACT/FIRST.HTM.*

[2] U. Bach, D. Lupo, P. Comte, J. E. Moser, F. Weissortel, J. Salbeck, H. Spreitzer, and M. Gratzel. Solid-state dye-sensitized mesoporous TiO_2 solar cells with high photon-to-electron conversion efficiencies. *Nature*, 395:583 585, 1998.

[3] D. R. Barbero, M. S. M. Saifullah, P. Hoffmann, H. J. Mathieu, D. Anderson, G. A. C. Jones, M. E. Welland, and U. Steiner. High resolution nanoimprinting with a robust and reusable polymer mold. *Adv. Funct. Mater.*, 17:2419 2425, 2007.

[4] J. Britt and C. Ferekides. Thin-film CdS/CdTe solar cell with 15.8 % efficiency. *Appl. Phys. Lett.*, 62:2851 2852, 1993.

[5] S. Y. Chou, P. R. Krauss, and P. J. Renstrom. Imprint of sub-25 nm vias and trenches in polymers. *Appl. Phys. Lett.*, 67:3114 3116, 1995.

[6] E. J. Crossland, S. Ludwigs, M. A. Hillmyer, and U. Steiner. Freestanding nanowires arrays from soft-etch block copolymer templates. *Soft Matter*, 3:94 98, 2007.

[7] M. Geissler and Y. Xia. Patterning pinciples and some new developments. *Adv. Mater.*, 16:1249 1269, 2004.

[8] O. F. Gobel, M. Nedelcu, and U. Steiner. Soft lithography of ceramic patters. *Adv. Funct. Mater.*, 17:1131 1136, 2007.

[9] M. Gratzel. Solar energy conversion by dye-sensitized photovoltaics cells. *Inorg. Chem*, 44:6841 6851, 2005.

[10] M. A. Green. *Crystalline silicon solar cells*. PhD thesis, University of New South Wales, Australia, 2001.

[11] J. Y. Kim, K. Lee, N. E. Coates, D. Moses, T.-Q. Nguyen, M. Dante, and A. J. Heeger. Efficient tandem polymer solar cells fabricated by all-solution processing. *Science*, 317:222 225, 2007.

[12] J. kruger. *Interface engineering in solid-state dye-sensitized solar cells*. PhD thesis, Ecole Polytechnique Federale de Lausanne, 2003.

[13] D. Kuang, S. Ito, B. Wenger, C. Klein, J.-E. Moser, R. Humphry-Baker, S. M. Zakeeruddin, and M. Gratzel. High molar extinction coefficient heteroleptic ruthenium complexes for thin film dye-sensitized solar cells. *J. Am. Chem. Soc.*, 128:4146 4154, 2006.

[14] J. R. Lawrence, G. A. Turnbull, and I. D. W. Samuel. Polymer laser fabricated by a simple micromolding process. *Appl. Phys. Lett.*, 82:4023 4025, 2003.

[15] S. Matsui and Y. Ochiai. Focused ion beam applications to solid state devices. *Nanotechnology*, 7:247 258, 1996.

[16] M. D. Morariu, N. E. Voicu, E. Schaffer, Z. Lin, T. P. Rusell, and U. Steiner. Hierarchical structure formation and pattern replication induced by an electric field. *Nat. Mater.*, 2:48 52, 2003.

[17] M. Nedelcu, M. D. Morariu, S. Harkema, N. E. Voicu, and U. Steiner. Pattern formation by temperature-gradient driven film instabilities in laterally confined geometries. *Soft Matter*, 1:62 65, 2005.

[18] B. O Regan and M. Gratzel. A low-cost, high efficiency solar based in dye-sensitized solloidal TiO_2 films. *Nature*, 353:737 739, 1991.

[19] S. M. De Paul, J. W. Zwanziger, R. Ulrich, U. Wiesner, and H. W. Spiess. Structure, mobility, and interface characterizatoion of self-organized organic-inorganic hybrid materials by solid-state NMR. *J. Am. Chem. Soc.*, 121:5725 5736, 1999.

[20] M. S. M. Saifullah, K. Kurihara, and C. J. Humphrey. Comparative study of sputtered and spin-coatable aluminium oxide electron beam resists. *J. Vac. Sci. Technol. B*, 18:2737 2744, 2000.

[21] M. S. M. Saifullah, T. Ondarcuhu, D. K. Koltsov, C. Joachim, and M. E. Welland. A reliable scheme for fabricating sub-5 nm co-planar junctions for single-molecule electronics. *Nanotechnology*, 13:659 662, 2002.

[22] M. S. M. Saifullah, K. R. V. Subramanian, D. Anderson D.-J. Kang, W. T. S. Huck, G. A. C. Jones, and M. E. Welland. Sub-10 nm high-aspect-ratio patterning of ZnO using an electron beam. *Adv. Mater.*, 17:1757 1761, 2005.

[23] E. Schaffer, S. Harkema, M. Roerdink, R. Blossey, and U. Steiner. Morphological instability of a confined polymer film in a thermal gradient. *Macromol.*, 36:1645 1655, 2003.

[24] E. Schaffer, T. Thurn-Albert, T. P. Rusell, and U. Steiner. Electrically induced structure formation and pattern transfer. *Nature*, 403:874 877, 2000.

[25] A. Shah, P. Torres, R. Tscharner, N. Wyrsch, and H. Keppner. Photovoltaic technology: The case for thin-film solar cells. *Science*, 285:692 698, 1999.

[26] H. J. Snaith and L. Schmidt-Mende. Advances in liquid-electrolyte and solid-state dye-sensitized solar cells. *Adv. Mater.*, 19:3187 3200, 2007.

[27] M. Templin, A. Franck, A. Du Chesne, H. Leist, Y. Zhang, R. Ulrich, V. Schadler, and U. Wiesner. Organically modified aluminosilicate mesostructures from block copolymer phases. *Science*, 278:1795 1798, 1997.

[28] T. Thurn-Albrecht, J. Schotter, G. A. Kastle, N. Emley, T. Shibauchi, L. Krusin-Elbaum andK. Guarini, C. T. Black, M. T. Tuominen, and T. P. Russell. Ultrahigh-densoty nanowires arrays grown in self-assembled diblock copolymer templates. *Science*, 290:2126 2129, 2000.

[29] B .Tian, X. Liu, B. Tu, C. Yu, J. Fan, L. Wang, S. Xie, G. D. Stucky, and D. Zhao. Self-adjusted synthesis of ordered stable mesoporous minerals by acid-base pairs. *Nat. Mater.*, 2:159 163, 2003.

[30] A. A. Tseng, K. Chen, C. D. Chen, and K. J. Ma. Electron beam lithography in nanoscale fabrication. Recent development. *IEEE Transactions on Electronics Packaging Manufacturing*, 26:141 149, 2003.

[31] N. E. Voicu, S. Ludwigs, E. J. W. Crossland, P. Andrew, and U. Steiner. Solvent-vapor-assisted imprint lithography. *Adv. Mater.*, 19:757 761, 2007.

[32] N. E. Voicu, M. S. M. Saifullah, K. R. V. Subramanian, M. E. Welland, and U. Steiner. TiO_2 patterning using electro-hydrodynamic lithography. *Soft Matter*, 3:554 557, 2007.

[33] S. Wagner, J. L. Shay, and P. Magliorato. $CuInSe_2$/CdS heterojunction photovoltaic detectors. *Appl. Phys. Lett.*, 25:434 435, 1974.

[34] S. C. Warren, F. J. DiSalvo, and U. Wiesner. Nanoparticles-tuned assembly and disassembly of mesostructured silica hybrids. *Nat. Mater.*, 6:156 161, 2007.

CHAPTER 2

Theoretical Background

2.1 Block Copolymers and Self-Assembly

The name of polymer comes from the Greek words *poly* which means many and *meros* which means parts. A usual polymer is an organic compound, containing carbon atoms together with hydrogen, oxygen, nitrogen and halogens. It is composed of many repeat-units called monomers, which are covalently linked together in a long chain through a *polymerization* reaction [21]. The *molecular weight* M_{w} of the polymer is defined by the weight fraction of the chains, w_{i}, multiplied by their monomer weight. The number of repeat units in one chain is called the degree of polymerization [36]. The polymers are more or less *polydisperse* and the polidispersity indicates the size distribution of the chain length. There are

different types of polymers: **homopolymers**, which are formed from a single type of monomer and **copolymers** which are composed from more than one type of monomer. Three types of copolymers are distinguished as a function of the arrangement of their monomers : *random copolymers* - the repeat unit distribution is random, *block copolymers* - the repeat units are arranged in blocks, and *sequenced copolymers* - chemically different blocks of repeat units are arranged in an alternating sequence.

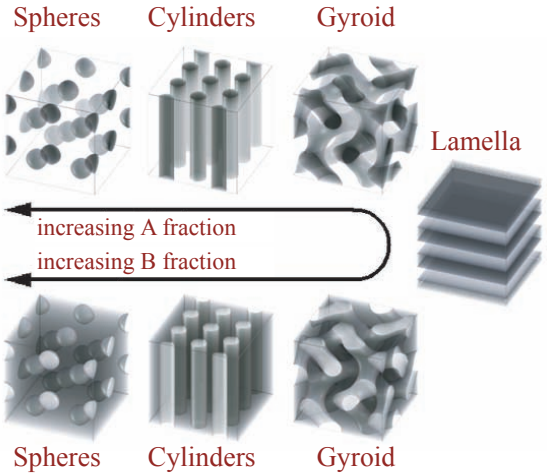

Figure 2.1: Schematic representation of the diblock copolymers morphology as a function of increasing the volume fraction of one component [1].

Block copolymers are composed of two or more chemically different polymer blocks, with different lengths, coupled together by chemical links to form a complex macromolecule. Due to the covalently bonding between the blocks, they cannot demix macroscopically. The microphase separation of the blocks forms nanometer-sized structures. They form 10 - 100 nm-sized microdomain structures with a morphology that is determined by the relative volumes of the blocks [7]. A diblock copolymer with equal block volumes leads a lamellar morphology, which is a sequence of the layers of the two different blocks. With increasing block volume ratio gyroid, cylindrical, and spherical equilibrium morphologies are formed (Figure 2.1).

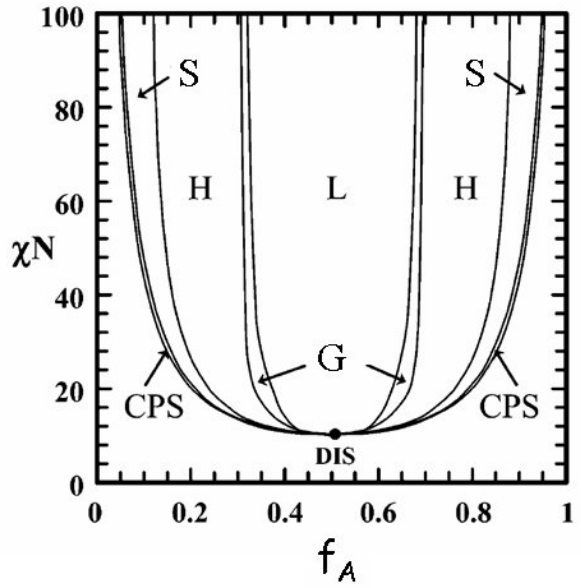

Figure 2.2: The theoretical prediction of the phase diagram of a diblock copolymer (Matsen and Bates, 1996) [25]. Labeling of the phases: L (lamellar), G (bicontinuous gyroid), H (hexagonal cylinders), S (spheres), CPS (close-packed, cubically ordered spherical micelles) and Dis (disordered).

The phase behavior of block copolymers is determined by three factors: the degree of polymerization N, the composition f (volume fraction of the A component), and the A-B segment-segment interaction parameter χ, which is the Flory-Huggins parameter.

The Flory-Huggins theory describes the phase separation process from the thermodynamic point of view. It minimizes the unfavorable interaction energy between different molecules to achieve the smallest surface to volume ratio. The phase diagram of a diblock copolymer is shown in Figure 2.2, where χN represents the degree of incompatibility between the blocks and f_{A} is the volume fraction of component A. If $\chi N \lesssim 10$ the entropy of mixing dominates, resulting in a disordered phase. If $\chi N \gtrsim 10$, entalpic terms dominate, producing an order-to-disorder transition (ODT), where the unlike segments segregate into a variety of ordered periodic microstructures. The connectivity of the blocks have a strong effect on the phase behavior by changing the ODT temperature compared to the

phase separation of a blend of blocks, and on the structure of the boundaries between the ordered phases [11 14].

2.2 Block Copolymer Structure Directing Hybrid Materials

In the second half part of the 1990s, it was discovered that a block copolymer can be used as a structure-directing agent for ceramic materials [6, 16, 38, 44]. Since then research focused on the improvement of the control of the shape and the pore size of organic-inorganic hybrid materials. Self assembly of a mixture of a copolymer with a precursor for an inorganic material will induce a nm-sized structure into the resulting inorganic materials. Organic-inorganic composites with structures on the nm-length scale, require the careful selection of components and processing conditions, however.

In 1995, Bagshaw *et al.* showed that the biodegradable poly(ethylene oxide) (PEO) surfactant acts as a structure directing agent for mesoporous silica molecular sieves, forming spherical, flexible rods, or worm-like micelle morphologies [6]. The PEO surfactant interacts with $Si(OC_2H_5)_{4-x}(OH)_x$ through hydrogen bonds. Increasing the temperature, the hydrogen bonding interaction between the solvent water and the ethylene oxide are broken and a phase separation of the surfactant from the solution was seen.

Templin *et al.* have used a poly(isoprene-block-ethylene oxide) (PI-*b*-PEO) block copolymer as a structure directing agent for alumino-silicate mesostructure materials [38]. The block-copolymer PI-*b*-PEO is interesting because of the high interaction parameter between the PI and PEO. Both PI and PEO have a similar glass transition temperatures (T_g) of around 200 K, which means they have similar mobilities within the microphases [34]. The structural control of the organic-inorganic material depends on the ability of the inorganic precursor to selectively swell only one block of the block copolymer. PI-*b*-PEO was mixed with two

metal oxide precursors: (3-glycidyloxypropyl) trimethoxysilane (GLYMO) and aluminum *sec*-butoxide ($AL(O^sBu)_3$). The metal oxides selectively swell only the PEO block because of the preferential hydrogen bonding. This gives rise to a microphase morphology of PI in a matrix of PEO swollen by the precursor. By adding various amounts of metal alkoxides, hexagonally cylindrical and lamellar morphologies were obtained after removing the block copolymer.

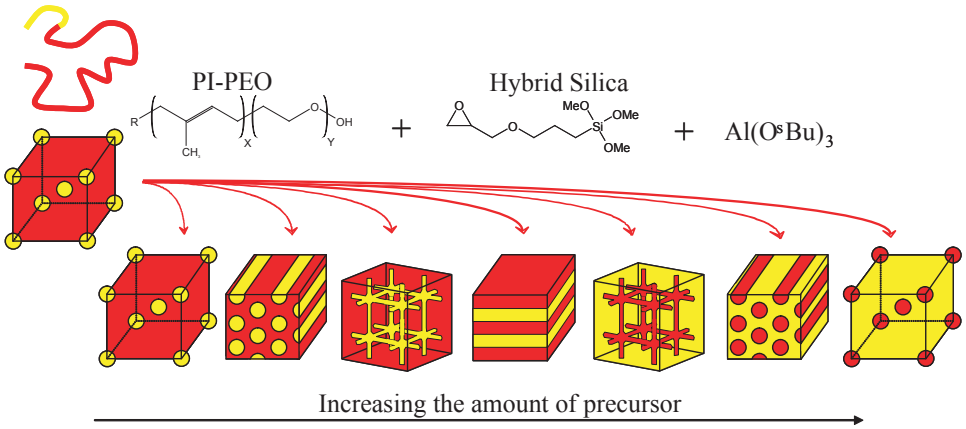

Figure 2.3: Schematic representation of the PI columns in a matrix of PEO mixed with sol-gel precursor. The morphology is changing with increasing the amount of precursor. Courtesy of Ulrich Wiesner.

Ulrich *et al.* showed that the morphology of the final hybrid material is mainly function of the weight fraction of the precursor components, schematically shown in Figure 2.3 [40]. They used a PI-*b*-PEO with a molecular weight of 14 kg/mol and a PEO volume fraction of 11 %, which micro-phase separates into a morphology of PI spheres in a PEO matrix. By increasing the weight fraction of GLYMO and $Al(O^sBu)_3$ (w_{inorg}) to $w_{\text{inorg}} = 0\ 23$, silica spheres were obtained, $w_{\text{inorg}} = 0\ 32$ gave rise to hexagonally packed cylinders, $w_{\text{inorg}} = 0\ 45$ yielded lamella, an inverse cylinder morphology was observed for $w_{\text{inorg}} = 0\ 65$, and $w_{\text{inorg}} = 0\ 82$ gave randomly packed worm-like micelles. For a higher volume fraction of PEO, $f_{\text{PEO}} = 0\ 38$, the amount of precursor has to be increased in order to obtain the spheres, cylinders and lamellar phases. PEO is a polymer that partially crystal-

lizes in the melt, but when mixed with the precursor materials it remains in the amorphous phase.

PI-*b*-PEO block copolymers were also mixed with silica nanoparticles and the influence of the nanoparticles size on the mesostructure was investigated [42]. It was shown that nanoparticles which are smaller than root-mean-square end-to-end distance of PEO block assemble into a lamellar structure, while the larger particles segregate and form a nanoparticle rich core surrounded by lamella which assemble into an onion-type structure.

In 1998, Yang *et al.* extended this approach to mesostructured silica to the non-silicon oxides, such as TiO_2, ZrO_2, Al_2O_3, Nb_2O_5, WO_3, SnO_2, etc. [43]. An amphiphilic poly(alkylene oxide) (P123) block copolymer was used as a structure directing agent in a non-aqueous solution to obtain the mesoporous metal-oxide species. The polymer was dissolved in ethanol and the corresponding metal chloride was added to form the required precursor. After removing the polymer by calcination the mesoporous metal-oxide materials were obtained. The sol-gel methods used to produce mesoporous metal-oxide materials involves a reaction of a metal chloride with a variety of different oxygen donor molecules to a metal oxide or an organic ether [3,4,18,24,29,31,37,39]. If the block copolymer does not dissolve in alcohols or ethers, a mixture of a metal alkoxide and the corresponding metal chloride is needed to obtain the corresponding metal oxide.

The condensation reactions leading to TiO_2 are given as an example because of theirs importance for some photovoltaic devices.

$$TiCl_4 + Ti(OR)_4 \rightarrow 2TiO_2 + 4RCl \tag{2.1}$$

$$TiCl_4 + 2ROR \rightarrow TiO_2 + 4RCl \tag{2.2}$$

The reaction (2.1) applies the case when the block-copolymer does not dissolve in any alcohols or ethers. In this case the condensation between Ti Cl and Ti OR leads to the formation of Ti-O-Ti bridges. The second reaction (2.2), the

alkoxylation, takes place in the case when the block-copolymer is dissolved in an alcohol and only $TiCl_4$ is required to obtain TiO_2 [10]. Usually these reactions are quite slow at room temperature and the oxide formation requires heating to higher temperatures (80 °C - 150 °C). At room temperature, the reaction that takes place between the metal alkoxide and the metal-chloride gives rise to a redistribution of the chloride atoms to a mixture of metal-chloroisopropoxides [4]. Titanium alkoxide is highly reactive for hydrolysis and condensation and therefore a modification of the chemistry is required to obtain titanium sol-gels.

2.3 Sensitizer

In dye sensitized solar cells, the dye plays an important role in the photovoltaic performance as it absorbs the incident light to generate an electron-hole pair. It is situated at the semiconductor-semiconductor or semiconductor-electrolyte heterojunction. The dye should absorb a wide range of the solar spectrum in order to achieve a maximal power conversion efficiency. More than 50 % of the solar energy is emitted in the region of 400 to 800 nm [23]. An ideal sensitizer for a solar cell should absorb all light below the threshold wavelength of about 920 nm. It should be stable for at least 20 years of exposure to the natured light [17].

There are several types of dyes that operate well in solar cells such as squarines [9] and porphyrines [32], and pentacene [33] which is extracted from blackberry juice [30]. The most commonly used dye is a ruthenium complex [22]. To absorb as much light as possible over the entire wavelength spectrum, a high extinction coefficient of the dye is required. The dye adsorbs to oxide - semiconductors through carboxylate, phosphonate, or sulfonate groups. The key issue for a successful dye is that the excited state life time must be long enough to achieve rapid electron injection into the semiconductor material. Also, the dyes should have a long term stability for future commercial applications. The ruthenium complex dyes *cis*-[Ru″(dcpby)$_2$(NCS)$_2$] are the standard dyes for dye sensitized

solar cells because of the good stability of the ruthenium complex compared to other sensitizers. In Figure 2.4 the schematic structures of the dyes used in this work are presented.

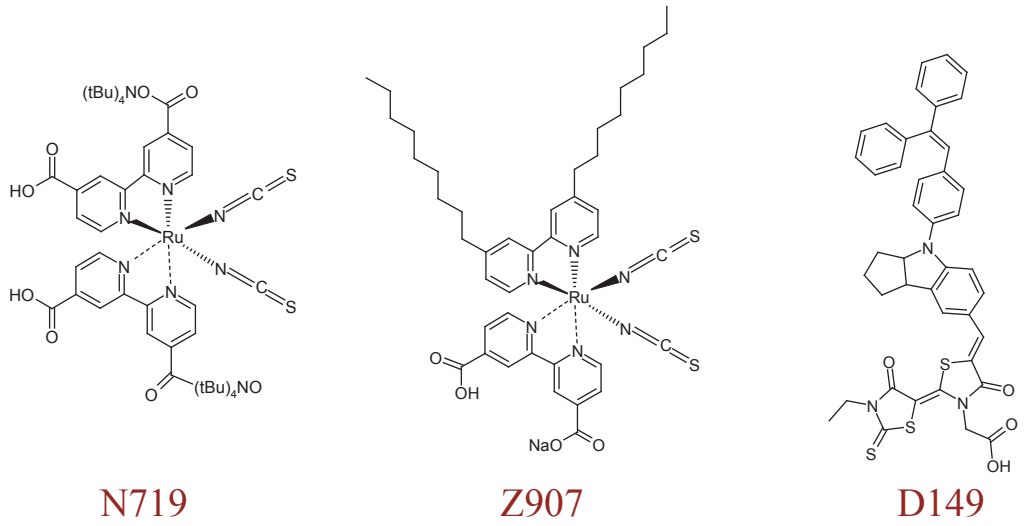

Figure 2.4: Chemical structures of the dyes N-719, Z-907, and the indoline D-149 dyes.

N-719, cis-bis(isothiocyanato)bis(2,2′-bipyridil-4,4′-dicarboxylate) ruthenium (II) bis-tetra-n-buthylammonium, was discovered in 1999 by Nazeeruddin [27]. This dye was used for dye sensitized solar cell having a liquid electrolyte as hole transporter. It is the di-tetrabutylammonium salt of the N3 dye, (cis-bis(isothiocyanato)-bis(2,2′-bipyridil-4,4′-dicarboxylate) ruthenium(II)), which was discovered in 1993 [26]. The N-719 dye has an absorption coefficient at 518 nm of 1 33×10^4 $\mathrm{Lmol^{-1}cm^{-1}}$ and is cca 290 mV negatively red shifted due to the replacement of the OH at the 4,4 positions by the by tetra-butylammonium ($(tBu)_4NO$).

The **Z-907** dye, Ru(4,4′-dinonyl 2,2′-bipyridine)$(NCS)_2$, was used for solid state dye sensitized solar cells, where the hole transporter was an organic material. It was found that when used with a quasi-solid-state gel electrolyte, the efficiency of the devices was over 6 % in full sun light and they were stable under stress and light soaking [41]. The difference between N-719 and Z-907 is the replacement

of 4,4′-dicarboxylic acid 2,2′ bipyridine by 4,4′-dinonyl-2,2′ bipyridine, making the dye more hydrophobic. Z-907 contains two carboxylic groups facilitating the absorption to TiO_2 and two amphiphiles which allow a tighter packing of dye molecules on a surface.

D-149 is an organic metal-free dye developed by Horiuchi *et al.* [19]. First, an indoline dye was sensitized, exhibiting a high efficiency in dye sensitized solar cells using a volatile liquid electrolyte [20]. These organic dyes are attractive because they are metal free, cheaper and easier to produce. To increase the performance of the solar cell devices, the structure of the indoline dye was modified by changing the molecular design of the rhodanine ring which contributed to the red shift in the absorption spectrum [20]. This modified dye is known as D-149. It has an absorption coefficient of 68700 $Lmol^{-1}cm^{-1}$ at 526 nm which is five times higher than the coefficient of the N-719 dye, 13300 $Lmol^{-1}cm^{-1}$ at 541 nm under the same conditions. Using this dye in a device increases light absorption without an appreciable red shift.

D-149 dye was used in this work for solid state dye sensitized solar cells containing an organic hole conductor.

2.4 The Hole Transporter

The hole transporter in a dye sensitized solar cell is used to regenerate the oxidized dye after electron injection into the semiconductor and to carry the positive charges to the counter electrode. To be able to regenerate the dye, the redox potential of the hole transporter has to be higher than the potential of the oxidized sensitizer. The two potentials, of the sensitizer and of the hole transporter, have to be large enough to produce a good driving force for the dye reduction. The hole transporter should not absorb the light in the visible spectral range to avoid the competition with the dye. Dye sensitized solar cells are made from mesoporous anode electrodes, and therefore the hole transporter has to be in the amorphous

state for a better filling of the pores. The molecules have to be very small due to the nm-size of the semiconductor porous material.

Liquid Electrolyte

The so called iodide/tri-iodide (I^-/I_3^-) Robust liquid electrolyte has been used as a hole transporter in dye sensitized solar cells presented in this thesis. It contains iodine, propyl-methyl-imidazolium-iodide (PMII), guanidine thiocynate and methylbenzimidazole. The role of the I^- is to regenerate the dye rapidly from its oxidized Ru(II) state following electron injection into TiO_2. The I_3^- ions created by this process diffuse to the counter electrode and are reduced to I^-. PMII is very viscous, but the viscosity is lowered when mixed with the other components. This liquid electrolyte has a higher viscosity and a better stability compared to a liquid electrolyte based on acetonitrile. Having a more viscous liquid electrolyte results in a slower I^-/I_3^- transport and a slower efficiency of the devices, however.

Spiro-MeOTAD

Spiro-MeOTAD (2,2′,7,7′-tetrakis(N,N-di-p-methoxyphenyl-amine) - 9,9′ spiro bifluorene) derived from TPD (N,N′-diphenyl-N,N′-bis(3 methylphenyl) - 1,1′ - biphenyl - 4,4′diamine) [5] was used as a hole conductor for solid state dye sensitized solar cells. Spiro-MeOTAD has a high glass transition temperature (121 °C) compared to TPD (62 °C). Its amorphous state is stable for years while TPD crystallizes within two months, making Spiro-MeOTAD the better material for solar cell devices. It is deposited by spin-coating from chlorobenzene. Because of its low conductivity, it has to be doped with tertbutyl pyridine (tbp) and Lithium TFSI (ionic dopant) to improve the conductivity and the charge compensation. Because of the lower charge mobility of Spiro-MeOTAD compared to the redox liquid electrolyte, solid state dye sensitized solar cells are less efficient than liquid

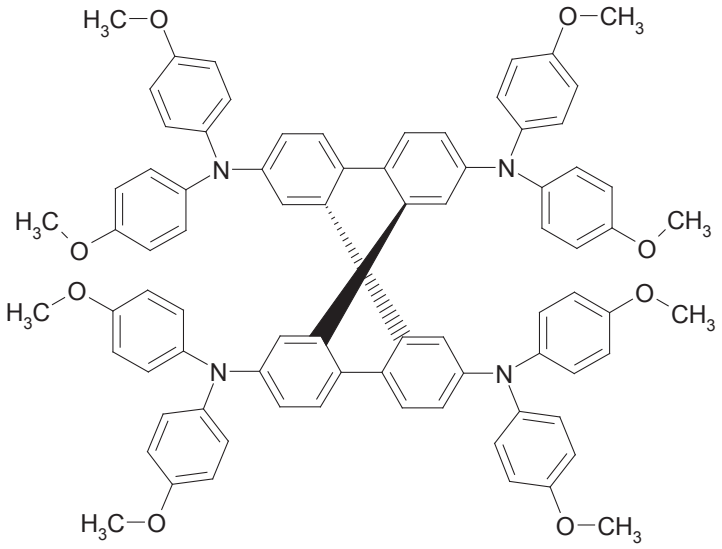

Figure 2.5: Chemical structure of Spiro-MeOTAD (2,2′,7,7′-tetrakis(N,N′-di-p-methoxyphenyl-amine)-9,9′-spirofluorene).

cells.

2.5 Charge Transport and Recombination

The important aspects of a dye sensitized solar cell are the transport of the charges, the dye regeneration, and charge recombination. The charge transfer takes place after sensitizing the dye by the absorption of photons. The dye is excited and a charge transfer from the dye into the conduction band of the TiO_2 occurs. The *generation* is an electronic excitation event which increases the number of free carriers available to carry charges. It is the transfer of an electron from the valence to conduction band of the semiconductor which creates an electron-hole pair. The *recombination* is an electronic relaxation event which reduces the number of free carriers [28]. It is the loss of an electron or a hole through the decay of the electron to a lower energy state. Generation requires an input of energy while the recombination releases the energy. *Photogeneration* means the generation of mobile electrons and holes through the absorption of light in the

semiconductor.

For the liquid electrolyte dye sensitized solar cells, the charge recombination takes place between the electrons in the TiO_2 with the holes in the triiodide and the oxidized dye molecules. The electron transport of the solar cells is dominated by the properties of the TiO_2. The recombination takes place at the interface and depends on the spatial region of photoinjected charges in the cell, the redox electrolyte, and the surface properties of the TiO_2 films. In this case, if the oxidized dye is not quickly regenerated, the charges will be lost under high illumination intensity [35]. The recombination is slow, between tens of milliseconds and seconds, once the regeneration of the dye has occurred.

In solid state dye sensitized solar cells the hole transfer is faster than in the liquid cells, on the nanosecond timescale, and therefore recombination takes place almost exclusively between the electrons from the TiO_2 and the holes in the hole transport material. Also, the recombination is faster compared to the liquid cells (micro- to milliseconds).

To improve the device efficiency charge collection has to be maximized. This implies a longer electron diffusion length (L_{D}) and an increase in the electron-hole recombination lifetime. The electron diffusion coefficient (D_{e}) can be evaluated from the equation: $D_{\mathrm{e}} = w^2\ 2\ 35\tau_{\mathrm{trans}}$, where w is the TiO_2 film thickness and τ_{trans} is the electron transport lifetime. At low light intensities, D_{e} is on the order of 10^{-4} $\mathrm{cm^2 s^{-1}}$. D_{e} increases with increasing the illumination intensity. Knowing D_{e} and the electron lifetime, L_{D} can be estimated from the equation: $L_{\mathrm{D}} = \quad \overline{D_{\mathrm{e}}\tau_{\mathrm{e}}}$, where, τ_{e} is the time constant for electron-hole recombination.

2.6 Magnetism and Ferromagnetism

Magnetism and electricity were initially considered as separate subjects and is still possible to study the interactions of the magnets without reference to electricity [15]. Magnetism in condensed matter systems which includes ferromagnets, spin-

glasses and low dimensional systems is still of great interest. The most interesting magnetic effects found in condensed matter systems are based on atoms which posses interacting magnetic moments [8].

The basic object in magnetism is the *magnetic moment*. If we consider a loop having a current $\overrightarrow{\boldsymbol{I}}$ enclosing an area $\mathrm{d}S$, the magnetic moment $\mathrm{d}\mu$ is given by:

$$\mathrm{d}\mu = \overrightarrow{\boldsymbol{I}}\,\mathrm{d}S \tag{2.3}$$

The length of the vector $\mathrm{d}S$ is equal to the area of the loop. The vector direction is normal to the loop and is determined by the direction of the current around the loop. The magnetic moment $\mathrm{d}\mu$ lies normal to the plane of the loop of current and can be parallel or antiparallel to the angular momentum vector associated with the charge that is going around the loop. If the loop has an infinite size, the magnetic moments can be calculated by summing-up the magnetic moments of infinitesimal current loops spread through the area of the loop. We take into account only the current running around the perimeter of the loop, because all the currents from the neighboring infinitesimal loops are canceled:

$$\mu = \int \mathrm{d}\mu = \overrightarrow{\boldsymbol{I}} \int \mathrm{d}S \tag{2.4}$$

For atoms the magnetic moment μ associated within orbiting electron points in the same direction as the angular momentum $\overrightarrow{\boldsymbol{L}}$ of that electron. μ is given by:

$$\mu = \gamma \overrightarrow{\boldsymbol{L}} \tag{2.5}$$

where γ is the constant *gyromagnetic ratio*.

A magnetic moment μ in a magnetic field $\overrightarrow{\boldsymbol{B}}$ has an energy given by the relation:

$$E = -\mu \overrightarrow{\boldsymbol{B}} \tag{2.6}$$

The energy is minimized when the magnetic moment is situated along the mag-

netic field.

A magnetic solid is composed of a large number of atoms with magnetic moments. The *magnetization* $\overrightarrow{\boldsymbol{M}}$ is defined as the magnetic moment per unit volume and can be considered to be continuous everywhere excluding the edges of the magnetic solid. If we consider a free space, there is no magnetization and therefore the magnetic field can be characterized by the vector fields $\overrightarrow{\boldsymbol{B}}$ and $\overrightarrow{\boldsymbol{H}}$:

$$\overrightarrow{\boldsymbol{B}} = \mu_{\mathrm{o}} \overrightarrow{\boldsymbol{H}} \tag{2.7}$$

where $\mu_{\mathrm{o}} = 4\pi \times 10^{-7}$ Hm^{-1} is the *permeability* of the free space. In a magnetic solid the two vector fields $\overrightarrow{\boldsymbol{B}}$ and $\overrightarrow{\boldsymbol{H}}$ may vary in direction and magnitude.

$$\overrightarrow{\boldsymbol{B}} = \mu_{\mathrm{o}} (\overrightarrow{\boldsymbol{H}} + \overrightarrow{\boldsymbol{M}}) \tag{2.8}$$

If the magnetization is linearly related to the magnetic field $\overrightarrow{\boldsymbol{H}}$, the solid is called a linear magnetic material and $\overrightarrow{\boldsymbol{M}}$ is given by the relation:

$$\overrightarrow{\boldsymbol{M}} = \chi \overrightarrow{\boldsymbol{H}} \tag{2.9}$$

where χ is the *magnetic susceptibility* which is a dimensionless quantity. Equations 2.9 in 2.8 yield:

$$\overrightarrow{\boldsymbol{B}} = \mu_{\mathrm{o}} (1 + \chi) \overrightarrow{\boldsymbol{M}} = \mu_{\mathrm{o}} \mu_{\mathrm{r}} \overrightarrow{\boldsymbol{H}} \tag{2.10}$$

where $\mu_{\mathrm{r}} = 1 + \chi$ is the *relative permeability* of the material.

The materials respond differently to the applied magnetic field, and therefore different types of magnetism are known:

- **Diamagnetism** is a fundamental property which arises from the non - cooperative behavior of the electrons when they are exposed to a magnetic field. When the material is in a magnetic field, the magnetization and the susceptibility are negative and the susceptibility is temperature independent. The

magnetization is zero when the field is zero.

- **Paramagnetism** is seen when the atoms or ions have a magnetic moment due to the unpaired electrons in partially filled orbitals. The individual magnetic moments do not interact magnetically and in this case the magnetization is zero when the magnetic field is removed. There is a partially alignment of the atomic moments in the direction of the field when the magnetic field is applied, giving rise to a positive magnetization and susceptibility.

- **Ferromagnetism** is caused by a strong interaction of the atomic moments due to the exchange of electronic forces resulting in a parallel or antiparallel alignment of the atomic moments. There is a large magnetization, even in the absence of a magnetic field.

- **Ferrimagnetism** occurs for oxides with a structure which is composed of two magnetic sublattices (A and B), separated by oxygens. It is similar to ferromagnetism but has very different magnetic order. The magnetic moments of the A and B sublattices are not equal and result in a net magnetic moment.

- **Antiferromagnetism** is the limit in which the moments of the A and B sublattices are equal but opposite and the net magnetic moment is zero.

The ferromagnetic materials have two characteristics: *spontaneous magnetization*, which exists inside a uniformly magnetized microscopic volume in the absence of an applied magnetic field below a *magnetic ordering temperature*. Above the T_c the thermal energy randomizes the magnetic moments. Below T_c the ferromagnet is ordered, above T_c it is disordered.

Ferromagnets can maintain the memory of an applied field even when it is removed. This behavior is called *hysteresis*. The hysteresis loop displays the relation between the magnetic flux density and the magnetic force (Figure 2.6).

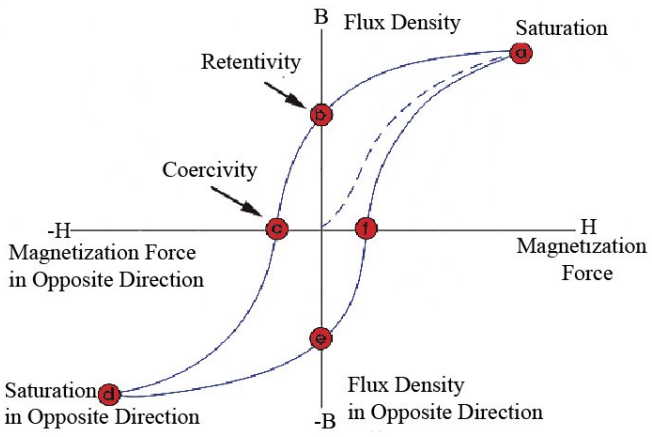

Figure 2.6: Schematic representation of the hysteresis loop of a ferromagnetic material [2].

The hysteresis loop is also known as the $\vec{B}$-$\vec{H}$ loop and is given by measuring the magnetic flux density $\vec{B}$ when the magnetization force $\vec{H}$ is changed. The dashed line shows a ferromagnetic material which has never been magnetized with increasing $\vec{H}$. $\vec{B}$ increases with increasing $\vec{H}$ until the magnetic domains are aligned and no further increase in the magnetic flux occurs, which means that the material has reached the saturation point. When $\vec{H}$ is reduced to zero, there is a remaining magnetic flux, even though the applied magnetic field is zero. This point is called retentivity and shows the remanence or the level of the residual magnetism in the material. $\vec{H}$ can be reversed to a point where $\vec{B}$ is zero. This point is called the coercivity point. The force required to remove the residual magnetization from the material is called the coercivity or the coercive force of the material. With increasing negative $\vec{H}$ the material becomes saturated in the opposite direction. Increasing $\vec{H}$ in the positive direction, to a point where $\vec{B}$ is zero traces a different path to the saturation point, because some force is needed to remove the residual magnetism from the material.

Bibliography

[1] *www.msri.org.*

[2] *www.ntd-ed.org.*

[3] P. Arnal, R. J. P. Corriu, D. Leclercq, P. H. Mutin, and A. Vioux. Preparation of anatase, brookite and rutile at low temperature by non-hydrolytic sol-gel methods. *J. Mater. Chem.*, 6:1925 1932, 1996.

[4] P. Arnal, R. J. P. Corriu, D. Leclercq, P. H. Mutin, and A. Vioux. A solution chemistry study of nonhydrolytic sol-gel routes to titania. *Chem. Mater.*, 9:694 698, 1997.

[5] Udo Bach. *Solid-state dye-sensitized mesoporous TiO_2 solar cells.* PhD thesis, Ecole Polythechnique Federale de Lausanne, 2000.

[6] S. A. Bagshaw, E. Prouzet, and T. J. Pinnavaia. Templating of mesoporous molecular sieves by nonionic polyethylene oxide surfactants. *Science*, 269:1242 1244, 1995.

[7] F. S. Bates and G. H. Fredrickson. Block copolymer thermodynamics: Theory and experiment. *Annu. Rev. Phys. Chem*, 41:525 557, 1990.

[8] S. Blundell. *Magnetism in condensed matter*. Oxford University Press, 2006.

[9] A. Burke, L. Schmidt-Mende, S. Ito, and M. Gratzel. A novel blue dye for near-IR dye-sensitized solar cell applications. *Chem. Commun.*, pages 234 236, 2007.

[10] X. Chen and S. S. Mao. Titanium dioxide nanomaterials: synthesis, properties, modifications and applications. *Chem. Rev.*, 107:2891 2959, 2007.

[11] M. Olvera de la Cruz and Isaac C. Sanchez. Theory of microphase separation in graft and star copolymers. *Macromol.*, 19:2501 2508, 1986.

[12] G. Floudas, N. Hadjichristidis, H. Iatrou andT. Pakula, and E. W. Fisher. Microphase separation in model 3-miktoarm star copolymers (simple grat) and terpolymers. Statistics and kinetics. *Macromol.*, 27:7735 7746, 1994.

[13] G. Floudas, S. Pispas, N. Hadjichristidis, T. Pakula, and I. Erukhimovich. Microphase separation in star block copolymers of styrene and isoprene. Theory, experiments and simulation. *Macromol.*, 29:4142 4154, 1996.

[14] G. Foudas, N. Hadjichristidis, Y. Tselikas, and I. Erukhimovich. Micorphase separation in model 4-miktoarm star copolymers of AB3 type. *Macromol.*, 30:3090 3096, 1997.

[15] W. M. Gibson. *Basic electricity*. Penguin Education, 1969.

[16] C. G. Goltner, S. Henke, M. C. Weissenberger, and M. Antonietti. Mesoporous silica from lyotropic liquid crystal polymer templates. *Angew. Chem. Int. Ed.*, 37:613 616, 1998.

[17] M. Gratzel. Dye-sensitized solar cells. *J. of Photochemistry and Photobiology C: Photochemistry Reviews*, 4:145 153, 2003.

[18] J. N. Hay and H. M. Raval. Synthesis of organic-inorganic hybrids via the non-hydrolytic sol-gel process. *Chem. Mater.*, 13:3396 3403, 2001.

[19] T. Horiuchi, H. Miura, K. Sumioka, and S. Uchida. High efficiency of dye-sensitized solar cells based in metal free indoline dyes. *J. Am. Chem. Soc.*, 126:12218 12219, 2004.

[20] T. Horiuchi, H. Miura, and S. Uchida. Highly efficient metal free organic dyes for dye sensitized solar cells. *Chem. Commun.*, pages 3036 3037, 2003.

[21] Richard A. L. Jones. *Soft condensed matter.* Oxford University Press, 2006.

[22] C. Klein, M. K. Nazeeruddin, D. Di Censo, P. Liska, and M. Gratzel. Amphiphilic ruthenium sensitizers and their applications in dye-sensitized solar cell. *Inorg. Chem.*, 43:4216 4226, 2004.

[23] J. Kruger. *Interface engineering in solid - state dye-sensitized solar cells.* PhD thesis, Ecole Polytechnique Federale de Lausane, 2003.

[24] P. Lafond, P. H. Mutin, and A. Vioux. Control of the texture of titania-silica mixed oxides prepared by nonhydrolytic sol-gel. *Chem. Mater.*, 16:5380 5386, 2004.

[25] M. W. Matsen and F. S. Bates. *Conformationally asymmetric block copolymers.* John Wiley Sons Inc, 1996.

[26] M. K. Nazeeruddin, A. Kay, I. Rodicio, H. Humphry-Baker, E. Muller, P. Liska, N. Vlachopoulos, and M. Gratzel. Coversion of light to electricity by cis-X2Bis(2 2-bipyridyl-4 4-dicarboxylate) ruthenium(II) charge transfer sensitizers (X=Cl, Br, I, CN and SCN) on nanocrystalline TiO_2 electrodes. *J. Am. Chem. Soc.*, 115:6382 6390, 1993.

[27] M. K. Nazeeruddin, S. M. Zakeeruddin, R. Humphry-Baker, M. Jirousek, P. Liska, N. Vlachopoulos, V. Shklover, C.-H. Fischer, and M. Gratzel. Acid-

base equilibria of (2,2-bipyridil-4,4-dicarboxylic acid)ruthenium(II) complexes and the effect of protonation on charge transfer sensitization of nanocrystalline titania. *Inorg. Chem.*, 38:6298 6305, 1999.

[28] Jenny Nelson. *The physics of solar cells.* Imperial College Press, 2003.

[29] M. Niederberger, M. H. Bartl, and G. D. Stucky. Benzyl alcohol and titanium tetrachloride -A versatile reaction system for the nonaqueous and low temperature preparation of crystalline and luminescent titania nanoparticles. *Chem. Mater.*, 14:4364 4370, 2002.

[30] A. Olea, G. Ponce, and P. J. Sebastian. Electron transfer via organics dyes for solar conversion. *Solar Energy Materials. Solar Cells*, 59:137 143, 1999.

[31] H. Parala, A. Devi, R. Bhakta, and R. A. Fischer. Synthesis of nano-scale TiO_2 particles by nonhydrolytic approach. *J. Mater. Chem.*, 12:1625 1627, 2002.

[32] L. Schmidt-Mende, W. M. Campbell, Q. Wang, K. W. Jolley, D. L. Officer, M. K. Nazeeruddin, and M. Gratzel. Zn-porphyrin-sensitized nanoscrystalline TiO_2 heterojunction photovoltaic cells. *Chem. Phys. Chem*, 6:1253 1258, 2005.

[33] G. K. R. Senadeera, P. V. V. Jayaweera, V. P. S. Perera, and K. Tennakone. Solid-state dye-sensitized photocell based on pentacene as a holle collector. *Solar Energy Materials. Solar Cells*, 73:103 108, 2002.

[34] P. F. W. Simon, R. Ulrich, H. W. Spiess, and U. Wiesner. Block copolymer-ceramic hybrid materials from organically modified ceramic precursors. *Chem. Mater.*, 2001:3464 3486, 13.

[35] H. J. Snaith and L. Schmidt-Mende. Advances in liquid-electrolyte and solid-state dye-sensitized solar cells. *Adv. Mater.*, 19:3187 3200, 2007.

[36] G. Strobl. *The physics of polymers*. Springer, Berlin, 1907.

[37] J. Tang, F. Redl, Y. Zhu, T. Siegrist, L. E. Brus, and M. L. Steigerwald. An organometallic synthesis of TiO_2 nanoparticles. *Nano Lett.*, 5:543 548, 2005.

[38] M. Templin, A. Franck, A. Du Chesne, H. Leist, Y. Zhang, R. Ulrich, V. Schadler, and U. Wiesner. Organically modified aluminosilicate mesostructures from block copolymer phases. *Science*, 278:1795 1798, 1997.

[39] T. J. Trentler, T. E. Denler, J. F. Bertone, A. Agrawal, and V. L. Colvin. Synthesis of TiO_2 nanocrystals by nonhydrolytic solution-based reactions. *J. Am. Chem. Soc.*, 121:1613 1614, 1999.

[40] R. Ulrich, A. Du Chesne, M. Templin, and U. Wiesner. Nano-objects with controlled shape, size and composition from block copolymer mesophase. *Adv. Mater*, 11:141 146, 1999.

[41] P. Wang, S. M. Zakeeruddin, J. E. Moser, M. K. Nazeeruddin, T. Sekiguchi, and M. Gratzel. A stable quasi-solid-state dye-sensitized solar cell with an amphiphilic ruthenium sensitizer and polymer gel electrolyte. *Nature Materials*, 2:402 407, 2003.

[42] S. C. Warren, F. J. Disalvo, and U. Wiesner. Nanoparticles-tuned assembly and disassembly of mesostructured silica hybrids. *Nature Materials*, 6:156 161, 2007.

[43] P Yang, D. Zhao, D. I. Margolese, B. F. Chmelka, and G. D. Stucky. Generalized syntheses of large-pore mesoporous metal oxides with semicrystalline frameworks. *Nature*, 396:152 155, 1998.

[44] D. Zhao, J. Feng, Q. Huo, N. Melosh, G. H. Fredrickson, B. F. Chmelka, and G. D. Stucky. Triblock copolymer syntheses of mesoporous silica with periodic 50 to 300 angstrom pores. *Science*, 279:548 552, 1998.

CHAPTER 3

Materials and Sample Preparation

3.1 Materials

The following chemicals were used to obtain nickel metal and mesoporous materials.

- Nickel Naphthenate, 60 % in toluene (6-8 %Ni), Streem Chemicals UK.
- Poly(Isoprene-block-Ethylene Oxide), home made by Ulrich Wiesner s group at Cornell University, USA.
- Titanium (IV) Isopropoxide, 97.0+ %, Alfa Aesar.
- Titanium (IV) Chloride, 99.0 %, Aldrich.

- Niobium (V) Ethoxide, 99.95 %, Aldrich.
- Niobium (V) Chloride, 99.99 %, Aldrich.
- Tetrahydrofuran (THF), Spectrophotometric grade, 99.5 %, Aldrich.
- α-Terpineol, 96.0+ %, Natural, FCC, Aldrich.
- Ethyl Cellulose, 30-60 mPa.s., viscosity 5 % in toluene/ethanol 80:20, Aldrich.
- Spiro-MeOTAD - 2,2 7,7 -tetrakis(N,N-di-methoxypheny-amine)- 9,9 -spiro bifluorene, Merck Chemicals.
- $Li[CF_3SO_2]_2N$, Aldrich.
- Tert.-butylpyridine, Aldrich.

Sensitizing Dyes:

◇ **Z 907** - cis-di(thiocyanato)-(2,2 -bipyridyl-4,4 -dicarboxylic acid)(4,4 -dinonyl-2,2 bipyridyl)-ruthenium(II), from EPFL

◇ **N 719** - cis-di(thiocyanato)-bis(2,2 -bipyridyl-4-carboxylate-4 -carboxylic acid)-ruthenium(II), from EPFL

◇ **D 149** - indoline dye, from EPFL

The robust liquid electrolyte was prepared from

◇ 0.8 M of Propyl-Methyl-Imidazolium-Iodide, made at EPFL Laboratory, Lausanne.

◇ 0.15 M of Iodine, Aldrich.

◇ 0.5 M of N-Methylbenzimidazole, Aldrich and crystallized in Diethyl Ether before use.

◇ 0.1 M of Guanidine Thiocynate, Fluka.

3.2 Sol - Gel Precursor Preparation

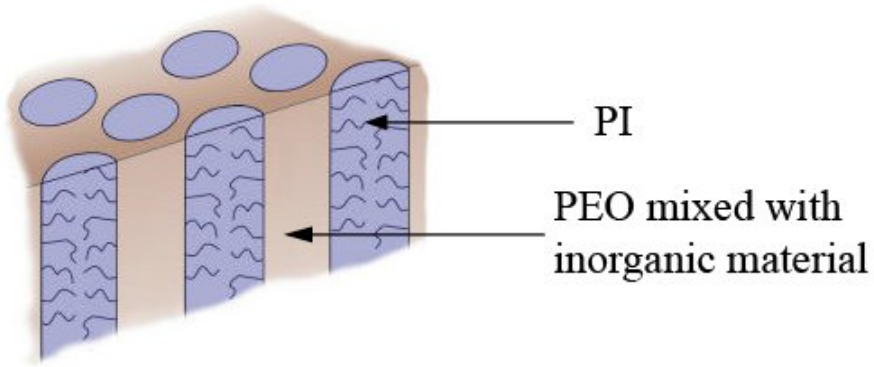

Figure 3.1: Schematic representation of the PI columns in a matrix of PEO mixed with inorganic precursor materials [5].

The mesoporous materials for the dye sensitized solar cells reported in this thesis are composed of the block copolymer PI-*b*-PEO which contains one hydrophilic block (PEO) having the chemical formula HO-$(CH_2$-CH_2-$O)_n$-H and an apolar block (PI) with the structure CH_3-$(CH_2$-$CH_2)_n$-H. PI is a hydrophobic block which is thermally more stable than PEO. It is has two sp^2 carbons per monomer which are converted into graphitic carbon when heated in an inert atmosphere. The carbon seats around the pore walls acting as a rigid support thereby preventing the collapse of the pores. The inorganic precursor material used to manufacture mesoporous materials is composed of a metal chloride which reacts with the metal-alkoxide to form the corresponding alkyl halide [1, 5]. The inorganic precursor materials were chosen in such a way that they selectively swells only the hydrophilic block, PEO in our case, giving rise to a morphology in which PI columns are surrounded by a matrix of PEO with the embedded precursor, Figure 3.1.

The precursor solutions used for the mesoporous materials reported in this thesis were prepared as follows: a diblock copolymer poly(isoprene block ethylene oxide) (PI-*b*-PEO) was dissolved in anhydrous tetrahydrofuran (THF) and dry

chloroform (in the case of Nb_2O_5). For TiO_2 the ratio between PI-*b*-PEO and the titania precursor was 1:2. 0.2 g of PI-*b*-PEO was dissolved in 2 ml of THF. To this solution, 0.73 ml of titanium (IV) isopropoxide was added and the solution was stirred for 30 min. 0.27 ml of $TiCl_4$ was added followed by stirring for another 2 hours.

For Nb_2O_5, PI-*b*-PEO was dissolved in THF or chloroform. 0.07 g of polymer was dissolved in 1.5 ml of solvent. 0.15 ml of niobium (V) ethoxide was added to the solution and stirred for 30 minutes followed by the addition of 0.1 g of $NbCl_5$ and stirring for another 2 hours. This solution was prepared in a glove box because of oxygen sensitivity of $NbCl_5$.

3.3 Substrate Preparation

Structured FTO

Fluorine doped tin oxide (FTO) glass (Nippon glass) which was used for dye sensitized solar cells devices was cleaned as follows: the FTO coated glass sheets were etched with zinc powder and HCl (4N) to form the required electron pattern [3, 11]. Scotch tape was used as mask material. After etching, the samples were cleaned with soap (2 % of Telmanex in water) and cut in 1.15×1.15 cm^2 squares. The pieces were then cleaned with acetone in a sonication bath for 10 minutes followed by 10 minutes in isopropanol. They were dried with a N_2 gun and treated for 10 min. under an O_2 plasma to remove all the organic residues. The pieces used for solid state dye sensitized solar cells were coated with a compact TiO_2 layer.

Compact TiO_2 layer

The compact TiO_2 layer was sprayed onto the conductive FTO substrate as a blocking layer for holes on the FTO electrode. A solution of titanium(IV)-bis-

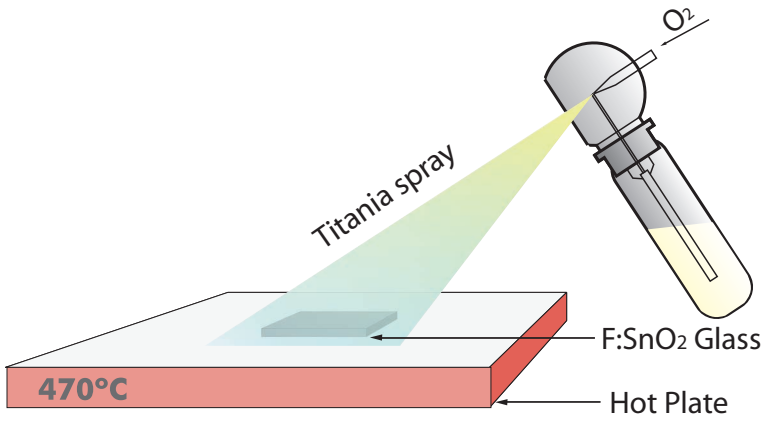

Figure 3.2: Set-up of spray pyrolysis. Courtesy of Sven Huttner.

(acetylacetonate)-diisopropylate dissolved in dry ethanol, in a 1:10 volume ratio was used. The FTO substrates were placed onto a hot plate heated to 470 °C and the solution was aerosol-sprayed using O_2 as carrier gas as schematically shown in Figure 3.2 [3, 10]. The TiO_2 layers were prepared in 32 sprays, processes which gave an approx. 60 nm thick film. The samples were left on the hot plate at 470 °C for 30 minutes to transform the precursor into anatase TiO_2 and to evaporate the organic components. The sample was then cooled down to room temperature.

Platinized FTO substrates

The counter electrodes used for the dye sensitized solar cells described in this thesis were platinized FTO. The FTO was cut in 1.5×1.3 cm pieces and a layer of 50 mM hexachloroplatinic (IV) acid in anhydrous isopropanol was spread on it. The coated substrates were placed onto a hot plate at 450 °C for 15 minutes. This procedure gave optically transparent electrodes [7].

3.4 Snow-jet Cleaning

The CO_2 snow cleaning process removes micron sized particles and organic contaminants, such as hydrocarbon based contamination. This method is non destruc-

tive, nonabrasive, residue free and without chemical waste after cleaning [9].

In our experiments, we use it for cleaning silicon wafers. The snow - jet system consists of a CO_2 pressurized bottle connected to a nozzle controlled by a on/off valve. During the cleaning procedure the silicon wafer is held by a vacuum chuck. The dust particles are easily removed from the wafer. This removal can be explained by two different mechanisms. The mechanism for particle removal involves the aerodynamic forces related to the movement of the high-velocity gas and to the momentum transfer between the dry ice and surface contamination. The mechanism for the removal of organic compounds requires the presence of liquid carbon dioxide during impact.

Liquid carbon dioxide is a very good solvent for hydrocarbons and other non-polar substances. Liquid carbon dioxide is not stable at atmospheric pressures and room temperature, but is present in the snow cleaning process on the surface. During the short impact time, the pressure increases at the snow-surface interface and this pressure can easily exceed the yield stress and the triple point pressure of the dry ice particle. The dry ice particle liquefies and acts as a solvent while in contact with the surface. The organic contamination is dissolved by the liquid CO_2 phase. When the particle rebounds from the surface, the pressure decreases and the CO_2 resolidifies, carrying the contaminations away.

3.5 Spin Coating Technique

Spin coating is one of the most used techniques to uniformly coat a substrate with a thin layer of polymers or other solutions. If a drop of solution is placed on a substrate, it can spreads to form a continuous film or it forms a droplet on the surface, depending on the wettability of the substrate [12]. The substrate is held in place by a vacuum chuck (Figure 3.3).

By spinning the substrate, the droplet is forced to spread out while the solvent evaporates. The liquid flows radially, due to the centrifugal force and the excess

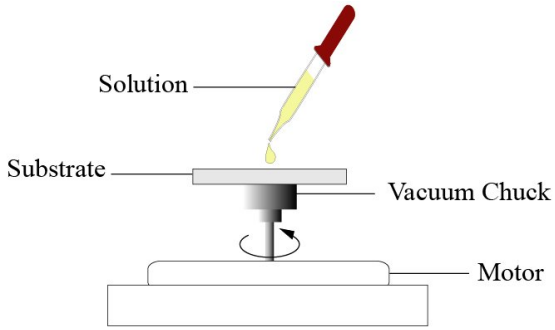

Figure 3.3: Representation of spin coating technique for the deposition of flat films.

solution flies off the edges of the substrate. The film continues to thin by solvent evaporation until it turns solid. The physics behind spin coating involves a balance between centrifugal forces controlled by the spin speed and viscous forces which are determined by the solvent viscosity, giving rise to a homogenous film.

The parameters involved in spin coating are: solution viscosity, solid content, angular speed, and spin time, which are the parameters determining the thickness of the final film. The thickness of the film increases with decreasing the spin speed and spin time. If the deposition conditions are correctly chosen, a thin film of uniform thickness is deposited onto the substrate. The thickness of films which are thinner than 1 μm can be deduced directly from the interference color of the film.

3.6 Polymer Degradation and Metal Oxidation

After the preparation of the precursor mixture, the spin-coated films on different substrates (such as silicon wafers or FTO) were placed onto a hot plate at 100 °C for 1 hour to evaporate the remaining solvent, and were then transferred into a tube furnace for high - temperature calcination. To manufacture bulk material, the precursor solution was put into a ceramic boat on a hot plate at 50 °C for

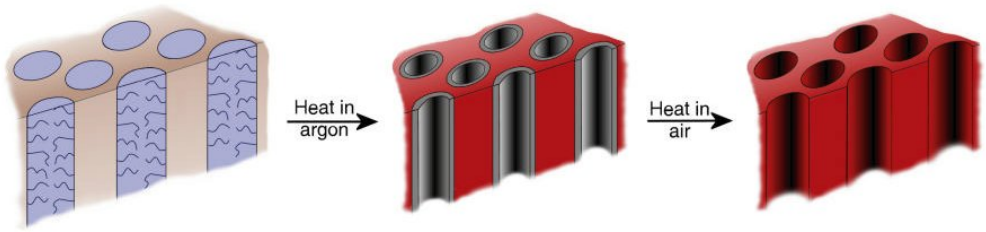

Figure 3.4: Schematic presentation of the transformation of PI into carbon which acts as a scaffold for the pores and its removal when heated under oxygen. Courtesy of Jinwoo Lee, [5]

more then 24 hours to evaporate the solvent. To ensure a slow solvent evaporation the boat was partly covered. Then, the materials were placed in a vacuum oven at 130 °C for 3 or 4 hours to completely evaporate the solvent.

After solvent evaporation, the spin-coated films or bulk material were transferred into a tube furnace for calcination at temperatures of 450 - 800 °C for 2 hours. The heating rate was 1 °/min. A nitrogen or argon flow was maintained through the furnace. During this process PEO was burnt off, PI was transformed into graphitic carbon which is thought to coat the pores, preventing the collapse of the porous structure at these temperatures, and the metal oxide starts to crystallize, as shown on the schematic presentation in Figure 3.4. To remove the carbon, the material was heated in an oxygen flow to 500 °C for 2 hours in the case of films and, around 5 hours in the case of bulk material.

3.7 Paste Fabrication

The TiO_2 and Nb_2O_5 pastes were made using Ito s recipe [2]. The powder obtained after calcination was ground in a mortar until a very fine powder was obtained. To 0.222 g of powder, 0.04 ml of acetic acid was added drop by drop, or all once, while continuing to grind until the liquid has partially evaporated and a wet powder was obtained. Then 0.04 ml of water was added drop by drop while grinding it for 1 min to evaporate the water. This was repeated 5 times. 0.04 ml ethanol (99 %)

was added while grinding for 1 min, repeating this process for 15 times. Then 0.1 ml of ethanol was added, grinding for 1 min and repeating 6 times. The TiO_2 dispersion in the mortar was transferred into a beaker and 4 ml of ethanol were added, followed by stirring with a magnet stirrer for 5 min. 0.8 g of terpineol was added and the solution was stirred for 5 min, followed by sonication using a sonicator horn (Ultrasonic Processor, Model CV33, Cole Parmer) for 30 min (2 min work + 2 min rest). 0.12 g of ethyl cellulose was added, stirring the solution until it was dissolved, followed by sonication for 30 min (2 min work + 2 min rest). The paste was concentrated by evaporating the ethanol using a stirrer at room temperature.

Ito reported that the coexistence of water and acetic acid was important. Without water and acetic acid, the films were unstable and did not keep their structure after sintering. [2]

3.8 Preparation of Liquid Electrolyte

The Robust liquid electrolyte was fabricated as follows: N-methylbenzimidazole was dissolved in diethyl ether and crystallized over night at room temperature followed by 2 hours in the fridge. 0.15 M of iodine was mixed with 0.1 M of guanidinium thiocynate, 0.5 M of crystallized N-methylbenzimidazole, 0.8 M of PMII and 0.55 ml of 3-methosypropionitride. The solution was stirred over night at room temperature and the robust PMII liquid electrolyte was obtained.

3.9 Device Assembly

3.9.1 Solid State Dye Sensitized Solar Cells

The device assembly of solid state dye sensitized solar cells is schematically shown in the Figure 3.5.

The coated FTO substrates with a compact TiO_2 layer were used as bottom

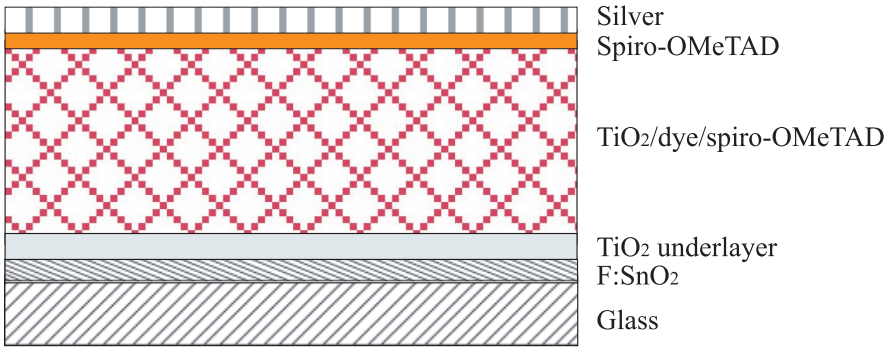

Figure 3.5: Schematic presentation of a solid state dye sensitized solar cell.

electrodes for solid state DSC. A layer of TiO_2 precursor solution was spin - casted at 3000 rpm. The samples were dried on a hot plate at 100 degrees for 1 hour, and transferred into a tube furnace for calcination which was heated with 1 °/min to 450-600 °C) for 2 hours. Prior to sensitizing in a dye solution, the mesoporous TiO_2 films were treated in a mild Piranha solution (1 part of Millipore water, 3 parts of sulphuric acid, 98 %, and 2 parts of hydrogen peroxide, 30 %) for 30 minutes at 50 °C, then rinsed in Millipore water, followed by 1 minute in ethanol and drying with a N_2 gun. The samples were soaked in a 0.5 mM dye solution in acetonitrile:tert.-butanol (1:1 vol %) at room temperature [8]. The Spiro-MeOTAD hole transporter used for these devices was dissolved in chlorobenzene (CB) with a concentration of 180 mg/ml. Tertbutyl pyridine (tbp) was added to the solution (1:57 tbp:CB). Lithium TFSI (ionic dopant) was separately predissolved in acetonitrile at 170 mg/ml, [11] (100 μl chlorobenzene, 18 mg Spiro-MeOTAD, 1.75 μl of tertial-butyl pyridine and 3.75 μl of lithium -TFSI ACN solution). The dyed films were rinsed in acetonitrile and dried in air for 1 minute. The Spiro-MeOTAD solution (15 μl) was deposited on top of the film and left for 40 seconds to penetrate into the pores, followed by spin-coating at 2000 rpm for 30 sec. in air. The samples were placed in a high vacuum evaporator (10^{-6} bar) and 200 nm of silver were deposited by evaporation through a shadow mask.

3.9.2 Dye Sensitized Solar Cells

Dye sensitized solar cells using a liquid electrolyte were assembled as follows: FTO coated sheets were cut into 1.5×1.3 cm^2 pieces, and cleaned with acetone and isopropanol, followed by 10 minutes in an O_2 plasma. These pieces were covered on two parallel edges with adhesive tape to control the film thickness. The TiO_2 paste was placed onto one of the free edges and distributed along the substrate with a glass rod to cover the whole surface area. One adhesive paste gave a 1 to 1.5 μm thick film. The samples were dried in air at 50 °C until the solvent was completely evaporated, followed by 5 minutes at 100 °C, and 10 minutes at 150 °C.

To obtain thicker films, multiple coatings were made. After drying, the films were slowly heated on a hot plate at 350 °C for 30 minutes to burn off the ethyl cellulose, followed by 500 °C for 1 hour under O_2. Before sensitizing with a dye, the layers were treated with $TiCl_4$. 2M of $TiCl_4$ solution in Millipore water was prepared at 0 °C to prevent the precipitation of TiO_2 which otherwise occurs in a highly exothermic hydrolysis reaction [4]. The stock solution was always kept in the freezer and a fresh 40 mM solution was prepared from the stock solution for every set of devices. The TiO_2 electrodes were inserted into a container with 40 mM $TiCl_4$ solution and were placed on a hot plate at 80 °C for 30 minutes. This results in a nucleation of nanometer sized TiO_2 particles on the TiO_2 films, increasing the active surface area [6]. The samples were washed with Millipore water and heated on a hot plate at 500 °C for 30 minutes in air and then cooled down to 70 °C. The samples ware soaked in a 0.5 mM ruthenium-complex dye solution over night. The sensitized layer and platinized FTO counter electrode with a 1 mm wide pinhole were assembled using a Surlyn[i] frame as spacer and seal, (Figure 3.6). The sandwiched electrodes were clamped together and heated to 100 °C causing the Surlyn to seal together the two electrodes. The liquid electrolyte

[i] http://www.dupont.com/industrial-polymers/surlyn

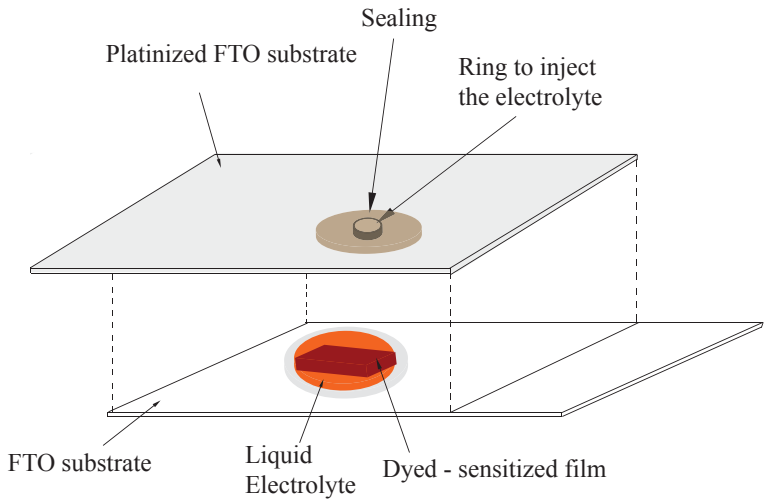

Figure 3.6: Schematic representation of a closed dye sensitized solar cell.

(Robust PMII) was injected through the small hole in the counter electrode. A funnel connected to a vacuum pump was placed above the cell creating a vacuum that drew the liquid into the cell. The electrolyte filled the space delimited by the Surlyn between the two electrodes. Finally the hole was sealed with polyimide kapton tape[ii].

[ii] http://www2.dupont.com/Kapton

Bibliography

[1] X. Chenn and S. Mao. Titanium dioxide nanomaterials: synthesis, properties, modifications, and applications. *Chem. Rev.*, 107:2891 2959, 2007.

[2] S. Ito, P. Chen, P. Comte, M. K. Nazeeruddin, P. Liska, P. Pechy, and M. Gratzel. Fabrication of screen-printing pastes from TiO_2 powders for dye-sensitized solar cells. *Progress in Photovoltaics: Research and Applications*, 2007.

[3] L. Kavan and M. Gratzel. Highly efficient semiconducting TiO_2 photoelectrodes prepared by aerosol pyrolysis. *Electrochimica Acta*, 40:643 652, 1995.

[4] L. Kavan, B. O Regan, A. Key, and M. Gratzel. Preparation of TiO_2 (anatase) films on electrodes by anodic axidative hydrolysis of $TiCl_3$. *J. Electroanal. Chem.*, 346:291 307, 1993.

[5] J. Lee, M. C. Orilall, S. C. Warren, M. Kamperman, F. J. DiSalvo, and U. Wiesner. Direct access to thermally stable and highly crys-

talline mesoporous transition-metal oxides with uniform pores. *Nat. Mater.*, doi:10.1038/nmat2111, 2008.

[6] M. K. Nazeeruddin, A. Kay, I. Rodicio, R. Humphry-Baker, E. Muller, P. Liska, N. Vlachopoulos, and M. Gratzel. Conversion of light to electricity by cis-X2Bis(2,2 -bipyridyl-4,4 -dicarboxylate-ruthenium(II) charge transfer sensitizers (X=Cl, Br, I, CN, and SCN) on nanocrystalline TiO_2 electrodes. *J. Am. Chem. Soc.*, 115:6382 6390, 1993.

[7] N. Papageorgiou, W. F. Maier, and M. Gratzel. An iodine/triiodide reduction electrocatalyst for aqueous and organic media. *J.Electrochem. Soc.*, 144:876 884, 1997.

[8] L. Schmidt-Mende, S. M. Zakeeruddin, and M. Gratzel. Efficiency improvement in solid-state-dye-sensitized photovoltaics with an amphiphilic ruthenium-dye. *Appl. Phys. Lett.*, 86:013504 3, 2005.

[9] R. Sherman, D. Hirt, and R. J. Vane. Surface cleaning with the carbon dioxide snow-jet. *J. Vac. Sci. Technol.*, 12:1876, 1996.

[10] H. J. Snaith and M. Gratzel. The role of a Schottky Barrier at an electron-collection electrode in solid state dye-sensitized solar cells. *Adv. Mater*, 18:1910 1914, 2006.

[11] H. J. Snaith, L. Schmidt-Mende, and M. Gratzel. Light intensity, temperature, and thickness dependence of the open-circuit voltage in solid-state dye-sensitized solar cells. *Phys. Rev. B.*, 74:045306, 2006.

[12] H. Kimura Suda, J. Zhang, T. Sassa, T. Wada, and H. Sasabe. Spin Coating. *Phys. Rev. Lett.*, 12:1196, 2000.

CHAPTER 4

Experimental Techniques

4.1 Atomic Force Microscopy

Atomic Force Microscopy (AFM) is an important new analytical technique, which is utilized to study the surface features of materials with a resolution down to the atomic level. Features such as the concentration of particles and the size distribution of particles can be measured by atomic force microscopy. In our experiments AFM was used to obtain information about the topography of polymer films. AFM was first described by Binning and Quate [1].

The atomic force microscope can be operated in different environments (in air, liquid, or vacuum) and in two primary modes (contact or non-contact) [4]. Whichever environment or mode, the basic operating principle of the AFM is the

same: the AFM uses a probe that consists of a micro-fabricated tip mounted on a flexible cantilever. The tip is slowly scanned across the surface of a material, a few Ångstroms away from the surface (non-contact mode) or in contact with it (contact mode). The force between the atoms of the surface and those of the tip cause the cantilever to deflect. The magnitude of the deflection depends on the separation between the surface atoms and the tip atoms, and on the atomic forces between them (van der Waals forces, Pauli exclusion forces, etc.).

At distances of a few nanometers, van der Waals forces are sufficiently strong to move macroscopic objects, such as an AFM tip mounted on a cantilever. Van der Waals forces are usually attractive and increase strongly with decreasing distance between atoms or molecules. The cantilever deflection can be recorded in various ways. The most common principle uses a laser which is focused on the back-side of the cantilever and is reflected onto a segmented photo diode. The photo-diode signals are used in a feed-back loop to control the tip-sample distance with a sub-Ångstrom resolution. By recording the vertical movement of the tip at a constant tip-sample force, the topography of the sample is measured with a resolution down to the atomic scale. The lateral and vertical movement of the tip or the sample are controlled by piezoelectric transducers (Figure 4.1).

In this study the AFM is used for surface imaging. Surfaces scans produce topographical maps with a lateral resolution down to 30 Å. AFM can be used to determine the surface roughness and grain sizes. It can resolve individual holes, defects (such as pinholes), and atomic clusters. It profiles samples in the real, three-dimensional space with vertical resolutions down to 0.1 Å [1]. By storing the digital information, the three-dimensional image of the surface can be manipulated, rotated, enhanced with color, filtered, enlarged, and displayed from any altitude or azimuth. The AFM is used to investigate a wide range of materials, including semiconductors, non-conducting surfaces, biological samples, high-resistivity materials, insulators, conducting samples, and features on micro-electronic devices.

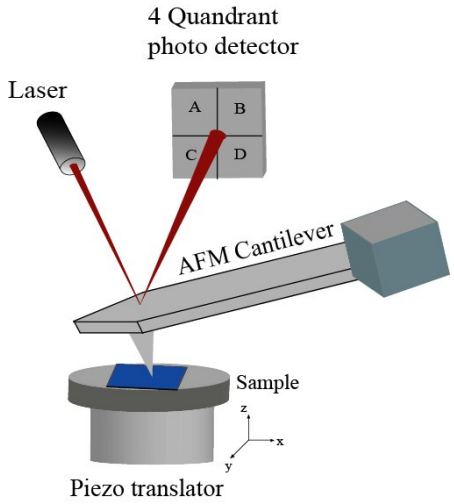

Figure 4.1: Schematic drawing of the main components of an AFM.

There are several modes of operation, but the most commonly used are Contact Mode AFM and Tapping Mode AFM.

In *Contact mode* AFM, the probe is scanned across a sample surface while monitoring the change in cantilever deflection with a segmented photodiode detector. A feedback loop maintains a constant cantilever deflection by vertically moving the scanner to maintain a constant photo diode voltage difference signal. The distance where the scanner moves vertically at each x, y data point is stored by the computer to form the topographic image of the sample surface. A feedback loop maintains a constant cantilever deflection and thereby a constant force during imaging, which typically ranges from 0.1 to 100 nN.

The mode of operation used in this thesis is the *Tapping Mode*, which consists of an oscillating the cantilever close to its resonance frequency (typically 300 kHz) during which comes into intermittent contact with the surface while scanning. The basic idea of the Tapping Mode is that the change in cantilever oscillation amplitude compared to the free oscillation is detected as the vibrating tip sweeps across the surface.

During Tapping Mode imaging, the vibrational frequency is set and the amplitude and phase of the oscillating tip are measured. The laser deflection method is

used to detect the root-mean-square (RMS) amplitude of cantilever oscillation. A feedback loop maintains a constant oscillation amplitude by vertically moving the scanner at each x, y data point. Recording this movement forms the topographical image.

The advantage of Tapping Mode AFM compared to Contact Mode AFM is that it reduces the lateral shear forces that are present in the Contact Mode. The Tapping Mode enables the imaging of soft, fragile, and adhesive surfaces without damaging them.

4.2 Magnetic Force Microscopy

Magnetic Force Microscopy (MFM) is a scanning probe microscopy technique that maps the spatial distribution of magnetism by measuring the magnetic interaction between a sample and a tip [5]. MFM measurements are based on non-contact AFM. A magnetic tip is mounted on a cantilever and scanned over the surface of the magnetic sample to obtain the topography. In the **Lift Mode**, the tip is lifted above the surface and scanned to observe the influence of the magnetic forces. These influences are measured using the principle of *force gradient detection*. If there are no magnetic forces, the cantilever has a resonant frequency f_0. In the presence of magnetic forces, the frequency is shifted by Δf which is proportional to the vertical force gradients. The magnetic tips have a frequency between 70-100 kHz. The shift in the resonant frequency is very small, in the range of 1-50 Hz. The frequency shifts can be detected in three ways:

- **Phase detection** - measures the cantilever s oscillations phase relative to the piezo actuation. It produces good results because of a good signal-to-noise ratio.

- **Amplitude detection** - which tracks the variations in the oscillation amplitude.

- **Frequency modulation** - which directly tracks shift in the resonant frequency.

The measurement data are acquired in two runs across each scan line. In the first run the topographical data are acquired in the Tapping Mode during the first trace and retrace, and on the second run the tip is lifted to a certain hight, usually to 30-100 nm and a second trace and retrace scan is done. The distance between the tip and the surface is always maintained constant. The magnetic interactions are detected in the second run.

4.3 X-Ray Diffraction

In order to investigate the phase composition of the inorganic films, -2υ scans were taken on a standard 2-circle diffractometer. To check the preferential out-of-plane orientation of crystals, scans (rocking curves) were taken on the same diffractometer. The 2 circle diffractometer was equipped with a monochromator for CuK_α radiation, consisting of a graphite (002) single crystal (Bruker) that fulfilled the Bragg condition for CuK_α.

The essential components of a X-ray diffractometer are:

- a source of X-rays, usually a sealed X-Ray tube;
- a goniometer;
- a X-ray detector;
- electronics for counting detector pulses in synchronization with the positions of the goniometer.

The operating voltage and current of the X-ray diffractometer were 40 kV and 40 mA, respectively.

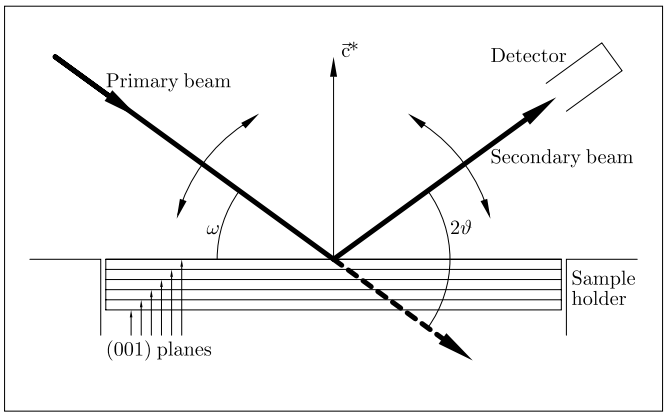

Figure 4.2: Schematic representation of -2υ scans. Curtesy of Ole Gobel [3].

4.3.1 -2υ Scans

is defined as the angle between the primary X-ray beam and the plane of the sample holder, Fig. 4.2. υ is the angle of reflection and is defined as the angle between the sample holder and the viewing direction of the detector. In normal -2υ scans these two angles are varied simultaneously from $_{\min}$ to $_{\max}$. When a single crystal substrate is placed onto the diffractometer with its c-axis normal to the sample holder plane, the detector registers the radiation of a diffracted beam only if the Bragg condition is fulfilled: $n\lambda = 2d_{(100)} \sin$ where:

- n is a natural number (positive integer);
- λ represents the X-ray wavelength;
- $d_{(100)}$ is the distance between adjacent (100) planes.

Because is always equal to the angle of reflection $= 2\upsilon$, this scan is called -2υ scan and the angle of incidence is called .

If a film with unoriented crystallites covers a single crystal substrate, the diffractogram of the sample will show the (00l) reflections of the single crystal and (hkl) reflections of the film. If a film that covers the crystal substrate was grown with a certain out-of-plane orientation (epitaxial orientation), the diffractogram

of the sample will show only $(00l)$ reflections of the single crystal substrate and $(00l)$ reflection of the film.

The X-ray scans shown in this thesis were taken with a Philips - PW1830 Generator 3.

4.4 Scanning Electron Microscopy

For scanning electron microscopy (SEM), the sample is placed into a high vacuum chamber and an electron beam generated by applying a voltage (kV) between the sample and a cathode is focussed onto the sample surface. The spot diameter depends on the current. Electrons impinging on the sample release, because of their high kinetic energy, secondary electrons. Some of the secondary electrons are emitted into the space above the sample and are collected by a detector. The spot can be moved over the sample surface by applying additional magnetic or electric fields. For imaging, the electron beam is scanned over the surface line by line. For each position x, y the intensity I of the detector signal is recorded and is displayed as an image $I(x\ y)$ which depends on the material properties of the illuminated spot area and the amount of emitted secondary electrons. The number of electrons that fall onto the detector depends on the presence and the size of obstacles between the electron spot and the detector.

To acquire SEM images, a LEO 15XXX field emission SEM was used. The distance between the sample and the objective lens, the working distance, was around 3 mm.

4.5 DC-SQUID Magnetometer

A Superconducting Quantum Interference Design magnetometer (SQUID magnetometer) was used for measuring the critical temperature T_c and the critical current density J_c. The SQUID allows us to measure hysteresis loops caused by

an applied magnetic field (H). J_c can be estimated from the width of the hysteresis loops at a given magnetic field and temperature using the critical state model. The advantage of the method is its high sensitivity, which allows the measurement of hysteresis loops even on individual filaments of superconducting nanostrustures.

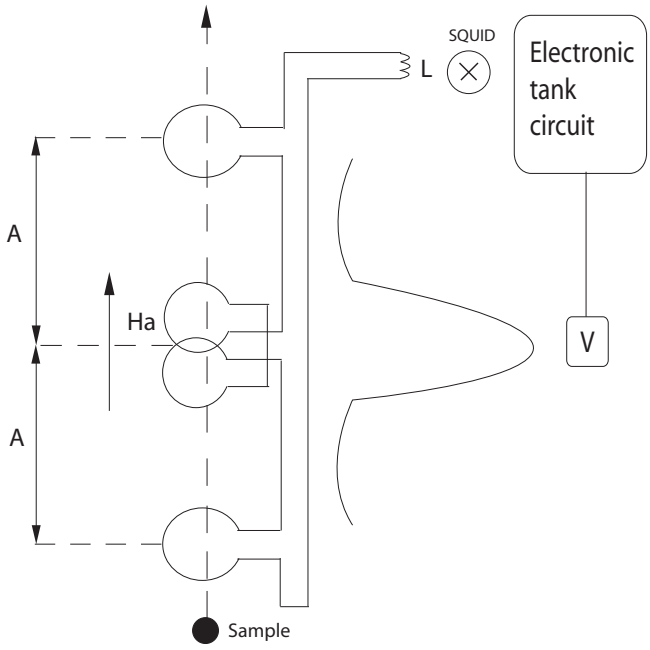

Figure 4.3: The schematic representation of a SQUID magnetometer

A SQUID consist of 4 superconducting detection coils that are designed to compensate the flux of the uniform field from a superconducting magnet. The planes of two outer detection loops are placed at a distance $\pm A$ from the center of the magnet, where two oppositely wound loops are situated. The magnetic field is set to a value of H and the sample is moved through this set of pickup coils. The magnetic moment m of the sample induces currents in these superconducting detection loops. The current passes through an inductance L generating a magnetic flux which is fed into a SQUID, resulting in an output voltage V in the electronic tank circuit, which depends on the z position of the sample, Fig. 4.3.

For the measurements the samples were cut in the form of small squares with

dimensions of about 4 mm×4 mm. The applied magnetic field was in the range of -4 T to 4 T at a temperature of 6K. Critical current densities can be determined by using the relation:

$$J_c(H) = \frac{\Delta M(x)}{a(1 - \frac{a}{3b})} \tag{4.1}$$

where:

- ΔM is the vertical width of the hysteresis loop of the given magnetic field;
- $2a \times 2b$ $(b > a)$ represents the rectangle cross section

4.6 Absorption Spectroscopy

Absorption spectroscopy is a technique where the intensity of a beam of light measured before and after interaction with a sample is compared. In UV and visible spectroscopy the amount of light of a particular wavelength absorbed by a sample is compared.

This technique was used in this report to characterize the optical density of the mesoporous TiO_2 samples.

4.7 Device Characterization

The photovoltaic devices were characterized under low light intensity (external quantum efficiency under monochromatic light) and simulated full sun light (current-voltage measurements).

4.7.1 External Quantum Efficiency

The external quantum efficiency (EQE) or the incident-photon-to-electron conversion efficiency (IPCE) is measured under monochromatic light and is defined as the ratio of the number of electrons generated by the solar cell to the number

of incident photons on the active surface [7].

$$EQE(\lambda) = \frac{n_{\text{electrons}}(\lambda)}{n_{\text{photons}}(\lambda)} = \frac{I(\lambda)\ e}{P_{\text{in}}(\lambda)\ h\nu} = \frac{I(\lambda)}{\lambda P_{\text{in}}(\lambda)} \frac{hc}{\nu} \tag{4.2}$$

where, $I(\lambda)$ is the electric current generated by the cell at wavelength λ, $P_{\text{in}}(\lambda)$ is the incoming light power at wavelength λ and λ is the wavelength of the incident irradiation. The EQE is measured under short-circuit conditions and is graphically displayed versus the corresponding wavelength in a photovoltaic action spectrum.

The EQE was measured with a halogen lamp (spectrally resolved by a monochromator) illuminating the solar cells from the FTO side, at an intensity of 0.1 mWcm^{-2} at each wavelength interval. The photocurrent was measured using a Keithly 237 source meter interfaced with a computer. The illumination spot size was 1 mm^2.

4.7.2 Current-Voltage Measurements

A solar cell can be considered as a two terminal device which behaves as a diode in the dark generating a photovoltage when illuminated by the sun [6]. The current-voltage characteristics of a photovoltaic device is shown in Figure 4.4 and can be approximated as the sum of the short circuit photocurrent and the dark current. The short-circuit current (J_{SC}) is the current measured when cathode and anode are directly connected.

The open-circuit voltage (V_{OC}) is the voltage created between the electrodes when the device is illuminated with unconnected anode and cathode.

The performance regime of a solar cell is the bias range of 0 to V_{OC} in which the power is generated. The cell output power density is the product of the measured cell current density and the bias voltage:

$$P = JV \tag{4.3}$$

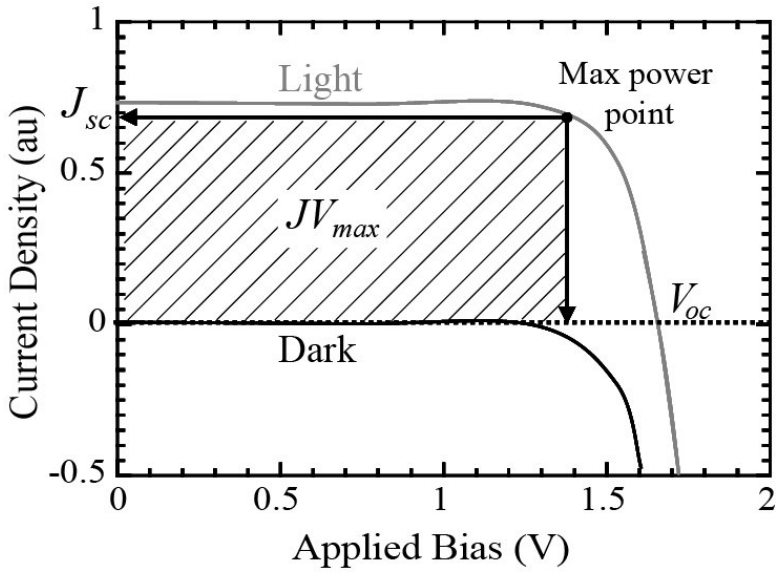

Figure 4.4: Schematic presentation of current voltage characteristics of a solar cell. The grey line represents the light current and the black line represents the dark current. The maximum power output is given by the hatched area [9].

and P is the maximum power point which occurs at V_{m} and J_{m} shown in Figure 4.4.

The *fill factor* describes the squarness of the $J-V$ curve which is given by:

$$FF = \frac{J_{\mathrm{m}} V_{\mathrm{m}}}{J_{\mathrm{SC}} V_{\mathrm{OC}}} \tag{4.4}$$

The *power conversion efficiency* η of a photovoltaic device under sun light can be calculated if J_{SC}, V_{OC} and FF are known , using the formula:

$$\eta = \frac{J_{\mathrm{SC}} V_{\mathrm{OC}} FF}{P_{\mathrm{in}}} \tag{4.5}$$

η is the estimated ratio between maximal electric output power to the power of incident illumination.

To obtain an efficient solar cell, J_{SC}, V_{OC} and FF have to be maximized. The simulated solar sun light AM 1.5 was generated by a 300 W Oriel solar simulator with the corresponding AM 0 and AM 1.5 filters. The intensity of the

solar simulator was calibrated using a Si calibration diode purchased from and calibrated by the Fraunhofer Institute for Solar Energy System. The spectral mismatch was calculated over the entire absorbtion area of the test cell and the calibration of the diode following the method of Seaman [8]. The measured area of ~ 13 cm^2 of a liquid eletrolyte based DSCs were determined by a black optical mask. The active area of a solid-state DSCs was defined by the overlap of the silver cathode with the FTO anode to approximately 0.04 cm^2.

4.8 BET Measurements

The so-called BET method is used to estimate the surface area, porosity and pore size distributions of porous materials. The name comes from the three scientists Brunauer, Emmett and Teller [2] who optimized the theory of measuring surface area using adsorbed gas molecules as rulers .

Powder materials were placed into a vacuum chamber at the temperature of liquid nitrogen, 77 K. The method used to determine the pore size distribution was gas sorption (adsorption and desorption) of the dry powder material, using N_2 as the adsorbing gas. In a gas sorption experiment, the material is heated and degassed by vacuum or inert gas purging to remove the adsorbed molecules. The amount of gas molecules adsorbed or desorbed are determined by the pressure variations due to the adsorption or desorption of the molecules by the adsorbing material.

The surface area of the material can be determined using the formula:

$$S = N_{\mathrm{A}} n_{\mathrm{m}} \sigma \tag{4.6}$$

where, N_{A} is the Avogadro s number, n_{m} is the monolayer capacity (moles of molecules needed to make a monolayer coverage on the surface of one gram of adsorbent) and σ is the area occupied by one adsorbate molecule ($\sigma = 16\ 2$ Å for

N_2).

The surface area determined by gas sorption is between 0.01-2000 m^2/g. The pore size and pore distribution can be determined from the adsorption (desorption) isotherm. The size of the pores that can be determined by this method is from a few Å up to 0.5 micrometers.

Bibliography

[1] G. Binning and C. F. Quate. Atomic force microscopy. *Phys. Rev. Lett.*, 56 (9):930 933, 1986.

[2] S. Brunauer, P. H. Emmett, and E. Teller. Adsorption of gases in multimolecular layers. *J. Am .Chem. Soc.*, 60:309 311, 1938.

[3] Ole F. Gobel. *The growth of patterned ceramic thin films from polymer precursor solutions.* PhD thesis, University of Groningen, 2004.

[4] G. Hangstad and R. P. Jones. Atomic force microscopy. *Ultramicroscopy*, 77:77, 1999.

[5] http://en.wikipedia.org.

[6] Jenny Nelson. *The physics of solar cells.* Imperial College Press, 2003.

[7] Robert Plass. *Nanoparticles sensitisation of solid-state nanocrystalline solar cell.* PhD thesis, Ecole Polytechnique Federale de Lausanne, 2004.

[8] C. Seaman. Calibration of solar cells by the reference cell method - the spectral mismatch problem. *Solar Energy*, 29:291 298, 1982.

[9] Henry J. Snaith. *Polymer based photovoltaic diodes.* PhD thesis, University of Cambridge, 2004.

CHAPTER 5

Direct Electron Beam Writing of Nickel Patterns

5.1 Introduction

Ferromagnetic materials are widely investigated due to the numerous technological applications in media for magnetic recording or as magnetoresistive heads [2]. There is an immense interest in fabricating nano-sized structures, because of the expected to enormous technological demand for these materials in the future. Nickel is one of the most explored ferromagnetic materials. It can be produced by different methods such as sputtering [2], chemical vapor deposition (CVD) [4], or electrochemical deposition [8]. A variety of nano-sized structures such as nanobelts, nanowires, or nanorings were created. The fabrication of Ni nanowires require a template such as a porous polycarbonate membrane [5], anodic alumina

oxide (AAO) [3], or carbon nanotubes onto which Ni is deposited by electrochemical deposition, CVD, or sputtering. These techniques require more work than the direct writing of the material, as a template has to be made first. Saifullah *et al.* [6] have shown that metal naphthenate resists, *i.e.* Zn naphthenate, can be patterned on the sub-10 nm scale using direct-writing electron beam lithography. Metal naphthenates contain cyclopentanes or cyclohexanes, methylene chains [-(CH_2)-], carboxilates, and metal. They have the chemical formula: [(cyclopentane)-$(CH_2)_n$-COO]$^{-m}$-M^{m+}, where M is the metal. M can be Zn, Ni, Fe, Cu, etc. The naphthenate materials are viscous liquids, which are stable in air and toluene.

In this work we obtained metallic nickel by spin-coating a nickel naphthenate resist and pattern this resist using direct-writing electron beam lithography. Direct-writing electron beam lithography offers the ability to write patterns with down to sub-10 nm dimensions. The conventional technique to pattern metals or metal oxides using electron beam lithography involves producing a pattern in a resist such as PMMA, evaporating the requisite material, followed by lifting-off the mask. The success of the lift-off step is not guaranteed in particular if higher temperatures are required for depositing the metal on a patterned resist.

5.2 Experimental Details

Ferromagnetic nickel films were produced by dissolving Ni naphthenate in toluene in the ratio 1:1 and 2:1 by volume. The obtained solution was spin-coated with 3000 rpm for 2 min. onto silicon wafers. The silicon wafers were cleaned by snow-jet [7] and then covered by spin-coating (3000 rpm, 1 min.) with a layer of hexamethyldisilazane (HMDS) to achieve a good adhesion of the naphthenate resist onto the substrate. To transform the Ni naphthenate into pure Ni metal, the samples were pyrolyzed in a tube furnace at 500 °C for 1 hour under an Ar/H_2 (40:60) mixture with a heating rate of 3 degrees/min. A higher amount of H_2 in argon is necessary to reduce the napthenate to metallic films. The film

thickness varies between 50 and 100 nm with the concentration of Ni naphthenate in toluene.

For the electron-beam lithography, the Ni naphthenate was diluted in toluene in a 1 to 20 ratio (by volume) and films were produced according to the procedure described above.

5.3 Results and Discussions

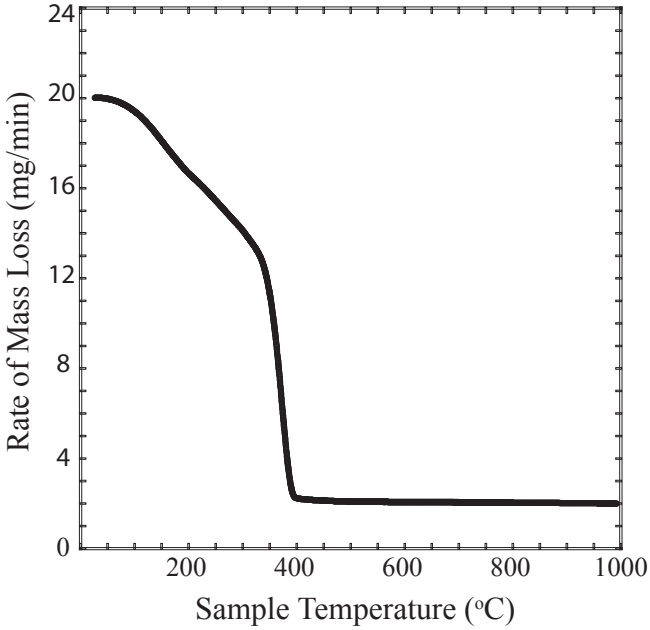

Figure 5.1: TGA curve of nickel naphthenate as a function of the annealing temperature.

The pyrolysis process of the Ni naphthenate was investigated by thermogravimetric analysis (TGA) shown in Figure 5.1. The as received, the material was heated at different temperatures under Ar gas and the rate of mass loss was measured. It was observed that between 100 - 200 °C there is a loss of the mineral spirits, while at around 400 °C there is a loss of all of the organic material. From 450 °C up to 1000 °C the crystalline phase of Ni is obtained.

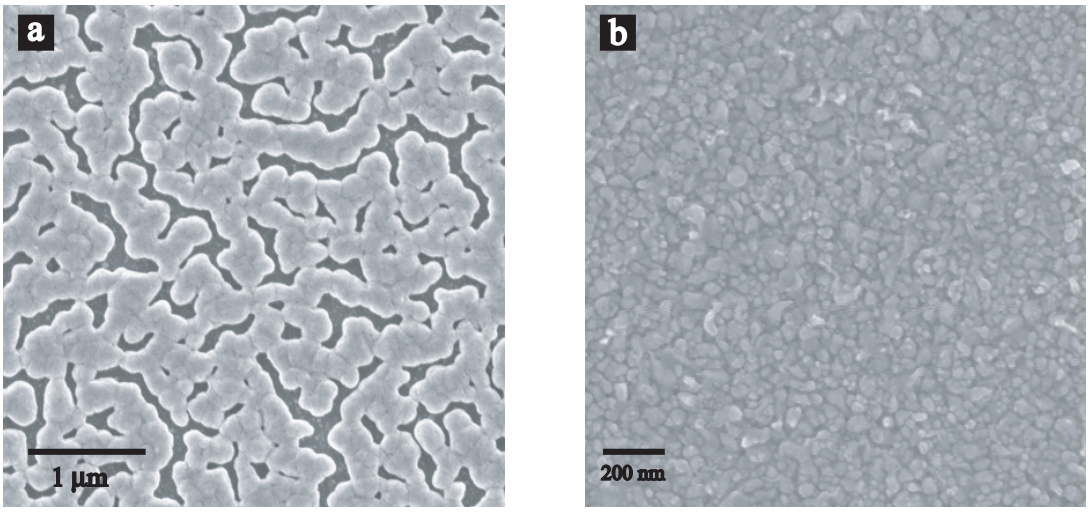

*Figure 5.2: SEM images if Ni metal films. (**a**) Morphology of a 50 nm Ni film showing islands, (**b**) morphology of a 100 nm Ni film presenting a compact layer.*

After calcination at 500 °C, the films were analyzed by scanning electron beam lithography (SEM), X-ray powder diffraction and magnetic force microscopy (MFM). The SEM scans of two films with different morphologies are shown in Figure 5.2. The morphology of the Ni films depends on the thickness of the film. The image in Figure 5.2 (a) shows a 50 nm thick film. The film is not continuous and consists of islands. These islands are composed of many smaller particles having sizes between 80 and 120 nm. Yi *et al.* [10] have obtained Ni islands for 15 nm thick films, while voids were seen for 50 nm thick films. In their case the Ni films, were made by a sputtering technique. The morphology of the films therefore depends on their thickness and on the procedure to make them. In our case Ni was obtained by spin-coating a viscous solution containing a large amount of organic materials and only 8 % of Ni. During the calcination process, all organic components are removed. Thin films do not contain enough metal to cover the entire surface area. With increasing the film thickness, the islands disappear and a continuous crystalline film is formed (Figure 5.2 (b)). The particles size of the polycrystalline film increases with increasing the films thickness. For a 100 nm

thick film, the particle size lies between 100 and 200 nm.

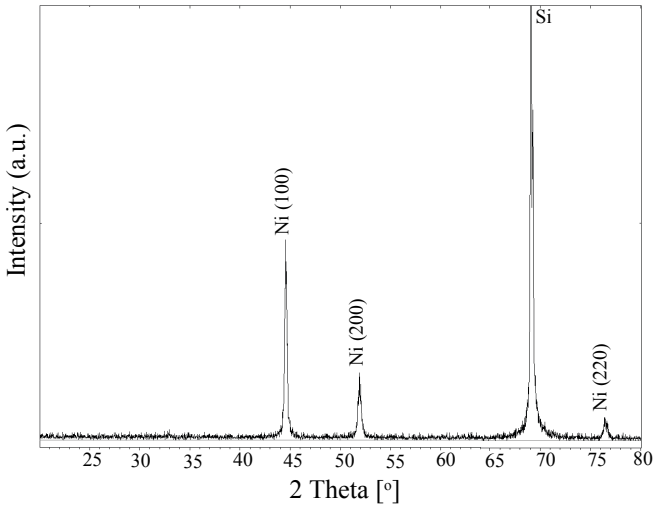

Figure 5.3: X-ray diffraction spectrum of a 90 nm thick Ni film.

Ni films were analyzed by X-ray powder diffraction to identify the orientation of the crystals (Figure 5.3). The film consists of polycrystalline FCC-packed Ni. As the highest peak is the (100) peak, the crystals have a preferential orientation along the $\overrightarrow{a}$ axis normal to the film plane. Since all peaks in the XRD spectrum can be attributed to metallic Ni, the film is free of crystalline nickel oxides.

To investigate the magnetic properties of our films, a DC SQUID magnetometer was used. The magnetization curve function of the applied magnetic field is shown in Figure 5.4.

A magnetic field of $\pm$ 4 Tesla was applied perpendicular to the sample. The magnetization saturation (M_s) of the 90 nm thick Ni film is around 430 emu/cm^3, which is slightly lower than the value for bulk Ni, 480 emu/cm^3. The magnetization saturation increases with increasing the film thickness. Figure 5.4 shows the M_s curve of the film as a function of the applied magnetic field. The coercivity of the film is around 340 Oe. This value indicates that the films consist of crystalline Ni. Mixtures of amorphous and crystalline phases, have a lower magnetization saturation and a higher coercivity [10]. These changes of the magnetic properties

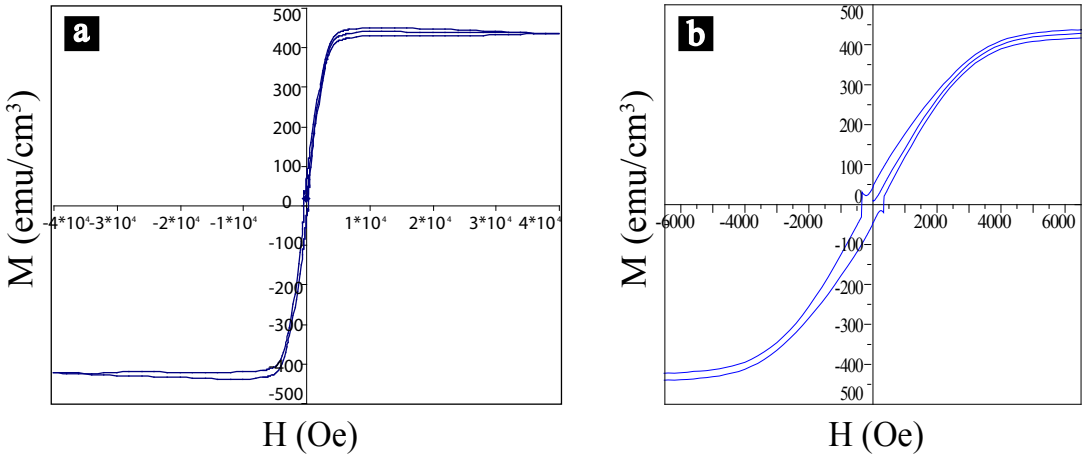

*Figure 5.4: Magnetization curve of a 90 nm thick Ni film function of the applied magnetic field. (**a**) The hysteresis loop of the film shows its coercivity. The curve in (**b**) is a magnification of the central part of the curve of (**a**).*

in the Ni films are due to the disordered structure in the thin films caused by the amorphous phase.

Magnetic force microscopy (MFM) was used to investigate the magnetic domains of a 100 nm thick Ni film. Figure 5.5 (a) shows the topography of the film, while the Figure 5.5 (b) is the corresponding MFM scan. The MFM picture shows bright and dark domains. The bright magnetic domains indicate an attraction between the Ni film and the magnetic tip. The dark domains arise from tip repulsion. The stripes in the magnetic domains possibly arise from the change in the orientation of the magnetic spins in the film during the scan.

There are two types of the magnetic domains orientation, in-plane and out-of-plane, both of which can be seen by MFM. Franco *et al.* [1] have shown both types of ferromagnetic domains in CoFe-AgCu films. The out-of-plane domains were formed when the films exerted a stronger magnetic field. When the films exerted a weak magnetic field, 10 kOe were applied perpendicular to the film in order to increase the strength of the magnetic field. Therefore, the MFM phase of these films showed long - stripe domains. The ferromagnetic in-plane domains are metastable, and the film demagnetizes in about one month. The out-of-plane

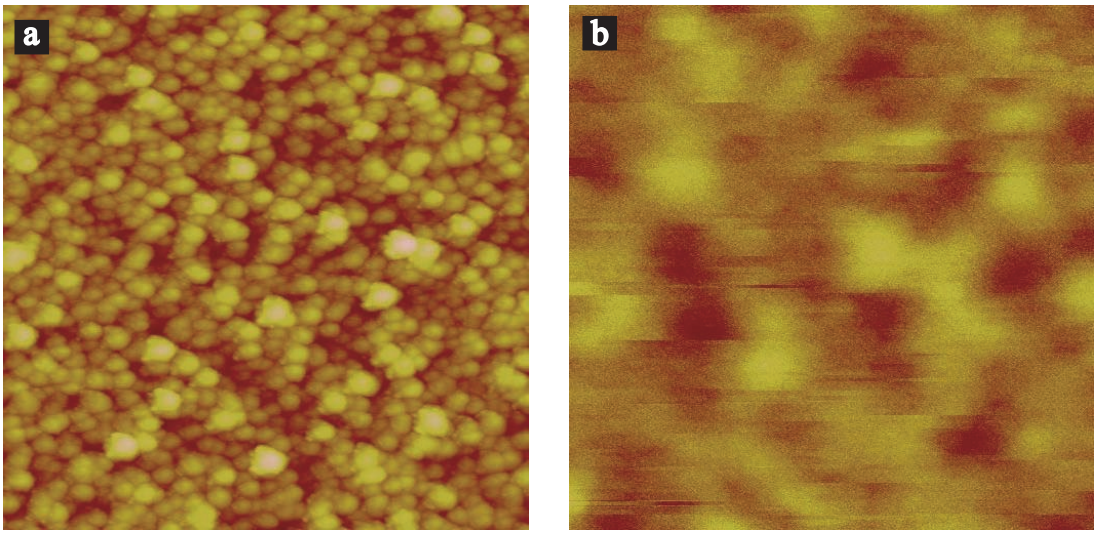

*Figure 5.5: Magnetic force microscopy image of a Ni film. (**a**) the topography, (**b**) magnetic contrast. The image sizes are* 5×5 μm^2.

domains are stable for a longer time, over one year. If we compare the MFM image in Figure 5.5 with the images presented by Franco *et al.* we can deduce that our ferromagnetic domains have an in-plane orientation and a lack of clearly defined domain shapes compared to the out-of-plane domains of Ni films.

The electrical resistivity of Ni films was calculated using the formula:

$$\rho = R_{\square} d \tag{5.1}$$

where $R_{\square}$ is the sheet resistance and d is the film thickness.

The sheet resistance was measured using a four-point probe. These measurements were done in collaboration with Dr. David Hasko, from the microelectronics group. The four-point probe instrument is used to measure the average resistance of a thin layer. There are four contacts on the sample and the current which comes from a high impedance passes through the two outside points. The voltage is measured across the two inside points using a voltmeter. At room temperature the sheet resistance for a 88 nm thick film was $R_{\square} = 0\ 537\ \Omega\square$, yielding a resis-

tivity of $\rho = 47\ 25 \times 10^{-6}\ \Omega\Box$. To test whether the sample was ferromagnetic, the measurement of the sheet resistance was also measured under liquid nitrogen, at T = 77 K. $R_\Box$ under liquid nitrogen was $R_\Box = 0\ 3\ \Omega\Box$, yielding $\rho = 26\ 4 \times 10^{-6}$ $\Omega\Box$. A decrease in the resistivity with decreasing the measuring temperature indicates that the film was ferromagnetic. The resistivity of bulk Ni lies in the range $6\ 85 - 7\ 78 \times 10^{-6}\ \Omega\Box$. The resistivity of nickel decreases with increasing the film thickness, and also depends on the film roughness. The high values for films are due to the small film thickness and the roughness.

Nickel structures were fabricated using direct-writing electron beam lithography. With this technique nano-sized structures, below 10 nm can be obtained. This kind of lithography system is formed from an electron gun, focussing condensor lenses, a beam blanker unit, a beam deflection unit, and a stage holder for the substrate [9]. The electrons are emitted from the gun and travel along the electron - optical axis with high velocities caused by high acceleration voltage used to write the structures. The condensor lenses are situated along the optical axis and have the role to focus the electrons into a fine beam, named the electron probe .

To be able to directly write structures into a resist film using electron beam lithography, the sensitivity of the resist to the electron beam and the contrast of the exposure have to be known. To measure these parameters, Ni naphthenate resist was spin-coated onto a Si wafer and structured using an electron beam. The exposed resist was developed in toluene for 10 seconds and the step height of the exposed area was measured using an atomic force microscope.

In Figure 5.6 the exposure curve of the Ni naphthenate resist is shown. The sensitivity $D_{0.5}$ (which is the dose of electrons impinge onto the sample by an electron beam probe of 0.5 nm diameter) is around 9 mCcm^{-2} and the contrast γ (which is the sharpness of the image obtained from the solubility/insolubility after development) is 1.43. Kakimi *et al.* have studied the influence of the electron beam on the naphthenate resist using infrared absorption spectroscopy. They found

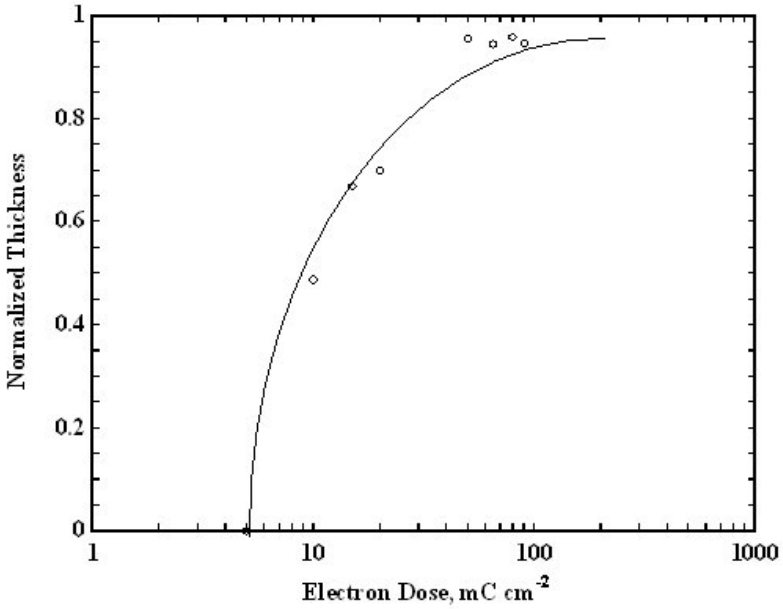

Figure 5.6: Electron beam sensitivity of nickel naphthenate.

that the naphthenate molecules exposed to an electron beam crosslink, forming -C=O and/or -$(CH_2)_n$ groups, making the exposed resist insoluble in toluene by increasing the molecular weight of the resist.

Figure 5.7 shows several structures written with an electron beam into a Ni naphthenate resist before and after annealing to transform the naphthenate material into pure Ni. The width of these structures written with this technique is between 10 and 14 nm. In initial experiments an electron dose of 10 $mCcm^{-2}$ was used, resulting in mechanically fragile structures due to the surface tension forces during the development and the blow drying. To obtain standing lines, the dose of electrons was increased by a factor of 3-4. After structuring the Ni naphthenate, the sample was developed in toluene for 10 seconds to remove the non exposed material and the patterns shown in Figure 5.7 (a) and (c) were obtained. These samples were heat-treated at 500 °C for one hour in an Ar/H_2 (40:60) atmosphere

to produce pure Ni lines. After heating all the organic materials were removed and the width of the lines of the Ni arrays was 7-9 nm, (Figure 5.7 (b) and (d)). Keeping the sample in the air, rendered electrical measurements impractical because of the rapid oxidation of the lines.

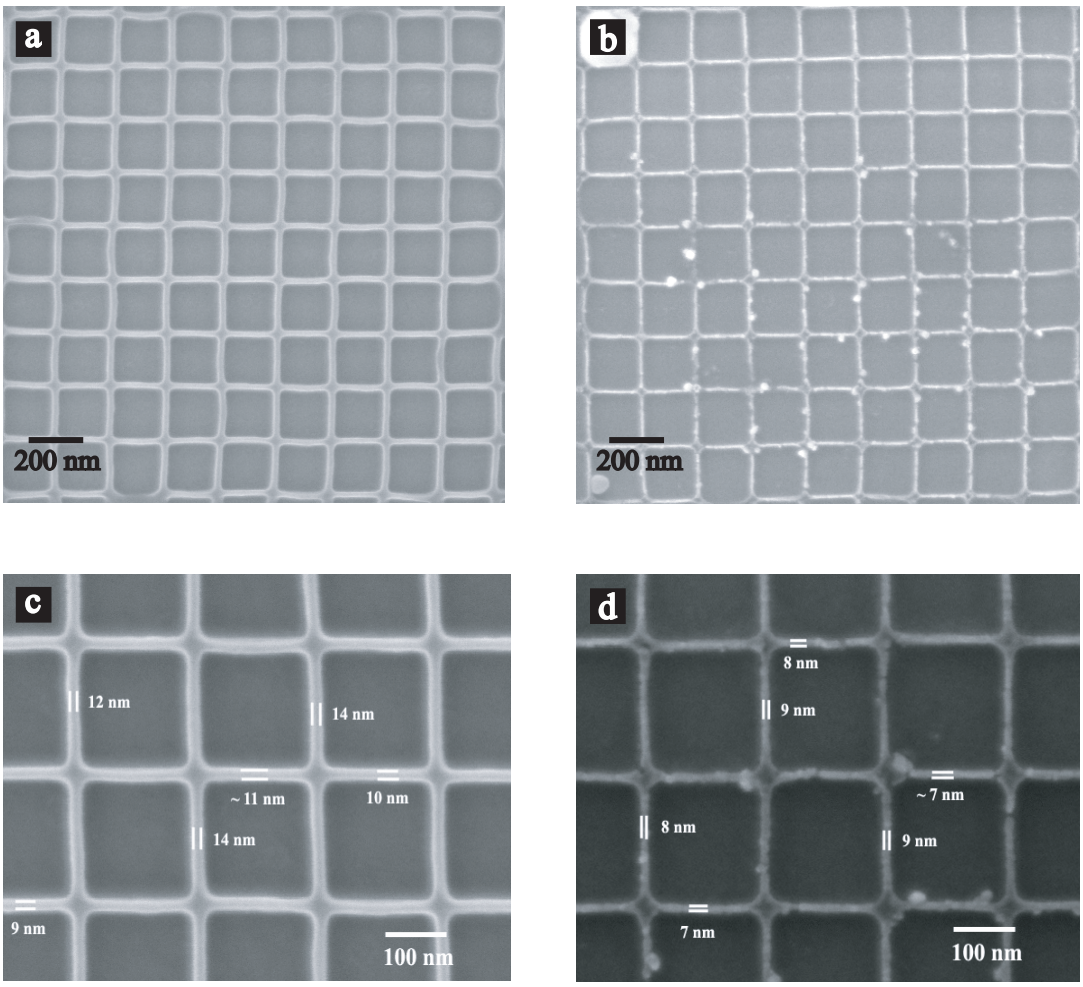

*Figure 5.7: SEM images of structured nickel naphthenate. (**a**) Lines of Ni naphthenate before annealing, (**b**) Ni lines after heating in an Ar/H_2 atmosphere, (**c**) 10-14 nm wide Ni naphthenate lines before heating, (**d**), 7-9 nm wide Ni lines after heating.*

5.4 Conclusions

In summary we have shown that pure Ni metal can be obtained by spin-coating a naphthenate resist onto a Si wafer substrate. The Ni films gave a magnetization saturation of 430 emu/cm^3 and a coercivity of 340 Oe. The electrical resistivity of these films was 47 25 $\times$ 10^{-6} Ω4cm for a 90 nm thick film. Using electron beam lithography, 10 - 14 nm wide lines were written. After heating at 500 °C, a slightly reduction in the line width to 7 - 9 nm was seen. In air the sub-10 nm lines oxidized and the electric and magnetic properties could not be measured. This indicates that Ni structures with a sub-10 nm structure size are impractical and therefore thicker structures are required.

Bibliography

[1] V. Franco, X. Batlle, and A. Labarta. Evidence of domain wall scattering in thin films of granular CoFe-AgCu. *Eur. Phys. J. B.*, 17:43 50, 2000.

[2] B. Ghebouli, A. Layadi, and L. Kerkache. Effect of the substrate on the structural and electrical properties of dc sputtered Ni thin films. *Eur. Phys. J. Ap.*, 3:35 39, 1998.

[3] M. J. Kim, Y. W. Kim, J. S. Lee, J.-B. Yoo, and C.-Y. Park. Magnetic properties of nickel nanostructures fabricated using anodic aluminium oxide templates. *J. Korean. Phys. Soc.*, 47:313 317, 2005.

[4] T. Maruyama and T. Tago. Nickel thin films prepared by chemical vapor deposition from nickel acetylacetonate. *J. Mater. Sci.*, 28:5345 5348, 1993.

[5] S. Pignard, G. Goglio, A. Radulescu, L. Piraux, S. Dubois, A. Declemy, and J. L. Duvail. Study of the magnetization reversal in individual nickel nanowires. *J. Appl. Phys.*, 87:824 829, 2000.

[6] M. S. M. Saifullah, K. R. V. Subramanian, D.-J. Kang, D. Anderson, W. T. S. Huck, G. A. C. Jones, and M. E. Welland. Sub-10 nm high aspect ratio patterning of zinc oxide using electron beam. *Adv. Mater.*, 17:1757 1761, 2005.

[7] R. Sherman, D. Hirt, and R. J. Vane. Surface cleaning with the carbon dioxide snow-jet. *J. Vac. Sci. Technol.*, 12:1876, 1996.

[8] L. Sun, P. C. Searson, and C. L. Chien. Magnetic anisotropy in prismatic nickel nanowires. *Appl. Phys. Lett.*, 79:4429 4431, 2001.

[9] K. R. Venkatsubramanian. *Spin coatable oxide resist for electron beam nanolithography.* PhD thesis, University of Cambridge, 2005.

[10] J. B. Yi, Y. Z. Zhou, J. Ding, G. M. Chow, Z. L. Dong, T. White, X. Y. Gao, A. T. S. Wee, and X. J. Yu. An investigation of structure, magnetic properties and magnetoresistance of Ni films prepared by sputtering. *J. Mag. Mag. Mater.*, 284:303 311, 2004.

CHAPTER 6

Solid State Dye Sensitized Solar Cells Fabricated with Mesoporous TiO_2

6.1 Introduction

The morphology of TiO_2 plays an important role in the efficiency of dye sensitized solid state solar cells. Here, we describe the use of poly(isoprene-*b*-ethylene oxide) (PI-PEO) block-copolymer as structure directing agents for the manufacture of TiO_2 mesoporous layers. A Ti-containing organic precursor molecule complexes to the PEO moiety of the block-copolymer, thereby assuming the microphase morphology of the copolymer. The morphology and average pore size of the TiO_2 mesoporous layer can be controlled by the molecular weight of the polymer and the relative amount of added precursor. The film porosity which is controlled by

the molecular weights of a diblock-copolymer and the amount of added titania precursor is shown to influence the performance of dye sensitized solar cells based on mesoporous TiO_2 layers. A device on a 1.1 μm thick mesoporous TiO_2 layer with an optimized microphase morphology showed a power conversion efficiency of 1.5 % under simulated sun light.

Mesoporous materials [12, 14] have been widely investigated during the last decade due to their applications in photoelectrochemical cells, photocatalysis, and sensors. TiO_2 is one of the most popular materials because it is cheap, widely available, and biocompatible. In 1991, Gratzel reported the use of TiO_2 in dye-sensitized solar cell devices (DSC) for the first time [6]. These cells were made from mesoporous TiO_2 nanoparticles, sensitized with a light absorbing dye, and filled with a liquid electrolyte, a iodide/triidide based solution. In 1998, Bach and Gratzel discovered another approach to the manufacture of DSCs by replacing the liquid electrolyte with an organic hole transporter (Spiro-MeOTAD) thereby preventing the possible leakage of the liquid electrolyte. These devices are now known as solid state dye sensitized solar cells (SSDSC) [1]. Spiro-MeOTAD is the most efficient organic hole transporter because of its good charge mobility [7]. The highest reported efficiency of SSDSCs is over 5 % [9]. Considerable previous research has been done to improve the morphology of TiO_2 by mixing organic-inorganic hybrid materials which can increase the efficiency of solar cells [2, 3, 15]. The organic materials are removed by calcination under air leaving a mesoporous structure. The disadvantage of this method is the collapse of the pores at temperatures higher than 400 °C and a lower crystallinity for lower calcination temperatures. To maximize the performance of the photocatalytic devices, the structure of the material has to have a maximal surface area to absorb the dye and a minimal amount of inorganic material which can trap and lead to recombination of the photo-excited electrons and holes. To improve the structural integrity and to improve the crystallinity during high temperature annealing the diblock copolymer PI-PEO was combined with precursor materials for the synthesis of

mesoporous inorganic materials [4, 5, 11, 13]. In our case, the diblock copolymer was mixed with sols of the group IV transition metal oxides, which selectively swell the hydrophilic (PEO) block [5]. PI on the other hand contains double bonds. During calcination, PEO is easily decomposed, while PI, which contains two sp^2 electrons per monomer is transformed into graphitic carbon in an inert atmosphere (argon), which acts as a scaffold for the pores preventing the structure collapse when annealed at temperatures higher than 400 °C. The combination of these specific functionalities of the two blocks are highly advantageous for the manufacture of DSCs: the compartmentalization of the Ti-precursor leads to the divided nature of the TiO_2 phase (on the 10-nm length scale), while the ability to calcinate the material at high temperature leads to a high degree of its crystallinity, thereby meeting the two requirements which are typically difficult to combine.

6.2 Experimental Details

The TiO_2 films described in this work were prepared as follows. Block copolymers (PI-PEO) of different molecular weights (M_w = 15 5 kg/mol with 22.7 % PEO, M_w = 33 5 kg/mol with 23 % PEO, M_w = 84 4 kg/mol with 14.4 % PEO) were dissolved in anhydrous tetrahydrofuran (THF). $TiCl_4$ and Ti isopropoxide (purchased from Aldrich) were added and stirred for about 2 hours. Ti isopropoxide is the main source of titania, while $TiCl_4$ was added to adjust the pH to 1-2. The titania precursor selectively swells only the PEO block of the block copolymer, and a continuous PI minority phase in a matrix of PEO with Ti precursor was obtained. The details regarding the disolution proces of alkoxides in PEO are described elsewhere [5]. The ratio between polymer and the titania precursor was 2:1 by weight. To increase the porosity of the films, the amount of Ti precursor was reduced with respect to the initial 2:1 ratio by 25 %, 50 %, and 75 %, respectively. The volume ratio between polymer and precursor therefore was 2:0.75, 2:0.5, and 2:0.2, respectively. The films were spin-coated onto fluorine doped SnO_2 (FTO)

coated glass sheets (sheet resistance 15 Ω □). The fabrication of the substrates are described in Chapter 3.3. After spin-coating, the films were placed onto a hot plate at 100 °C for about 1 hour to evaporate the solvent. They were then transferred into a tube furnace for high-temperature processing (450 - 600 °C) for 2 hours under an argon inert atmosphere. During this process, the PEO is burnt off and PI is transformed into graphitic carbon which coats on the pores preventing the collapse [5]. To remove the carbon, the samples were heated under oxygen at 500 °C for 1 hour. The film thicknesses of 500 nm - 2 μm of the spin-coated layer was as a function of the molecular weight of the diblock copolymer and the amount of added titania precursor.

The dye sensitized solar cells were assembled as follows: prior to sensitizing in the dye solution, the TiO_2 films were treated in a mild piranha solution (1 part of Millipore water, 3 parts of sulphuric acid and 2 parts of hydrogen peroxide) for 30 minutes at 50 °C, followed by rinsing with Millipore water, immersion for 1 minute in ethanol, and drying in a N_2 flow. After this treatment, the TiO_2 films were soaked in a 3×10^{-4} M dye solution of the amphiphilic polypyridil ruthenium complex, cis-RuLL $(SCN)^2$ (L=4,4 -dicarboxilic-acid-2,2 bipyridine, L=4,4 -dinonyl-2,2 -bipyridine) (Z907) in acetonitril:tert-butanol (1:1 vol %) at room temperature [8]. The hole transporting material used for the devices was 2,2 7,7 -tetrakis (N,N -di-methoxypheny-amine)-9,9 -spirobifluorene (Spiro-MeOTAD), dissolved in chlo robenzene (180 mg/mL) and mixed with $Li[CF_3SO_2]_2N$, tert.-butylpyridine and $N(PhBr)_3SbCl_6$ [10]. The tert.-butylpyridine and lithium ions were added to help to increase the cell performance. The dyed films were rinsed in acetonitrile and dried in air for 1 minute. The Spiro-MeOTAD solution (70 μl) was deposited on top of the film and left for 40 seconds to penetrate in the pores before spining off the remaining solution. The samples were placed in an evaporator where 200 nm of silver were deposited through a shadow mask. Before device fabrication, the TiO_2 was characterized by X-ray powder diffraction, scanning electron microscopy (SEM). The photovoltaic properties of the solar cells were characterized

by recording the current-voltage characteristics of the solar cell in the dark and under simulated sun light AM 1.5 (100 mWcm^{-2}).

6.3 Results and Discussions

It is generally assumed that an increasing TiO_2 crystallinity will improve the efficiency of DSCs. We therefore prepared a series of mesoporous TiO_2 samples calcinated at temperatures in the range of 400 - 600 °C and DSCs were made from these layers. The solar cell performance of the resulting devices were measured. For these measurements, the ratio between copolymer

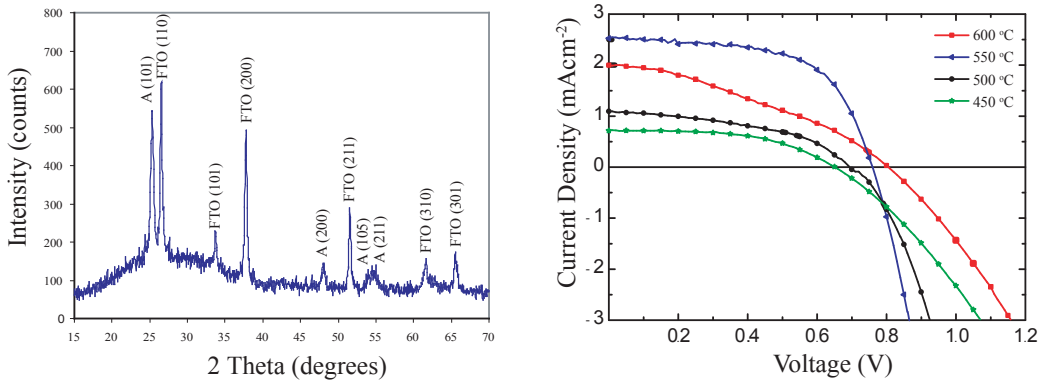

Figure 6.1: ***(a)*** *XRD of a TiO_2 film;* ***(b)*** *Photocurrent-voltage characteristics of the solar cells fabricated with mesoporous TiO_2 films calcinated at different temperatures.*

(M_w = 15 5 K) and the titania precursor was 2:1, and the film thickness was around 1 μm. The DSCs characteristics measured were: current-density measured at short circuit (J_{SC}), voltage measured at open circuit (V_{OC}), the fill factor (FF) which is the squarness of the $J-V$ curve, and the power conversion efficiency (η) which is the ratio between the power output and the power input. Under simulated full sun light, the best performance was obtained for mesoporous TiO_2 heated at 550 °C. In this case $J_{SC} = 2\ 54$ mA/cm^2, $V_{OC} = 0\ 76$ V, $FF = 0\ 61$ and $\eta = 1\ 17\%$.

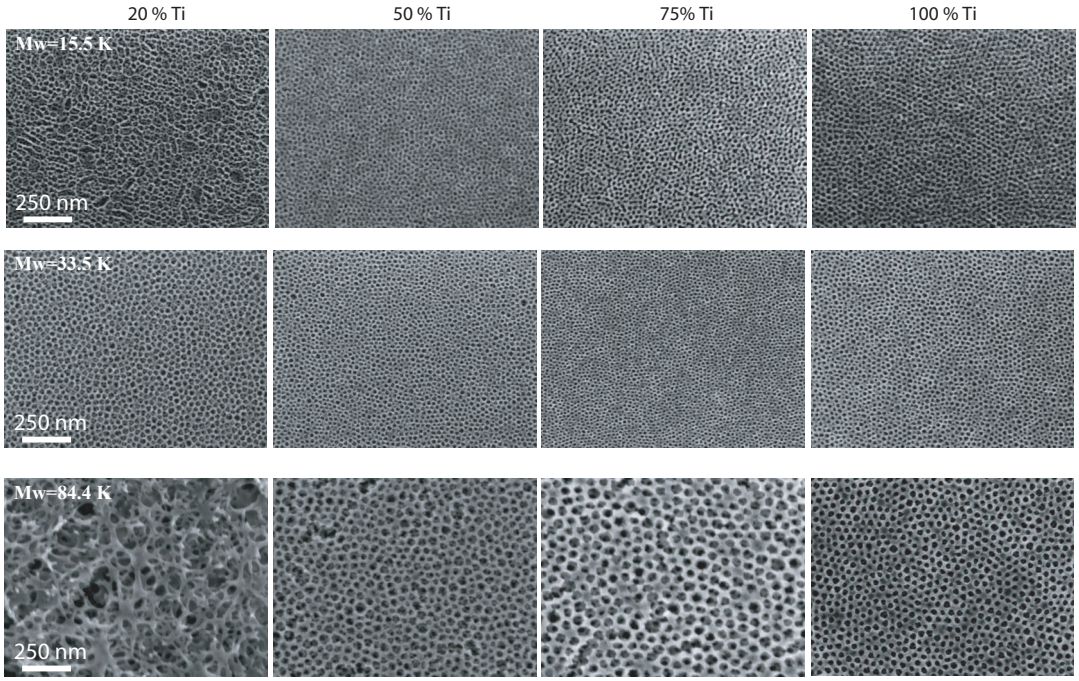

Figure 6.2: Scanning electron microscopy images of mesoporous TiO_2 films as a function of molecular weights of diblock copolymer and added titania precursor.

For even higher calcination temperatures (i.e. 600 °C) a lower device performance was found Figure 6.1 (b). This is possible due to the de-doping of the FTO substrate.

XRD scans of films were done to identify the phase of TiO_2 and to calculate the crystal size (Figure 6.1 (a)). From 450 °C to 600 °C only the anatase phase was found. The crystal size calculated with Debye-Scherer formula for the 25.25 ° is around 13 nm.

Figure 6.2 shows the SEM images of mesoporous TiO_2 layers as a function of different molecular weights of diblock copolymer and the amount of added Ti-precursor. The three rows correspond to the three polymer molecular weights of M_w = 15 5 kg/mol, M_w = 33 5 kg/mol, M_w = 84 4 kg/mol , while the four columns show films, with increasing amount of precursor, corresponding to polymer - precursor weight ratios of 2:0.2, 2:0.5, 2:0.75, and 2:1, respectively.

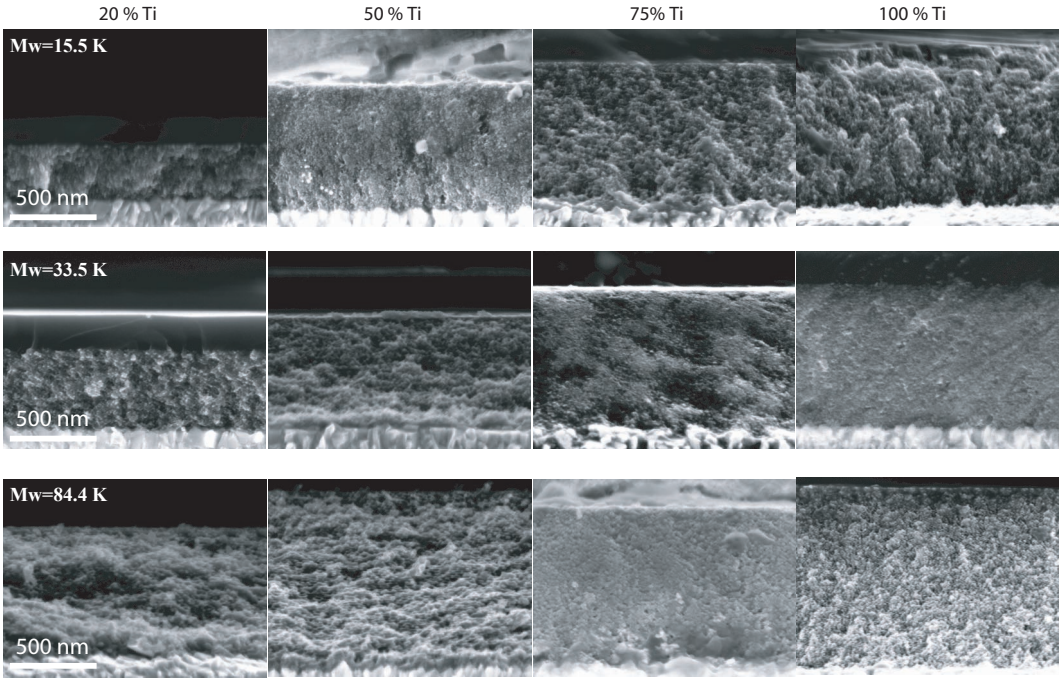

Figure 6.3: Cross-sections images of mesoporous TiO_2 films function of different molecular weights of diblock copolymer and changes of the amount of titania.

The top view of the first row (M_w = 15 5 kg/mol) show a cellular looking pattern for the composition ratios of 2:0.5, 2:0.75, and the 2:1 mixture shows an ordered phase. Close examination of the cross-sectional images in Figure 6.3 reveals that the pores are interconnected. For the highest precursor content, the pores size is around 15 nm and it increases with decreasing amount of precursor.

For the 2:0.5 composition ratio, the pore size is slightly larger, around 18 nm. The morphology of the sample with the lowest precursor content differed slightly. The pores are less well ordered, exhibiting a worm-like morphology. The SEM images in the second row correspond to PI-PEO with a molecular weight of M_w = 33 5 kg mol^{-1}. In this case all the images show a continuous structure with increasing pores sizes as a function of the decreasing ratio of added Ti-precursor. For the highest precursor content the pore size is around 30 nm increasing to around 35 nm for the left-most images. The film thickness decreased

from 1.5 μm to 750 nm, right to the left. In the third row, the mesoporous TiO_2 SEM images correspond to PI-PEO with M_w = 84 4 Kg mol^{-1}. The pores are larger, around 70 nm for the highest precursor content. The morphology again shows an inter connected cellular structure for all polymer precursor ratios except for the 2:0.2 ratio which exhibits a spider-web morphology. The film thickness decreased as a function of decreasing amount of precursor from 2 μm to 1.2 μm.

BET measurements were performed to characterize the internal pore areas of the mesoporous films. The pore area of film made with the M_w = 15 5 kg/mol decreased from 35 m^2/g to 30 m^2/g with decreasing the precursor content, mirroring the increasing pore size from 15 nm to 18 nm. For the films made with the M_w = 33 5 kg/mol, the surface area varied from 70 m^2/g to 63 m^2/g, while for the highest molecular weight of the copolymer, M_w = 84 4 kg/mol the pore area were around 77 m^2/g for all ratios of added precursors. All these samples were incorporated into dye sensitized solid state solar cells. After calcination in the furnace the films with the lowest precursor content did not show any cracks, while all the others showed some cracks. It seems that films thicker than 800 - 900 nm exhibit cracking. The crack - width was around 1-1.5 μm. The crack pattern is not expected to affect the cell performance.

Figure 6.4 shows the absorption spectra of PI-PEO films (M_w = 15 5 kg mol^{-1}) dyed with Z 907 with increasing the amount of Ti-precursor. Except for the polymer precursor ratio, all other parameters were kept constant. Figure 2 reveals an increase in absorbed light, and therefore an increase in dye adsorbtion with increasing the amount of Ti-precursor.

Figure 6.5 (a) shows the external quantum efficiency (EQE) photovoltaic action spectra, defined as the ratio of collected electrons to incident photons, for devices made with the lowest molecular weight copolymer as a function of decreasing the amount of Ti-precursor. The spectra shows an increase in collected electrons with increasing pore size. For the 15 nm pores, a maximum EQE of 7 % is reached at 532 nm, while for the lowest precursor content leading to 18 nm

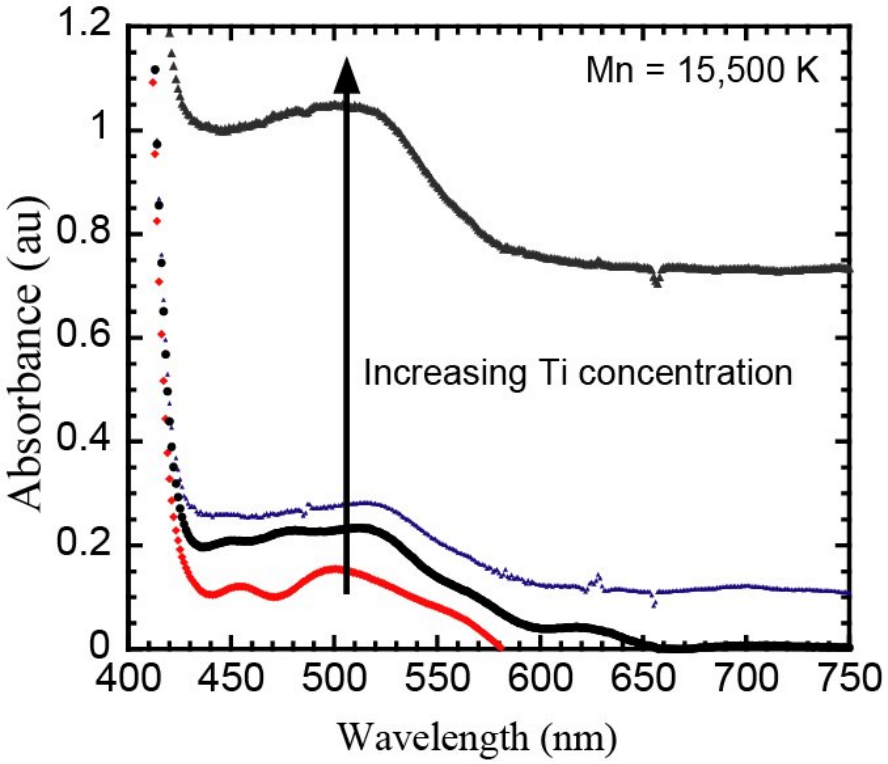

Figure 6.4: Light absorbance for PI-b-PEO, M_w = 15 5 kg/mol as a function of increasing Ti-precursor amount.

pore size, the maximum EQE was 22 % at 531 nm. For the devices made with the M_w = 33 5 kg mol^{-1} polymer, the EQE results were similar to those shown in Figure 3.

The current density-voltage characteristics were measured for all the films shown in Figure 2, in the dark and under simulated full sun light AM 1.5, 100 mWcm^{-2}. $J - V$ curves for the best performing devices made with two polymer molecular weights and the same precursor ratio of 2:0.5 are presented in Figure 6.5 (b). The best performing devices were obtained from PI-PEO with M_w = 33 5 kg mol^{-1} and a precursor ratio of 2:0.5. The power conversion efficiency for a 1.1 μm thick film was η = 1 50 %, the photocurrent-density was J_{SC} = 2 96 mAcm^{-2}, the open-circuit voltage was V_{OC} = 0 80 V, and the fill - factor was FF = 0 63. For the lower molecular weight of PI-PEO with the same precursor amount, J_{SC} = 2 17

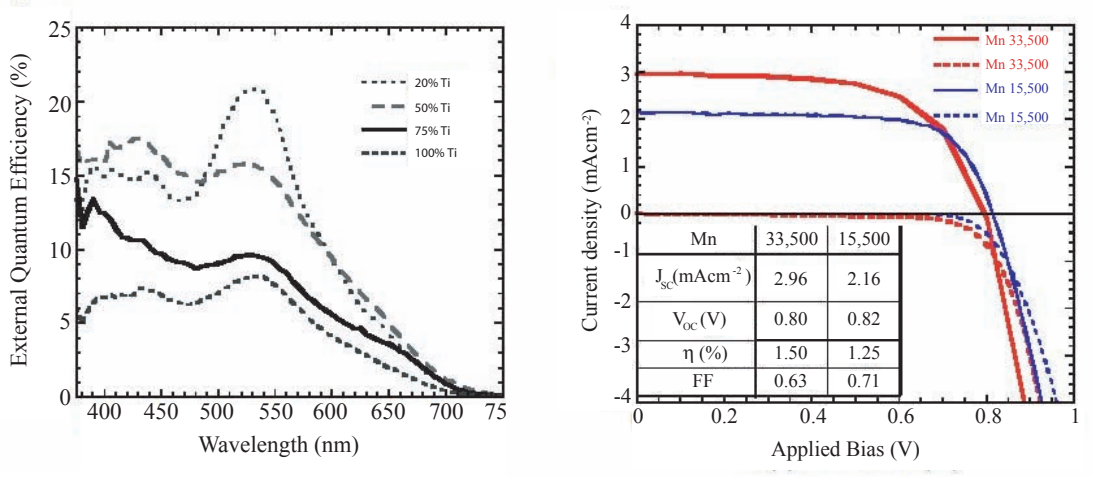

Figure 6.5: ***(a)*** *External Quantum Efficiency photovoltaic action spectra for devices made with the M_w = 15 5 kg mol^{-1} polymer as a function of decreasing the amount of Ti-precursor,* ***(b)****Photocurrent-voltage characteristics of solar cells for two different devices as a function of the porosity of TiO_2 measured under simulated full sun light AM 1.5 illumination at 100 mW cm^{-2}. Red curves are for TiO_2 films made with the M_w = 33 5 kg mol^{-1} block-copolymer and 50 % Ti-precursor. Blue curves are for TiO_2 films made with the M_w = 15 5 Kg mol^{-1} polymer and the same amount of Ti-precursor.*

mAcm^{-2}, V_{OC} = 0 82 V, and FF = 0 71 were measured. This device yielded a power conversion efficiency of η = 1 25 % for a 1 μm thick film. The lower efficiency obtained for the M_w = 15 5 kg mol^{-1} polymer is probably due to smaller pore size which may cause a reduced infiltration of the Spiro hole transporter into the pores. The cells made with the highest molecular weight PI-PEO did not perform well. They adsorbed dye, but the Spiro-MeOTAD hole transporter solution dewetted during spin-coating onto the mesoporous TiO_2 substrates. This might be due to the larger pores and a potential super-hydrophobic effect caused by the pore structure.

Our results have to be compared to the best performance of dye sensitized solid state solar cells based on a nanoparticle assembly using the same Z-907 and the same hole transporter Spiro-MeOTAD of over 5 % for 2 μm thick films [9].

6.4 Conclusions

In conclusion we have shown that we can control the morphology and pore size of mesoporous TiO_2 films by a one-pot approach consisting of a PI-PEO diblock-copolymer mixed with a titania precursor. Using this mixture, mesoporous TiO_2 layers were made, which were incorporated into solid state dye sensitized solar cells. A power conversion efficiency of 1.5 % was obtained for a 1.2 μm thick film made using a PI-PEO molecular weight of 33.5 kg mol^{-1} and a polymer-precursor weight of 2:0.5. It is likely that the efficiency of our devices can be further improved if thicker films can be obtained and if a dye with a higher absorption coefficient will be used.

Bibliography

[1] U. Bach, D. Lupo, P. Comte, J. E. Moser, F. Weissortel, J. Salbeck, H. Spreitzer, and M. Gratzel. Solid-state dye-sensitized mesoporous TiO_2 solar cells with high photon-to-electron conversion efficiencies. *Nature*, 395:583 585, 1998.

[2] K. M. Coakley, Y. Liu, M. D. McGehee, K. L. Frindell, and G. D. Stucky. Infiltrating semiconducting polymers into self-assembled mesoporous titania films for photovoltaic applications. *Adv.Funct. Mater.*, 13:301 306, 2003.

[3] K. M. Coakley and M. D. McGehee. Photovoltaic cells made from conjugated polymers infiltrated into mesoporous titania. *Appl. Phys. Lett.*, 83:3380 3382, 2003.

[4] C. Garcia, Y. Zhang, F. DiSalvo, and U. Wiesner. Mesoporous aluminosilicate materials with superparamagnetic gamma-Fe_2O_3 particles embedded in the walls. *Angew. Chem. Int. Ed.*, 42:1526 1530, 2003.

[5] J. Lee, M. C. Orilall, S. C. Warren, M. Kamperman, F. J. DiSalvo, and U. Wiesner. Direct access to thermally stable and highly crystalline mesoporous transition-metal oxides with uniform pores. *Nat. Mater.*, doi:10.1038/nmat2111, 2008.

[6] B. O Regan and M. Gratzel. A low-cost, high efficiency solar based in dye-sensitized solloidal TiO_2 films. *Nature*, 353:737 739, 1991.

[7] D. Poplavskyy and J. Nelson. Nondispersive hole transport in amorphous films of methoxy-spirofluorene-arylamine organic compound. *J. Appl. Phys.*, 93:341 346, 2003.

[8] L. Schmidt-Mende, S. M. Zakeeruddin, and M. Gratzel. Efficiency improvement in solid-state-dye-sensitized photovoltaics with an amphiphilic Ruthenium-dye. *Appl. Phys. Lett.*, 86:013504, 2005.

[9] H. J. Snaith, A. J. Moule, C. Klein, K. Meerholz, R. F. Friend, and M. Gratzel. Efficiency enhancements in solid-state hybrid solar cells via reduced charge recombination and increased light capture. *Nano Lett.*, 7:3372 3376, 2007.

[10] H. J. Snaith, L. Schmidt-Mende, M. Chiesa, and M. Gratzel. Light intensity, temperature, and thickness dependence of the open-circuit voltage in solid-state dye-sensitized solar cells. *Phys. Rev. B.*, 74:045306, 2006.

[11] M. Templin, A. Franck, A. D. Chesne, H. Leist, Y. Zhang, R. Ulrich, V. Schadler, and U. Wiesner. Organically modified aluminosilicate mesostructures from block copolymer phases. *Science*, 278:1795 1798, 1997.

[12] B. Tian, X. Liu, B. To, C. Yu, J. Fan, L. Wang, S. Xie, G. D. Stucky, and D. Zhao. Self-adjusted synthesis of ordered stable mesoporous minerals by acid-base pairs. *Nat. Mater.*, 2:159 163, 2003.

[13] S. C. Warren, F. J. DiSalvo, and U. Wiesner. Nanoparticles-tuned assembly and disassembly of mesostructured silica hybrids. *Nat. Mater.*, 6:156 161, 2007.

[14] P. Yang, D. Zhao, D. I. Margolese, B. F. Chmelka, and G. D. Stucky. Generalized syntheses of large-pore mesoporous metal oxides with semicrystalline frameworks. *Nature*, 396:152 155, 1998.

[15] M. Zukalova, A. Zukal, L. Kavan, M. K. Nazeeruddin, P. Liska, and M. Gratzel. Organized mesoporous TiO_2 flms exhibiting greatly enhanced performance in dye-sensitized solar cells. *Nano Lett.*, 5:1789 1792, 2005.

CHAPTER 7

Dye Sensitized Solar Cells Fabricated with TiO_2 Paste

7.1 Introduction

Since the advent of the space-race, an enormous amount of work has focused on developing highly efficient, durable photovoltaic technologies. Over recent years, with the realization of an impeding fuel shortage and the need for clean renewable sources of energy, considerable efforts were made to reduce the cost of solar cells by primarily addressing the material processing techniques. Photo-electrochemical solar cells are an emerging photovoltaic technology which could revolutionise this industry. Dye-sensitized solar cells (DSCs), invented by O Regan and Gratzel in 1991 [13], are composed of a low cost mesoporous n-type metal oxide, typically

TiO_2, the pigment used in white paint. Sensitization of this oxide with dye-molecules, subsequent infilling with a redox active liquid electrolyte, and capping with a Pt counter electrode completes the device. Electrons are injected into the metal oxide following the optical excitation of the dye. The redox active electrolyte regenerates the oxidized dye species with the holes carried back to the counter electrode to complete the circuit. Because light absorption takes place in only a monolayer of dye, an extremely large internal surface area is required to enable complete light absorption in reasonably thin layer, typically 1000 times the surface area of the device. This is usually achieved by forming mesoporous films from sol-gel processed sintered nanoparticles with a surface roughness of approximately 100 fold per micron thickness [6, 11, 13]. Achieving the correct pore structure, good interconnection between the particles, and suitably low surface-state defect densities are likely to be critical for a further improvement of the efficiency, reproducibility, and longevity of these solar cells. The mesoporous films fabricated from sol-gel processed nanoparticles have been remarkably successful. However, after twenty years of optimization, further improvements are not directly forceable. Recently, extensive developments in the material sciences has enabled the synthesis of mesoporous materials using block-copolymers as structure directing agents [10, 21, 24]. In principle, this method for mesoporous material synthesis should enable a greatly enhanced control of the pore size, uniformity, and interconnectivity and has already been shown to enable the fabrication of highly efficient solar cells [12, 26]. A range of approaches for obtaining mesoporous inorganic materials structured by block-copolymers exist: A block-copolymer can be used as a sacrificial template. Selectively degrading one of the blocks and backfilling the remaining porous polymer template with the required material via electrochemical deposition, chemical vapor deposition, or thermal deposition, and removal of the sacrificial polymer results in the creation of a close to identical replication of the original block-copolymer morphology [4, 22]. For a more simple approach, hydrophilic-*b*-hydrophobic copolymers can be mixed directly in solution

with metal salts to act as structure directing agents. The metal-oxide precursors preferentially associate with the hydrophilic block, swelling this phase. Upon heating, hydrolysis and calcination occurs, forming an organic-inorganic hybrid material with the metal hydroxide or oxide replicating the morphology of the hydrophilic phase. Further heating, chemical washing, or plasma etching removes the polymer leaving a pure mesoporous metal oxide. Previously, it has been shown that highly crystalline mesoporous materials with no structural collapse can be obtained by mixing an amphiphilic diblock-copolymer poly(isoprene-block-ethylene oxide) (PI-*b*-PEO) with inorganic materials which preferentially swell the PEO block [5, 10, 16, 21].

The potential benefits of using diblock copolymers to structure mesoporous materials are clear. However, due to the slow kinetics in solid films, structure formation usually requires long processing times (days) and often high temperatures (up to 1000 °C). Furthermore, obtaining films with thicknesses in excess of one micro-meter is non-trivial due to the unavoidable material contraction and induced stresses during the hydrolysis and calcination processes [3, 26]. From these considerations, commercial success of applying these methods to large area, low-cost thin film fabrication appears unlikely. Here, we address this processing issue and develop a mesoporous material fabrication protocol which separates the slow stages of mesopore formation and calcination from film fabrication. The mesoporous material is formed as a monolith, with subsequent reconstitution with solvent and binder as a paste which is readily applicable for rapid thin film coating. The paste, which is composed of preformed, precrystalized mesoporous particules of predetermined scale and morphology, can form robust up to 30 μm thick films.

7.2 Experimental section

Mesoporous TiO_2 was prepared as described previously by Lee *et al.* [10]. Poly(isoprene-*b*-ethylene oxide) (PI-*b*-PEO) with a range of molecular weights, M_w = 15 5 kg/mol, 22.7 wt % PEO, M_w = 33 5 kg/mol, 23 wt % PEO and M_w = 84 4 kg/mol, 14.4 wt % PEO was dissolved in THF and mixed with titanium isopropoxide and $TiCl_4$ in a ratio of 1:1.5 by mass and stirred for at least 2 hours. The solution was placed onto a hot plate at 50 °C for more than 24 hours to slowly evaporate the solvent, then in a vacuum oven at 130 °C for 2 hours to completely remove the solvent and other volatile components. To convert the titania precursor into TiO_2, the material was transferred into a tube furnace for high temperature processing at 525 °C for 2 hours under an inert (argon) atmosphere with a ramping rate of 1 degree/min. During this process PI was transformed into amorphous carbon coats acting as a scaffold preventing pore collapse [10] The carbon was removed by heating the material at 525 °C for 5 hours under O_2.

After cooling, the mesoporous TiO_2 monolith was ground in a mortar until a fine powder was obtained. This TiO_2 powder was incorporated into a paste, as described in the Chapter 3.7.

The mesoporous TiO_2 powder was characterized by X-ray diffraction spectroscopy (XRD) using a Philips PW 1830 Generator 3 and specific nitrogen adsorbtion (BET). The TiO_2 films were characterized with scanning electron microscopy (SEM) using a LEO 15xxx at an acceleration voltage of 5 kV and with high resolution transmission electron microscopy (HRTEM) using a JEOL 4000EX microscope, with 400 kV acceleration voltage and a point resolution of 0.17 nm.

Fluorine doped SnO_2 (FTO) coated glass sheets (Pilkington, TEC15) were manually cleaned with Halmenex soap, acetone and isopropanol followed by 10 minutes in an O_2 plasma etcher. The mesoporous TiO_2 pastes were applied by doctor-blading. Two parallel strips of Scotch tape we adhered to the edge of the FTO sheets to control height of the doctor-blade. The paste was dispensed

onto one end of the glass sheet with a cylindrical glass pipette used as the doctor blade, which was manually rolled along the Scotch tape strips, coating the entire substrate. A doctor blade height of one Scotch tape (70μm) gave an approximately 1-1.5 μm thick dry film. For thicker films up to three Scotch tapes were used at once. The coated sheets were dried in air at 50 °C until the solvent was completely evaporated, then at 100 °C for 5 min, followed by 10 min at 150 °C. For thicker films this process was repeated many times. The samples were slowly heated on a hot plate to 350 °C for 30 minutes to burn off the ethyl cellulose, then at 500 °C for 1 hour under O_2 to ensure good interconnection between the particules. The samples were soaked in a 40 mM $TiCl_4$ solution at 80 °C for 30 min. The films were then cleaned in Millipore water, dried, and heated to 500 °C for 30 min in air. They were cooled to 80 °C before immersing into a 0.5 mM solution of cis-di(thiocyanato)-bis(2,2 -bipyridyl-4-carboxylate-4 -carboxylic acid)-ruthenium(II) dye (termed N719) in a mixture of acetonitrile:*tert*-butyl alcohol (volume ratio 1:1) and kept in the dark over night at room temperature.

The counter electrodes used for these devices were fabricated as described in the Chapter 3.3, liquid electrolyte was prepared as presented in the Chapter 3.8 and the DSCs assembled as detailed in the Chapter 3.9.2.

The solar cells were measured under AM 1.5 simulated sun light generated by a 300 W Oriel solar simulator using AM 0 and AM 1.5 filters. The power of the simulated light was calibrated using a Si calibration diode which was calibrated by and purchased from the Frounhofer Institute for Solar Energy System. The mismatch factor to the solar spectrum was calculated over the entire spectral responsive region of both the test solar cells and calibration diode following the method of Seaman [15]. The active area of the DSCs, defined by a black optical mask, was 0.13 cm^2. The external quantum efficiency (EQE) measurements were done using a halogen lamp which was spectrally resolved through a monochromator, with the intensity calibrated using a Si diode. The cells were illuminated from the FTO side at an approximate intensity of 0.1 $mWcm^{-2}$ at

each wavelength interval, with an illumination spot size of approximately 1 mm^2. The current-voltage measurements were recorded on a Kiethley 237 sourcemeter, which was interfaced by a PC. Transient open-circuit voltage and transient short-circuit photocurrent measurements were performed as previously described [17]. Here, a single red light emitting diode (630 nm peak) was used as the background and perturbation source, focused to give a maximum intensity of around 100 $mWcm^{-2}$. The square wave perturbation (1 ms width) was kept to a minimum intensity such that it could be considered to be small. The voltage signal was recorded through the high impedance port (1 MΩ) of an Agilent Technologies oscilloscope. The transient short-circuit photocurrent was recorded through the low impedance port (50 Ω). For measuring the voltage perturbation at short-circuit, a Kiethley 237 sourcemeter was connected in series with the solar cell, and used to hold the current constant, which was equivalent to short-circuit current under the bias light, following a light pulse. The voltage perturbation across the solar cell was recorded by connecting this circuit in parallel with the high impedance port on the oscilloscope, i.e. measuring the voltage purturbation across the solar cell when no extra current is allowed to flow following the light pulse.

7.3 Results and discussion

Following the preparation of mesoporous TiO_2, monoliths the TiO_2 powder was characterized with XRD to probe the crystal phase, size, and crystallinity of the material. For annealing temperatures below 700°C we only observe the anatase crystal structure, with crystal sizes of around 13 nm calculated by the Debye-Scherrer peak width analysis. An XRD spectrum for the mesoporous TiO_2 powder obtained with the M_w = 33 5 kg/mol PI-*b*-PEO heated to 525 °C is shown in Figure 7.1. For crystallization performed above 750 °C, signatures of the rutile phase started to appear, coinciding with a slight growth in crystal size.

We note that the retention of the porosity and crystal size up to this temper-

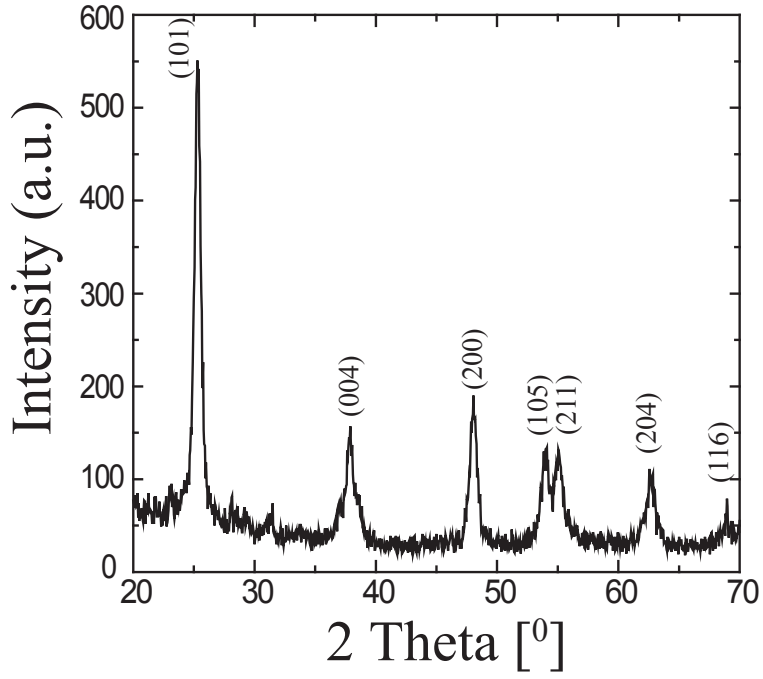

Figure 7.1: X-ray diffraction pattern of a mesoporous TiO_2 powder made using PI-b-PEO with a molecular weight of 33.5 kg/mol, heated at 525 °C.

ature is a consequence of the carbon scaffold [10].

Figure 7.2 shows SEM and HRTEM images of mesoporous TiO_2 films, and the spectral transmission of light. Figure 7.2 (a) shows a SEM image of a film fabricated from the above mentioned pastes. We observe very rough films comprised of a range of sizes of particules. We note that zooming in on a macroscopic particulate reveals a mesoporous composition. Figure 7.2 (b) to 7.2 (d) show surface images of mesoporous thin films fabricated directly on silicon wafers using similar precursor solutions as those used for the pastes, incorporating diblock-copolymer of three different molecular weights. From these images it is apparent that the scale of the porosity and specific surface area are directly influenced by the molecular weight of the structure directing polymer. The pore size increases from 20 nm to 70 nm with increasing the polymer molecular weight and the surface areas measured by BET adsorption under N_2 at 77 K, decrease from 77 m^2/g to

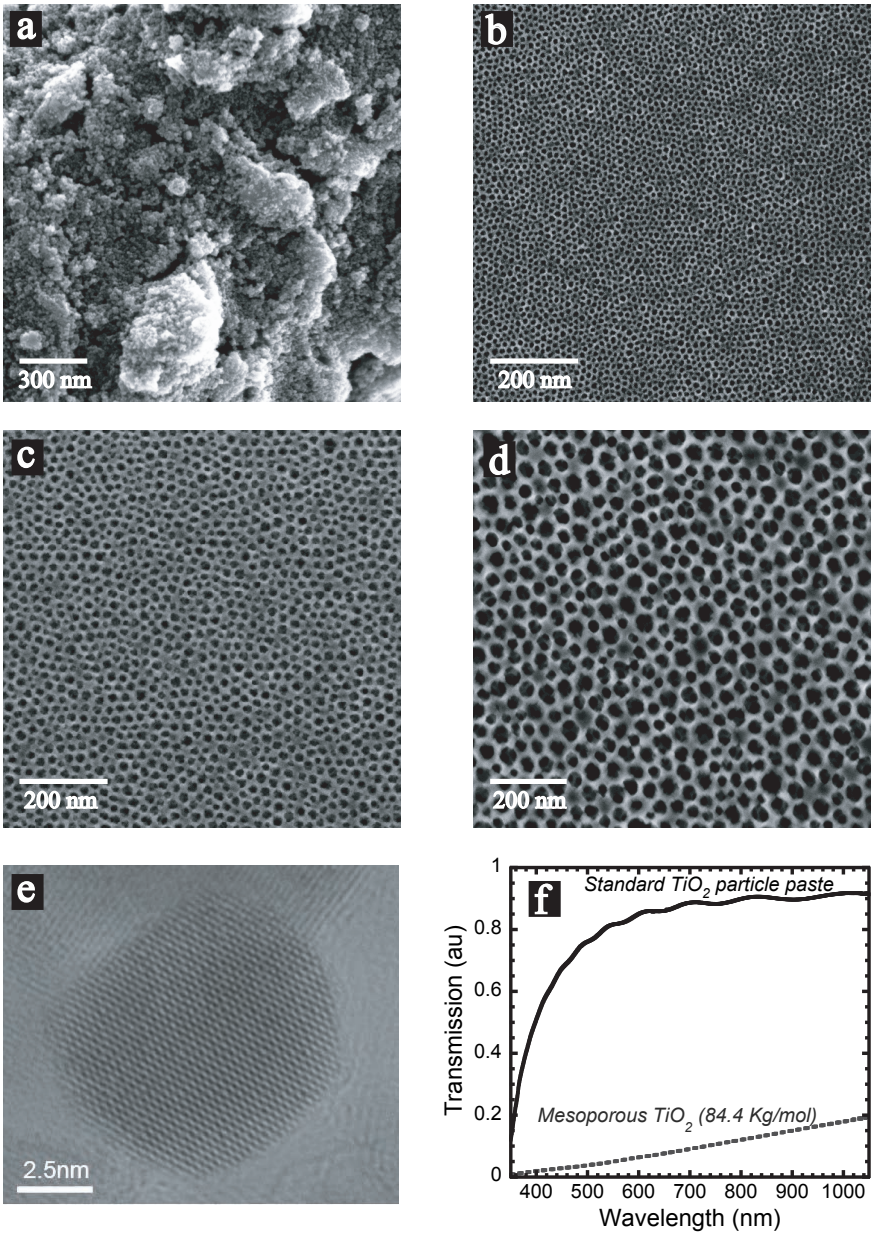

Figure 7.2: SEM and HRTEM images of mesoporous TiO_2 films. ***a)*** *SEM image of a rough film made with a paste,* ***b)*** *SEM image of a mesoporous TiO_2 film made with PI-b-PEO of $M_w = 15\,5$ kg/mol,* ***c)*** *SEM image of a mesoporous TiO_2 film made with PI-b-PEO of $M_w = 33\,5$ kg/mol,* ***d)*** *SEM image of a mesoporous TiO_2 film made with PI-b-PEO of $M_w = 84\,4$ kg/mol,* ***e)*** *HRTEM scan of the $< 100 >$ face of a particle showing the hexagonally packing of the pores,* ***f)*** *Spectral transmission of light for films made with a standard TiO_2 particle paste and with our mesoporous TiO_2 paste.*

45 m^2/g. This compares to a 20 nm pores size [7] for a conventional film fabricated from sol-gel processed sintered nanoparticles. HRTEM study shows that the titania within the particle is crystalline and the faces are oriented along the (111), (101), (131) and (100) directions. An image of the (100) face, in Figure 7.2 (e), shows that the morphology of TiO_2 is hexagonally packed confirming the morphology of the spin-coated films described in the previous chapter.

Light scattering plays an important role in enhancing the efficiency of solar cells by increasing the effective optical path-length in the active medium. This is especially significant for enhancing light absorption near the band edge where the extinction coefficient is low [1]. This is particularly effective for TiO_2 based solar cells since the high refractive index of TiO_2 results in the optical confinement of the scattered light within the TiO_2 layer. For record efficiency dye-sensitized solar cells, large titania particles of around 200-400 nm in diameter are added to the normal particles (20 nm), either mixed together or as a double layer [14]. This is clearly advantageous, but the large particles have a low surface area and exhibit a poor dye uptake, hence the films have to be thick, which sacrifices open-circuit voltage and fill factor [2, 8, 19]. In Figure 7.2 (f) the spectral transmission of the light through films fabricated from a standard particle paste (1.5 μm thick) and our mesoporous TiO_2 paste (1.5 μm thick) are compared. In this instance the roughness of our material is greatly advantageous, inducing sufficient scattering in very thin highly porous films. To compare the influence of pore size and porosity on DSC performance we fabricated solar cells incorporating mesoporous TiO_2 particles made from the three different molecular weight PI-*b*-PEO polymers.

In Figure 7.3 (a), the photovoltaic action spectra are shown. The highest external quantum efficiency peak of around 80 % was obtained for titania structured with the $M_w = 33\ 5$ kg/mol PI-*b*-PEO. The lowest performance of around 57 % was observed for the titania structured with the 15.5 kg/mol polymer. The smaller pore size of the $M_w = 15\ 5$ kg/mol structured titania may simply result in some of the smallest pores not being contacted by the electrolyte.

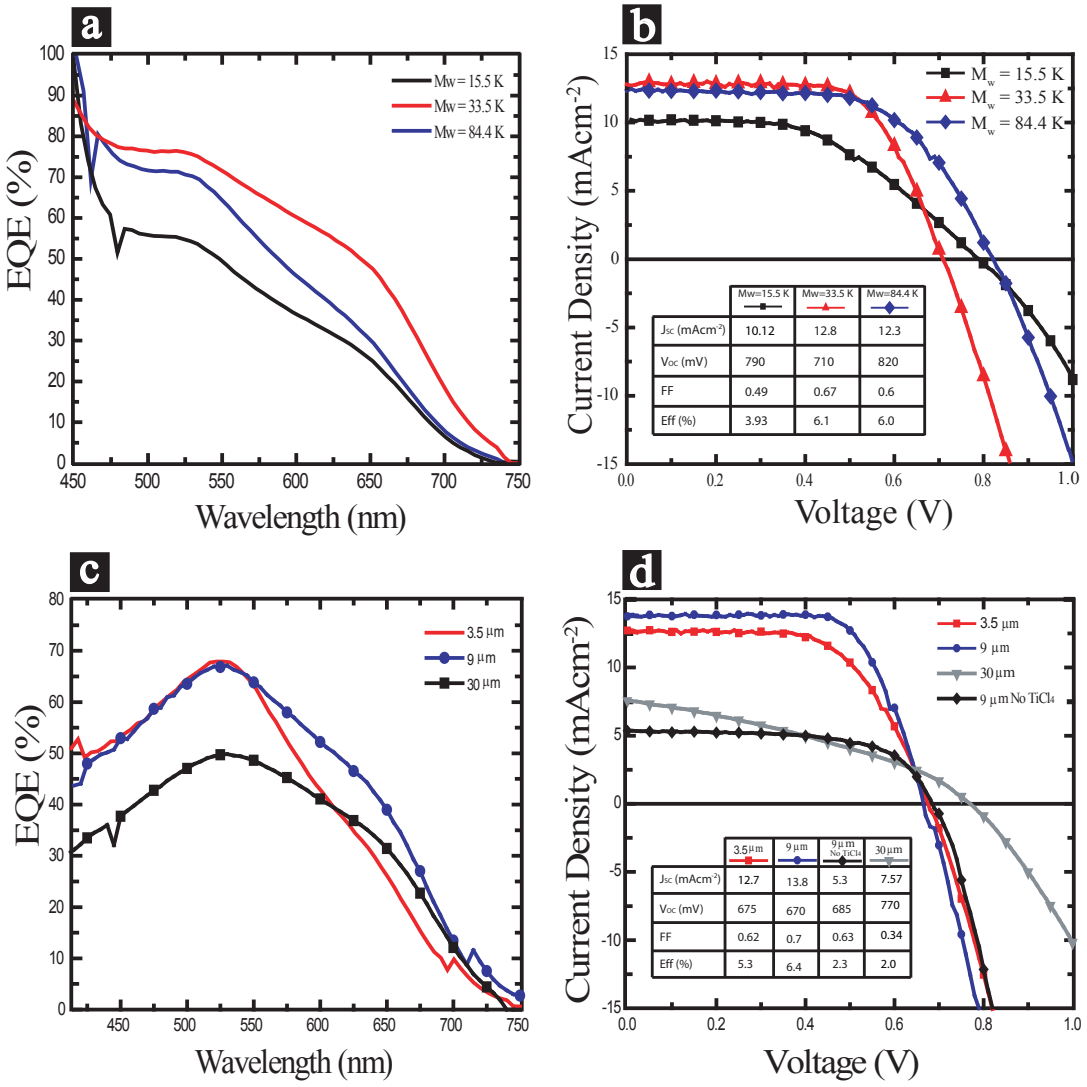

Figure 7.3: Liquid electrolyte dye sensitized solar cell performance. ***a)*** *EQE and,* ***b)*** *current-voltage characteristics for devices made with different molecular weights of the PI-b-PEO copolymer,* ***c)*** *EQE and* ***d)*** *current-voltage characteristics for the devices fabricated with different TiO_2 film thicknesses, with PI-b-PEO of $M_w = 33\ 5$ kg/mol.*

The larger pore size of the 84.4 kg/mol structured titania may be too large resulting in a sacrifice in surface area. We can also not rule out the possibility of inclusions in these films where a spherical void, entirely encapsulated in TiO_2, is isolated from the dye and electrolyte. The occurrence of these inclu-

sions is likely to be strongly influenced by the structure directing agent. We note that previously reported dye-sensitize solar cells by Zukalova *et al.* incorporating the commercially available Pluronic123 triblock copolymer as the structure directing agent, had a pore size of 7 nm in diameter [26]. Figure 7.3 (b) shows current-voltage characteristics of a 9 μm thick solar cell fabricated with the three molecular weights of the diblock-copolymer measured under air mass (AM) 1.5 simulated solar illumination of 100 mWcm^{-2}. Following the same trend as the spectral response, the device which was fabricated from titania structured with the 33.5 kg/mol PI-*b*-PEO delivered the highest current and efficiency. This device exhibited a staggering power conversion efficiency of 6.1 %. The devices made with a higher molecular weight of the diblock-copolymer also performed very well, exhibiting a power conversion efficiency of 6.0 %.

From our materials, the best performing solar cells were made using the 33.5 kg/mol PI-*b*-PEO. Figure 7.3 (c) and 7.3 (d) show the performance of solar cells incorporating titania made from this polymer for a range of TiO_2 film thicknesses varying from 3.5 μm up to 30 μm. From a mechanical viewpoint, fabricating robust, mesoporous, up to 17 μm thick films from normal particles has recently represented a breakthrough in titania paste fabrication [2]. Here, our films remain robust and crack free even for film thicknesses above 30 μm which is the record for mesoporous films structured from block copolymers. Our method entirely overcomes the issue of volume reduction, stress, and cracking. The EQE peaks are around 70 % at 525 nm for the 3.5 μm and 9 μm thick TiO_2 films. However, the action spectrum of the 9 μm thick film is broader due to a higher degree of light scattering and more light is absorbed by the dye at wavelengths $>$ 650 nm. For a 30 μm thick film, the EQE peak is lower, around 50 %. We note that the illumination intensity of our spectral response measuring unit is extremely low (1 mWcm^{-2}) and the illumination spot is much smaller than the active area of the device (1 mm^2 ca 0.31 cm^2 for the device). For these DSCs this does not enable optimum operation and the photovoltaic action spectrum does not deliver

as much current as expected from the measurements under simulated sun light.

In Figure 7.3 (d) we show the current-voltage characteristics for the solar cells prepared with different layer thickness of the TiO_2 electrodes measured under AM 1.5 simulated sun light. The 9 μm thick film gave a power conversion efficiency of 6.4 %, while the thickest cell of 30 μm exhibited a moderate current but a poor fill factor with an over all efficiency of only 2 %. This may be due to the electron diffusion length being shorter than 30 μm thereby limiting current collection. We note that standard liquid-electrolyte solar cells work efficiently up to a layer thickness of approximately 20 μm [18]. The most striking result of our study concerns the thinnest 3.5 μm thick films. The short-circuit current of nearly 13 mA/cm^{-2} and a power conversion efficiency of 5.4 % is unprecedented for films of this thickness incorporating a standard Ru complex dye.

In Figure 7.4 (a) a side view of a 3.5 μm thick film is presented. The large scattering particules are clearly apparent. Considering the roughness and macroscopic disorder in the film it is surprising that it works at all. In Figure 7.4 (b) we present our record efficiency device for the 3.5 μm thick titania layer. This device exhibits a power conversion efficiency of 6.44 % under full sun conditions, the main difference to the previous device being a slightly improved open-circuit voltage and fill factor. Under low light levels of 21 $mWcm^{-2}$ we observe an even more impressive power conversion efficiency of 8.1 %. The photocurrent increases linearly with intensity over this range, but the fill factor increases considerably when the intensity is reduced. We note that these devices are fabricated with a non-volatile electrolyte (Robust) and a standard ruthenium complex dye (N719). These results for thin films represent a significant improvement upon the state-of-the-art.

For all the devices investigated above, the mesoporous titania films were treated with an aqueous $TiCl_4$ solution and subsequently resintered prior to dye adsorption, following standard protocol for DSC fabrication [7]. During this procedure, small (2 nm) nanoparticles are grown on the surface of the TiO_2 resulting

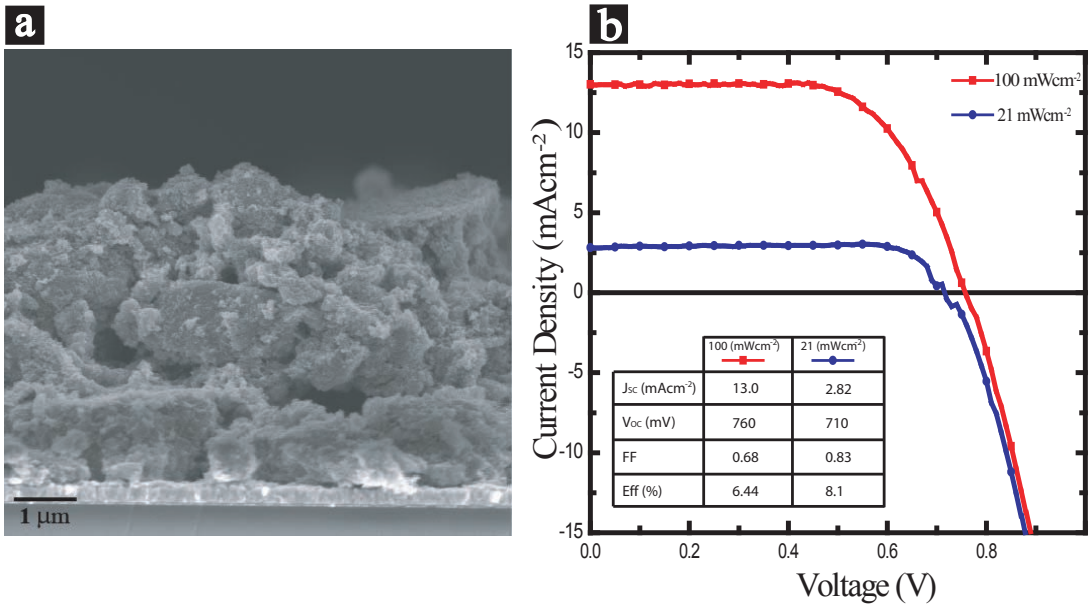

Figure 7.4: ***a)*** *Cross-sectional image of a 3.5 μm thick TiO_2 film,* ***b)*** *current-voltage characteristics for a DSC incorporating a 3.5 μm thick TiO_2 film, PI-b-PEO of $M_w = 33\ 5$ kg/mol, measured under simulated AM 1.5 full sun light (100 $mWcm^{-2}$) and low light intensity (21 $mWcm^{-2}$).*

in enhanced roughness, possible reduction in necking between particles, thereby enhancing charge transport. The $TiCl_4$ treatment most probably also alters the chemical nature of the titania surface. Also shown in Figure 7.3 (d) are the current-voltage characteristics of a 9 μm thick mesoporous TiO_2 film (33.5 kg/mol PI-*b*-PEO) which was not treated with the $TiCl_4$ solution. For this titania, the $TiCl_4$ treatment is clearly critical in order to achieve a high photocurrent and a high power conversion efficiency. The short-circuit photocurrent for the untreated device was only 5.3 $mAcm^{-2}$ (ca. 13.8 $mAcm^{-2}$ for the $TiCl_4$ treated film) with an ensuing power conversion efficiency of only 2.3 %. Interestingly, the fill factor is still above 0.6 suggesting that transport and resistive losses are not too high.

To probe these differences further, we have performed transient open-circuit voltage and transient short-circuit photocurrent measurements similarly to the one previously described [17]. Here, a single red light emitting diode (630 nm peak) was used as the background and perturbation source, focused to give a

maximum intensity of around 100 $mWcm^{-2}$. The perturbation was kept to a minimum intensity such that it could be considered small. At open-circuit, when the light pulse hits the device a transient pulse in the voltage is observed. The factor which causes this increase in voltage is the increase in charge density within the active layer. Since the perturbation is small, the transient decay of the voltage is directly proportional to the transient decay of the charge density, and hence an estimate of the electron-hole recombination lifetime is made. At short-circuit, charge can be collected from the device, and following the light pulse there is a transient pulse observed in the short-circuit current. The current collection rate is then estimated from the decay of this signal. Due to the use of a red light source, the adsorption can be considered uniform over the entire film, and in essence this experiment corresponds to a spatially integrated time of flight transient current measurement under zero (low) field. The effective diffusion coefficient for electrons (D_e) can be calculated following $D_e = w^2\ 2\ 35\tau_{trans}$, where w is the film thickness and τ_{trans} is the current collection lifetime.

The electron transport lifetime and electron recombination lifetime versus background red light intensity for the solar cells with and without the $TiCl_4$ treatment are shown in Figure 7.5 (a). Surprisingly, and conversely to what is usually observed for standard TiO_2, the charge recombination for the device treated with the $TiCl_4$ solution is one order of magnitude faster than that from the non-treated device at low light intensities. However, in both cases the charge recombination lifetime decreases with increasing light intensity and becomes comparable for the two systems at high light intensities. The current collection lifetime for the two systems is comparable for all light intensities and shorter than the charge recombination lifetime. In Figure 7.5 (b) we show the effective diffusion coefficient for electrons calculated from the photo current decay measurements. Here, we observe almost identical diffusion coefficients for devices with or without the $TiCl_4$ treatment, and a relative invariance to light intensity, i.e. a low charge density dependence to the charge transport in this material. We initially expected that prior

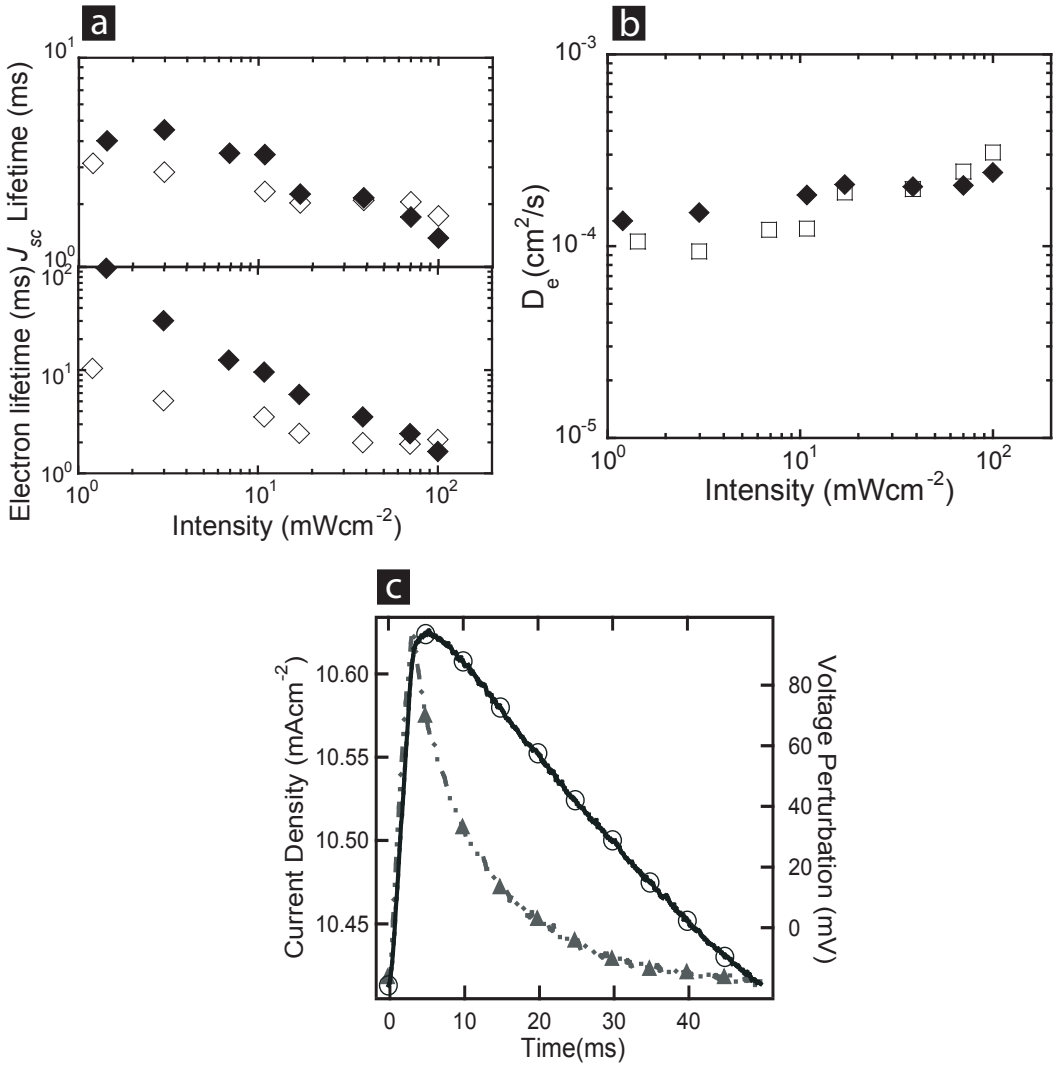

Figure 7.5: ***a)*** *The current decay lifetime and charge recombination lifetime (τ_e measured in a DSC incorporating a 9 μm thick film (33.5 kg/mol PI-b-PEO) at open-circuit (♦ - un-treated film and ◊ - film post-treated with $TiCl_4$ solution.)* ***b)*** *the effective diffusion coefficient as a function of the light intensity (♦ - un-treated film and □ - film treated with $TiCl_4$ solution),* ***c)*** *Transient signal of the current and voltage perturbation under short-circuit conditions under approximately 100 $mWcm^{-2}$ red light intensity.*

to $TiCl_4$ treatment the mesoporous particulates would be insufficiently connected, resulting in poor electron transport. This is apparently not the case, and even in the untreated film the electron diffusion coefficient is over 10^{-4} cm^2s^{-1}. This

is comparable or greater than what is usually reported for films fabricated from standard titania particles especially at low light levels, [20, 25] which is consistent with an excellent connectivity both within the nanocrystaline titania phase and between the macroscopic particulates.

Close examination of Figure 7.5 (a) reveals that, at high light intensities the charge recombination lifetime appears to approach the current collection lifetime. From a naive viewpoint one may wonder how the solar cell can operate efficiently since one may expect the charges to recombine within the cell before being collected. However, here the transport and recombination are measured in very different regimes, one being in the low charge density regime at short-circuit and the other being in the high charge density regime at open-circuit.

In order to obtain good understanding of the transport and recombination in the same regime, it is possible to measure the voltage perturbation under short-circuit conditions. Here, a sourcemeter (or a galvinostat) is used to allow a constant current, equivalent to short-circuit current, to flow through the circuit. Following the light pulse the current cannot vary, therefore a voltage perturbation occurs. Since no extra charge can be collected, the charge injected from the pulse must recombine within the device and the decay of the voltage perturbation is proportional to the decay of the extra charge in the system, hence the charge lifetime is extracted. In Figure 7.5 (c) we show the current and voltage transient responses at short-circuit measured sequentially for the same DSC as the one above, with $TiCl_4$ treatment. Here, we see that the voltage decay is significantly slower than the current decay. It is possible to estimate the electron diffusion length (L_D) from the simple relationship between the electron lifetime and diffusion coefficient, $L_D = \sqrt{D_e \tau_e}$. From the data in Figure 7.5 (c), it is estimated to be 18 μm, in very good agreement with our solar cell thickness dependence measurement thereby confirming our suspicion that the current collection in the 30μm thick solar cell is limited by electron hole recombination.

To compare the efficiency of our material to the standard nanoparticles, four

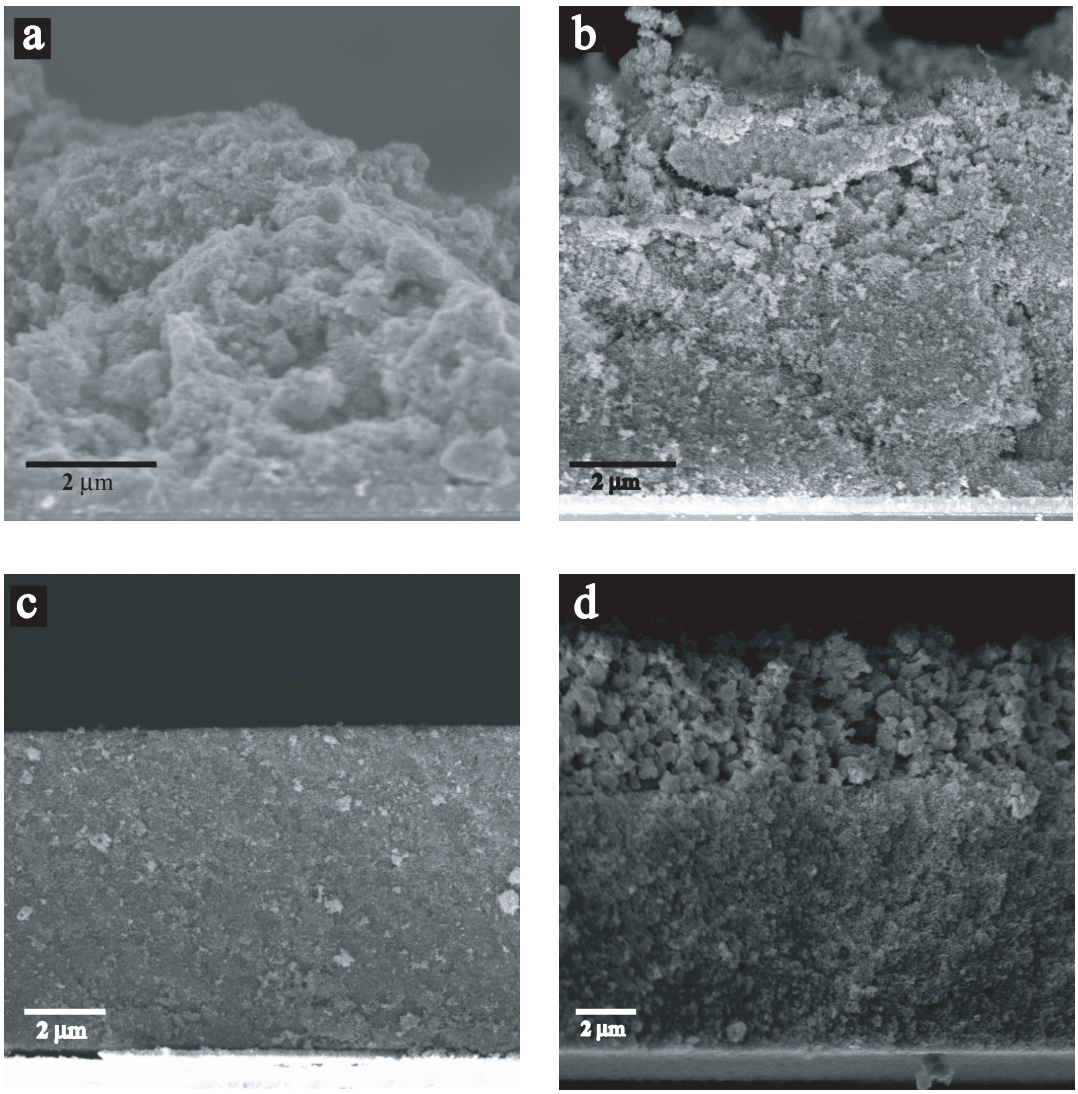

Figure 7.6: SEM images of the cross-sections of TiO_2 layers made from different materials. ***a)*** *4.0 µm thick film made from our paste,* ***b)*** *8.5 µm thick transparent film made from TiO_2 nanoparticles plus a layer of our paste on top* ***c)*** *7.8 µm thick transparent film made from 20 nm TiO_2 nanoparticles,* ***d)*** *8.5 µm TiO_2 layer prepared from a transparent nanoparticle layer and a scattering layer with a particle size of 400 nm.*

different solar cell devices were prepared and the DSCs characteristics measured.

Figure 7.6 shows the cross-section images of TiO_2 films made from mesoporous TiO_2 paste (Figure 7.6 (a)) and from a transparent layer with the mesoporous

TiO_2 paste on top in Figure 7.6 (b). The TiO_2 paste was used as a scattering layer. A single transparent layer (20 nm TiO_2 nanoparticles) and a transparent layer covered by a scattering layer (400 nm TiO_2 nanoparticles) are shown in Figure 7.6 (c) and (d) respectively.

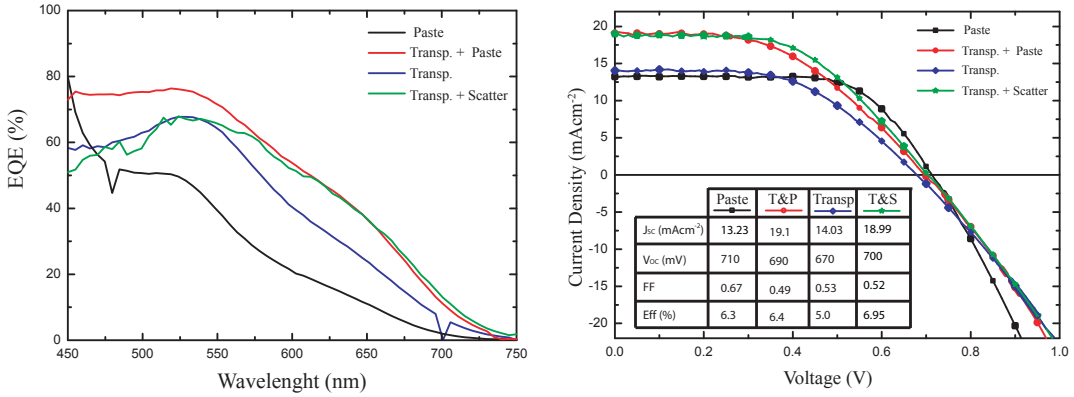

Figure 7.7: Liquid electrolyte dye sensitized solar cell performance. ***a)*** *EQE and,* ***b)*** *current-voltage characteristics for devices made with different TiO_2 materials.*

The solar cell performance of the devices fabricated with the films shown in Figure 7.6 is described in Figure 7.7. The spectral response is shown in Figure 7.6 (a). The highest peak of 78 % was obtained for the DSCs fabricated with the TiO_2 film composed from a transparent layer with a mesoporous TiO_2 film on top. The film prepared with a transparent layer plus a scattering layer on top exhibited a peak of 65 %. Even though the EQE value was lower, this double layer scattered as much light as the one with the highest EQE peak.

A lower EQE peak of 50 % was obtained for the device made from a mesoporous TiO_2 single layer, while the DSC built from the transparent TiO_2 film yielded an EQE of 63 %.

The current-voltage characteristics are shown in Figure 7.7 (b). The devices fabricated with the films from Figure 7.6 (b) and (d) exhibited similar current densities at short circuit, 19.1 $mAcm^{-2}$ and 18.95 $mAcm^{-2}$, respectively. Even though the current densities had similar values, the power conversion efficiency

is higher for the conventional nanoparticle - scattering nanoparticle double layer, around 6.95 %, compared to 6.4 % for the device in which the scattering layer was replaced by a mesoporous particle layer. This is due to a lower fill factor, which might be caused by the mismatched TiO_2 materials. The DSCs fabricated with the film from Figure 7.6 (c) gave a power conversion efficiency of 5 %, while the one from Figure 7.6 (a) had an efficiency of 6.3 %.

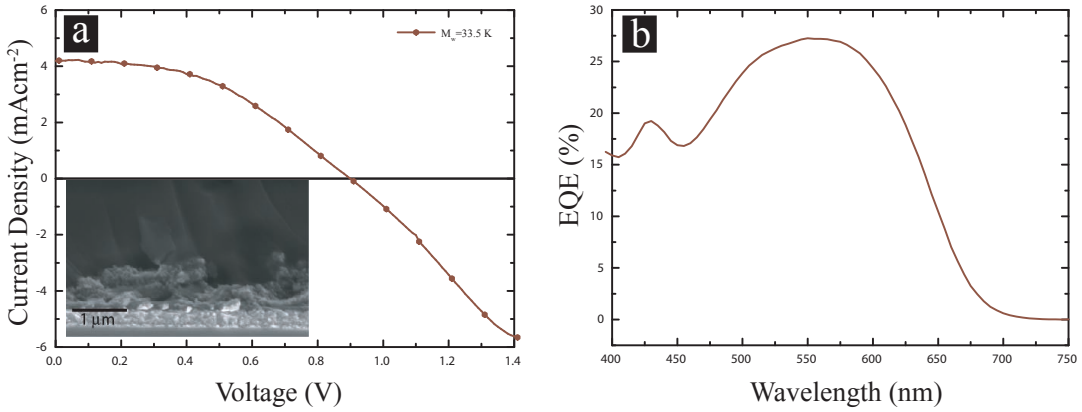

Figure 7.8: Current-voltage characteristic and, ***b)*** *EQE of a solid-state dye sensitized solar cell prepared with a mesoporous TiO_2 paste.*

Figure 7.8 shows the solid-state DSCs characteristics of a device fabricated from the mesoporous TiO_2 paste made with $M_w = 33\,5$ kg/mol PI-*b*-PEO. The TiO_2 film was prepared by the doctor blading technique, and the cell was assembled as described in Chapter 3.9.1. In Chapter 6 the solid state devices were fabricated using the Z-907 dye. For this device, an organic indoline dye named D149, which has a higher extinction coefficient was used. For a 1 μm thick film, the $J_{SC} = 4\,2$ mAcm^{-2}, $V_{OC} = 0\,9$ V, and $FF = 0\,45$ were measured, yielding to a power conversion efficiency of 1.7 % under simulated full sun light. The lower power conversion efficiency given by this cell might be due to the roughness of the TiO_2 film. A cross-section of the device is shown in the inset in Figure 7.8 (a). The film is not homogeneous due to the griding procedure of the TiO_2 powder. In order to obtain smaller and more monodispers particles, a grinding machine

has to be used. If we compare the efficiency of this device with the best efficiency of the solid state DSC described in the Chapter 6, this device performed better. The film thickness was similar and the better efficiency might be due to the dye which absorbed more light. The photovoltaic action spectrum of the 1 μm thick TiO_2 device showed a EQE peak of 23 %.

7.4 Conclusion

In summary, we have developed a novel protocol for fabricating up to 30 μm thick mesoporous TiO_2 films, based on sol-gel chemistry incorporating structure - directing diblock copolymers. Our procedure separates the process of mesopore formation and crystallization from thin film fabrication, rendering it highly suitable for large area coating technologies and up-scaling. These films are highly porous and exhibit substantial light scattering, making them ideally suited for incorporation into the active layer of dye-sensitized solar cells. A solar to electrical power conversion efficiency of over 6.4 % was obtained for DSCs incorporating 3.5 μm thick films measured under full sun conditions (AM 1.5 (100 mWcm^{-2})). Under lower light levels of 21 mWcm^{-2} this efficiency increases to over 8 %. Using an organic dye, the efficiency of a solid-state dye sensitized cells was improved to 1.7 %. This work demonstrates that soft templates can yield a much greater control over mesopore formation than conventional material fabrication techniques, resulting in advantageous optical and electronic functionalities. This procedure is applicable to a large number of mesoporous materials which can be fabricated employing structure-directing-agents, [9, 23] with broad ranging applications.

Bibliography

[1] C. J. Barbe, F. Arendse, P. Comte, M. Jirousek, F. Lenzmann, V. Shklover, and M. Graetzel. Nanocrystalline titanium oxide electrodes for photovoltaic applications. *J. Am. Ceram. Soc*, 80:3157 3171, 1997.

[2] S. Itoand P. Chen, P. Comte, M. K. Nazeeruddin, P. Liska, P. Pechy, and M. Graetzel. Fabrication of screen-printing pastes from TiO_2 powders for dye-sensitized solar cells. *Progress in Photovoltaics: Research and Applications*, 2007.

[3] E. J. W. Crossland, M. Kamperman, M. Nedelcu, C. Ducatti, U. Wiesner, D.-M. Smilgies, G. E. S. Toombes, M. A. Hillmyer, S. Ludwigs, U. Steiner, and H. J. Snaith. The biocontinuous double gyroid-sensitized solar cell. *Submitted to Nature*.

[4] E. J. W. Crossland, S. Ludwigs, M. A. Hillmyer, and U. Steiner. Freestanding nanowires arrays from soft-etch block copolymer templates. *Soft Matter*, 3:94 98, 2007.

[5] A. C. Finnerfrock, R. Ulrich, G. E. S. Toombes, S. M. Gruner, and U. Wiesner. The plumber s nightmare: *a* new morphology in block copolymer-ceramic nanocomposites and mesoporous aluminosilicates. *J. Am. Chem. Soc.*, 125:13084 13093, 2003.

[6] M. Gratzel. Conversion of sunlight to electric power by nanocrystalline dye-sensitized solar cells. *J. Photochem. and Photobiol. A:Chem.*, 164:3 14, 2003.

[7] S. Ito, P. Liska, P.Comte, R. Charvet, P. Pechy, U.Bach, L. Schmidt-Mende, S. M. Zakeeruddin, A. Kay, M. K. Nazeeruddin, and M. Graetzel. Control of dark current in photoelectrochemical (TiO_2/I-I_3) and dye-sensitized solar cells. *Chem. Commun.*, pages 4351 4353, 2005.

[8] S. Ito, S. M. Zakeeruddin, R. Humphry-Baker, P. Liska, R. Charvet, P. Comte, M. Mohammad, K. Nazeeruddin, P. Pechy, M. Takata, H. Miura, S. Uchida, and M. Gratzel. High-efficiency organic-dye-sensitized solar cells controlled by nanocrystalline-TiO_2 electrode thickness. *Adv. Mater.*, 18:1202 1205, 2006.

[9] M. Kamperman, C. B. W. Garcia, P.Du, H. Ow, and U. Wiesner. Ordered mesoporous ceramics stable up to 1500 degrees *c* from diblock copolymer mesophases. *J. Am. Chem. Soc.*, 126:14708 14709, 2004.

[10] J. Lee, M. C. Orilall, S. C. Warren, M. Kamperman, F. J. DiSalvo, and U. Wiesner. Direct access to thermally stable and highly crystalline mesoporous transition-metal oxides with uniform pores. *Nat. Mater.*, doi:10.1038/nmat2111, 2008.

[11] M. K. Nazeeruddin, P. Pechy, T. Renouard, S. M. Nazeeruddin, R. Humphry-Baker, P. Comte, P. Liska, L. Cevey, E. Costa, V. Shklover, L. Spiccia, G. B. Deacon, C. A. Bignozzi, and M. Gratzel. Engineering of efficient panchromatic sensitizers for nanocrystalline TiO_2-based solar cells. *J. Am. Chem. Soc.*, 123:1613 1624, 2001.

[12] M. Nedelcu, J. Lee, E. J. W. Crossland, M. C. Orilall, S. C. Warren, U. Wiesner, U. Steiner, and H. J. Snaith. Block-copolymer directed synthesis mesoporous TiO_2 and its application in solid state dye sensitized solar cells. *In preparation.*

[13] B. O Regan and M. Gratzel. A low-cost, high efficiency solar based in dye-sensitized solloidal TiO_2 films. *Nature*, 353:737 739, 1991.

[14] G. Rothenberger, P. Comte, and M. Gratzel. A contribution to the optical design of dye-sensitized nanocrystalline solar cells. *Solar En. Mater. Solar Cells*, 58:321 336, 1999.

[15] C. H. Seaman. Calibration of solar cells by the reference cell methode-the spectral mismatch problem. *Solar Energy*, 29:291 298, 1982.

[16] P. F. W. Simon, R. Ulrich, H. W. Spiess, and U. Wiesner. Block copolymer-ceramic hybrid materials from organically modified ceramic precursors. *Chem. Mater.*, 2001:3464 3486, 13.

[17] H. J. Snaith and M. Gratzel. Electron and hole transport through mesoporous TiO_2 infiltrated with Spiro-MeOTAD. *Adv.Mater.*, 19:3643 3647, 2007.

[18] H. J. Snaith and L. Schmidt-Mende. Advances in liquid-electrolyte and solid-state dye-senstized solar cells. *Adv. Mater.*, 19:3187 3200, 2007.

[19] H. J. Snaith, L. Schmidt-Mende, M. Chiesa, and M. Gratzel. Light intensity, temperature, and thickness dependence of the open-circuit voltage in solid-state dye-sensitized solar cells. *Phys. Rev. B.*, 74:045306, 2006.

[20] A. Solbrand, H. Lindstroem, H. Rensmo, A. Hagfeldt, S.-E. Lindguist, and S. Soedergren. Electron transport in the nanostructured TiO_2-electrolyte system studied with time-resolved photocurrents. *J. Phys. Chem. B.*, 101:2514 2518, 1997.

[21] M. Templin, A. Franck, A. D. Chesne, H. Leist, Y. Zhang, R. Ulrich, V. Schadler, and U. Wiesner. Organically modified aluminosilicate mesostructures from block copolymer phases. *Science*, 278:1795 1798, 1997.

[22] T. Thurn-Albert, J. Schotter, G. A.Kastle, N. Emly, T. Shibauchi, L. Krusin-Elbaum, K. Guarini, C. T. Black, M. T. Tuominen, and T. P. Russell. Ultralight-density nanowires arrays grown in self-assembled diblock copolymer templates. *Science*, 290:2126 2129, 2000.

[23] S. C. Warren, F. J. DiSalvo, and U. Wiesner. Nanoparticles-tuned assembly and disassembly of mesostructured silica hybrids. *Nat. Mater.*, 6:156 161, 2007.

[24] P. Yang, D. Zhao, D. I. Margolese, B. F. Chmelka, and G. D. Stucky. Generalized syntheses of large-pore mesoporous metal oxides with semicrystalline frameworks. *Nature*, 396:152 155, 1998.

[25] K. Zhu, N. Kopidakis, N. R. Neale, J. van de Lagemaat, and A. J. Frank. Influence of surface area on charge transport and recombination in dye-sensitized TiO_2. *J. Phys. Chem. B.*, 110:25174 25180, 2006.

[26] M. Zukalova, A. Zukal, L. Kavan, M. K. Nazeeruddin, P. Liska, and M. Gratzel. Organized mesoporous TiO_2 films exhibiting greatly enhanced performance in dye-sensitized solar cells. *Nano Lett.*, 5:1789 1792, 2005.

CHAPTER 8

Mesoporous Nb_2O_5 and its Application in Solar Cells

8.1 Introduction

Since the discovery of dye sensitized solar cells (DSC) by O Regan and Gratzel in 1991 considerable research has focussed on the development of highly efficient and durable photovoltaic devices. This requires the improvement of the semiconductor TiO_2 material, of the dye and of the hole transporter which can be a liquid electrolyte or a solid organic material. One route of optimization is therefore the development of new n-type semiconductor materials as an alternative to the commonly used TiO_2. Possible alternatives that can be used in DSCs are CdSe, ZnO, WO_3, Nb_2O_5, SnO_2 [2] etc.

Nb_2O_5 is an interesting semiconductor candidate with a band gap between 3.2 - 4 eV, which has also potential applications in Lithium batteries [3, 6], display devices [1], or dye sensitized solar cells [5]. Several preparation methods of Nb_2O_5 have been described in the literature, such as the deposition of a colloidal suspension [5] or a sol-gel approach [7]. Yang *et al.* used a poly(alkylene oxide) block-copolymer dissolved in ethanol, mixed with $NbCl_5$. In order to obtain mesoporous Nb_2O_5, the material was pyrolyzed at a high temperature. Orilall *et al.* showed that highly crystalline and well organized mesoporous Nb_2O_5 can be obtained in a simple one-pot procedure [4]. They used a PI-*b*-PEO block copolymer mixed with niobium ethoxide and niobium chloride. These inorganic materials swell only the hydrophilic block (PEO) of the block copolymer, leading to PI columns in a matrix of PEO with inorganic materials. The ratio between the polymer and the niobium oxide precursor was 1:1.45.

Following Orilall s recipe we have worked towards the application of the mesoporous Nb_2O_5 for use in DSCs. This project is in progress and only preliminary results are presented in this chapter.

8.2 Experimental Details

PI-*b*-PEO block copolymer with $M_w = 15\ 5$ kg/mol, 22.7 wt% PEO was dissolved in 1.5 ml THF and mixed with 0.15 ml of niobium ethoxide. The solution was stirred for about 30 minutes. 0.1 g of $NbCL_5$ was added and the solution was stirred for more than 2 hours in a glove box, ($NbCl_5$ is air sensitive).

To obtain thin films, the solution was spin-coated with 3000 rpm for 1 min. onto FTO glass covered with a compact TiO_2 layer by spray pyrolysis (see Chapter 3.3). The films were placed onto a hot plate at 100 °C for 1 hour to evaporate the solvent, and transferred into a tube furnace for calcination at 550 °C for 2 hours under N_2 using a ramping rate of 1 degree/min. During this process, PI was transformed into carbon acting as a scaffold for the mesoporous structure

preventing its collapse. To remove the carbon, the films were heated at 500 °C under O_2 for 2 hours, with a ramping rate of 1 degree/min. To prepare thicker films by spin-coating, the first layer was spun, and the solvent was evaporated on a hot plate at 100 °C for 1 hour. A second layer was cast onto the first layer followed again by the heating step. The sample was then transferred into the tube furnace for calcination as described earlier. These films were assembled into solid state dye sensitized solar cells as described in Chapter 3.9.1.

To obtain a powder that can be processed into a paste, the mixture was placed into a ceramic boat on a hot plate at 50 °C, for more than 24 hours to slowly evaporate the solvent. The boat was partially covered with a Petri dish to regulate the evaporation rate. To completely remove the remaining solvent and other volatile products, the material was transferred into a vacuum oven at 130 °C for 2 hours, and then into a tube furnace for high temperature processing. To transform the Nb precursor into Nb_2O_5, the powder was heated at 600 °C for 2 hours under N_2 using a ramping rate of 1 degree/min, followed by O_2 at 500 °C to remove the carbon. A paste was made from the powder as described in Chapter 3.7. Films were fabricated by the doctor-blading technique and were assembled into liquid dye sensitized solar cells (see in Chapter 3.9.2).

8.3 Results and Discussion

SEM images of the single and double layers of mesoporous Nb_2O_5 are shown in Figure 8.1. The morphology of the top surface of the single layer is worm-like. The pore size is around 20 nm and the films are bicontinuous down to the substrate. The Figure 8.1 (b) shows the top view of the two layers of mesoporous Nb_2O_5. The surface morphology indicates that the layer is porous. Surprisingly is the morphology of the double layer differs. The surface pores are elongated, having a needle shape morphology. This has also been observed by Lenzmann [5] in his study of Nb_2O_5 nanoparticles. These films were fired at lower temperature (400-

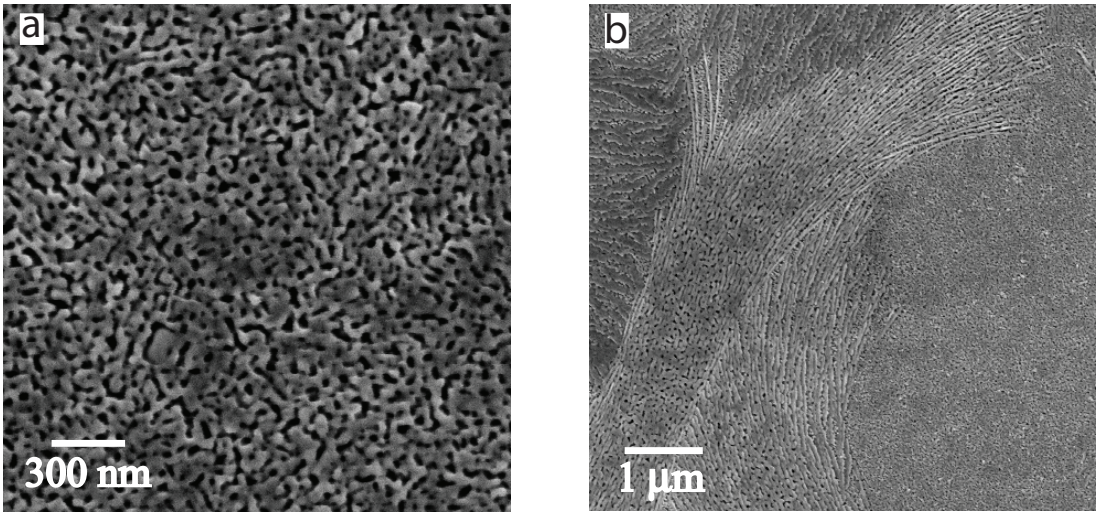

Figure 8.1: SEM images of Nb_2O_5 films. ***a)*** *shows a single layer,* ***b)*** *shows a double layer deposited by spin-coating.*

500 °C) and had a smaller needle size, while the samples fired at a temperature higher than 500 °C showed a 5 times larger needle morphology. In our case we obtained a needle like morphology of the mesoporous Nb_2O_5 only for films that are thicker than 400 nm and spin-coated double or triple layers. This may be due to a preferential alignment of the material when coated onto a surface of the same material.

The -2ν X-ray scans of the film shown in Figure 8.2 demonstrates the purity of the Nb_2O_5 phase. It has been reported that Nb_2O_5 heated at a temperature below 500 °C is in the amorphous phase and starts to crystallize between 500-600 °C. At about 600 °C it is fully crystalline in the orthorhombic phase. Crystallization occurs more rapidly at higher temperatures, up to 900 °C. At temperatures higher than 900 °C the monoclinic form becomes evident [5]. In our case the films were heated at 550 °C, limited by the substrate stability. Previous studies of DSCs based on TiO_2 showed a reduction in power conversion efficiency when heated to temperatures higher than 600 °C, possibly caused by the de-doping of the FTO. The X-ray data displayed in Figure 8.2 shows a Nb_2O_5 film on a silicon wafer heated at 550 °C. The sharp peaks are an indication for the crystalline

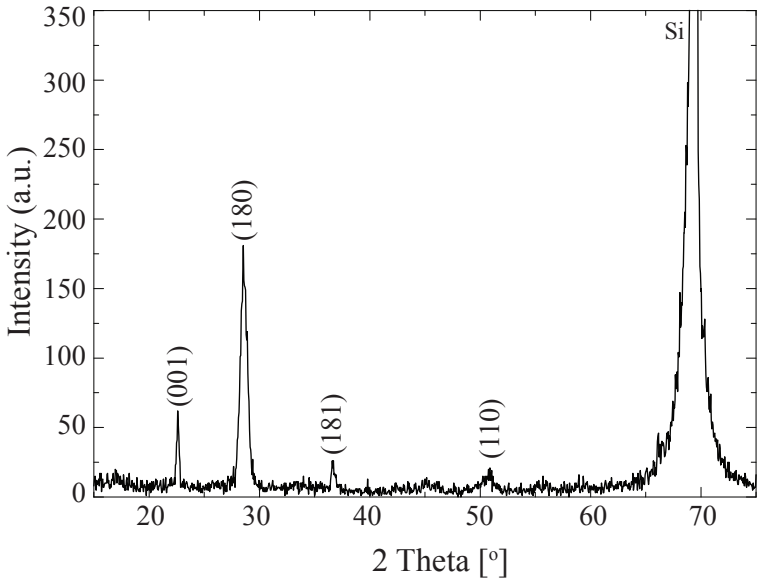

Figure 8.2: X-ray scan of a Nb_2O_5 film deposited on a silicon wafer substrate.

nature of the material. Broad peaks are seen from a mixture of amorphous and crystalline phases. The crystal size calculated with the Debye-Scherrer formula from the highest intensity peak ($2\nu = 28\ 55\ °$) is around 11 nm.

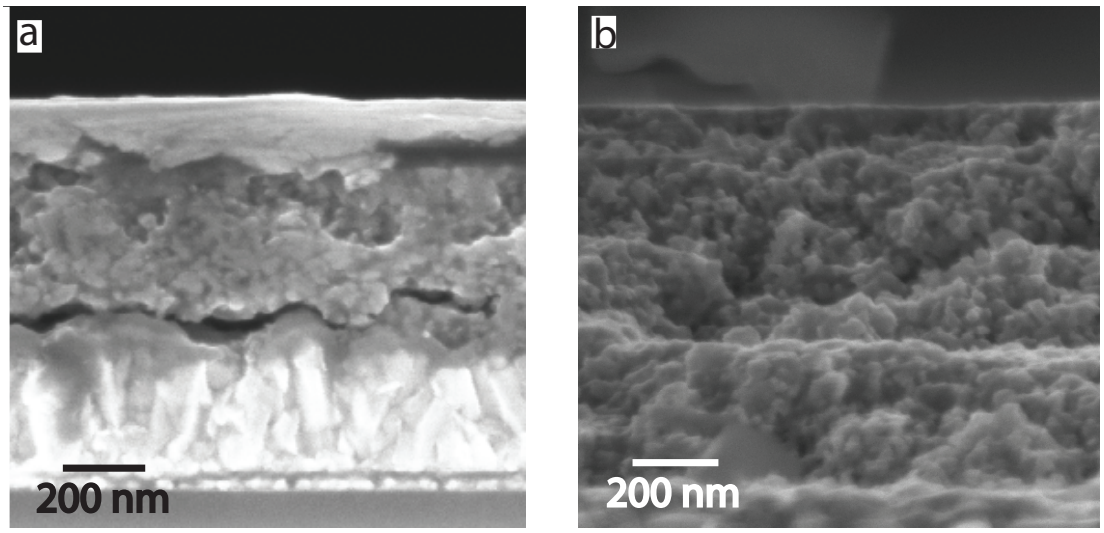

Figure 8.3: SEM cross-sections of fractured Nb_2O_5 films. ***a)*** *390 nm thick Nb_2O_5 solid state DSC,* ***b)*** *600 nm thick Nb_2O_5 solid state DSC showing two individual layers.*

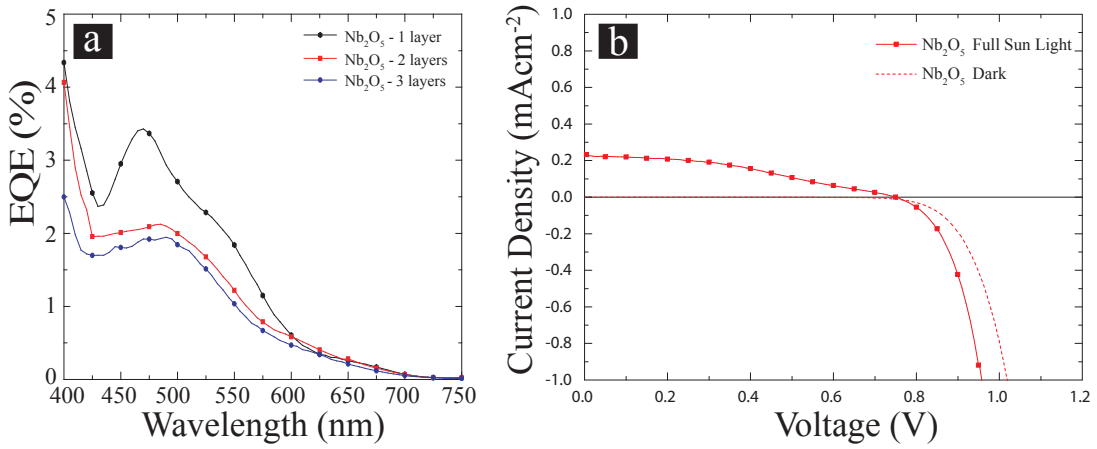

Figure 8.4: Solid state dye sensitized solar cell performance. ***a)*** *EQE of the devices as a function of the Nb_2O_5 film thickness, and* ***b)*** *current-voltage characteristic of the device made with one layer of the Nb_2O_5.*

The films made on FTO glass were used to fabricate solid state DSCs. The devices were assembled as described in Chapter 3.9.1. Before soaking in the dye solution, the films were treated in a mild piranha[i] solution. The organic hole transporter (Spiro-MeOTAD) was spin-coated onto the porous Nb_2O_5 film and Ag was evaporated as top electrode. Figure 8.3 shows the cross-sections of single and double layer devices from mesoporous Nb_2O_5. Figure 8.3 (a) indicates that the Spiro-MeOTAD has filled all the pores down to the substrate, while in Figure 8.3 (b) the hole transporter has not reached the bottom electrode. This might be due to the morphology of the double layer film. Possibly there was no continuity between the layers.

The solar cell performance of these devices is presented in Figure 8.4. The photovoltaic action spectra for different film thicknesses are shown in Figure 8.4 (a). The highest peak EQE of around 3.5 % was obtained for one layer of the Nb_2O_5, 2.2 % was obtained for the double layer of the semiconductor, while the poorest performance was obtained for three layers of the material, of around 2 %.

[i]Mild piranha solution contains 1 part of Millipore water, 3 parts of sulphuric acid and 2 parts of hydrogen peroxide, 30 % heated at 50 °C for 30 min.

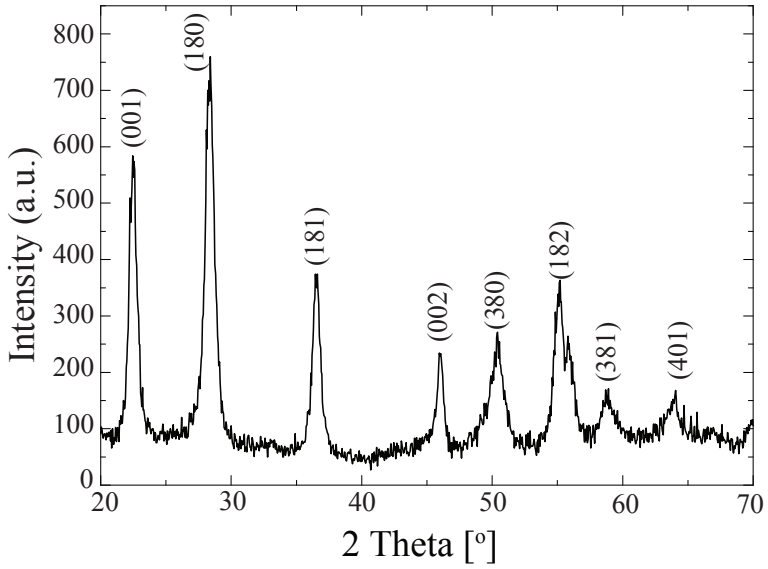

Figure 8.5: X-ray -2ν scan of mesoporous Nb_2O_5 powder.

We think that the lower performance of the two and three layers DSCs is due to the lack continuity between the layers. The hole conductor might therefore only have filled the top layer. Due to the low EQE values, the current-voltage characteristics were measured only for the solar cell made with one layer of the mesoporous Nb_2O_5 shown in Figure 8.4 (b). Under simulated full sun light AM 1.5, 100 mWcm^{-2}, $J_{SC} = 0\,225$ mAcm^{-2}, $V_{OC} = 0\,74$ V and $FF = 0\,37$ % yielding a power conversion efficiency of 0.62 %. The low value of the efficiency may be due to a number of reasons such as: the crystallinity of the material, i.e. at 550 °C a mixture of amorphous and crystalline phases might coexist with the amorphous material acting as possible traps for electrons. The improvement of the crystallinity might play an important role in improving the efficiency of the cells. Another reason might be the blocking layer used in these devices (TiO_2). A compact layer of Nb_2O_5 might improve the cell performance.

To prepare thicker films, a mesoporous Nb_2O_5 powder was made (as described in the Chapter 3), by heating the material at 600 °C under N_2. Figure 8.5 shows

a X-ray diffraction scan of the Nb_2O_5 powder. Heating the material at a higher temperature improved the crystallinity of the material. In this case the crystal size is around 13 nm, slightly higher than the crystal size of the films heated at 550 °C.

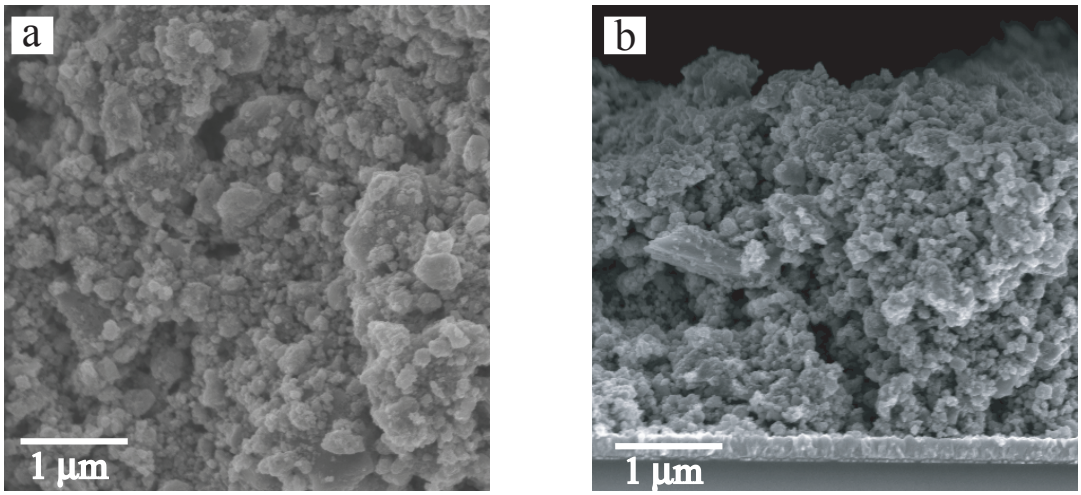

Figure 8.6: SEM images of the mesoporous Nb_2O_5 films made using a paste. ***a)*** *Top view of the film, and* ***b)*** *Cross-section of a rough Nb_2O_5 film.*

A paste was made from the mesoporous Nb_2O_5 powder and blade-coated onto FTO glass substrates. The films were heated at 350 °C for 30 min. to remove the ethyl cellulose and then at 500 °C for 1 hour under O_2 to ensure a good interconnection between the particles. The SEM images of the film morphology and a cross-section of the film made from the paste are shown in Figure 8.6. The films were very rough, showing the variation of particle sizes obtained by grinding the powder. To improve the particle size distribution a more uniform grinding of the powder is required. These films were used to fabricate liquid electrolyte DSC. The film thickness was around 5 μm. In Figure 8.7 the current voltage characteristic of the Nb_2O_5 solar cells is presented. Before dye sensitizing, the samples were treated in a $NbCl_5$ 40 mM solution in ethanol at 75 °C for 15 min., and heated on a hot plate at 500 °C for 1 hour. The dyed films were sandwiched

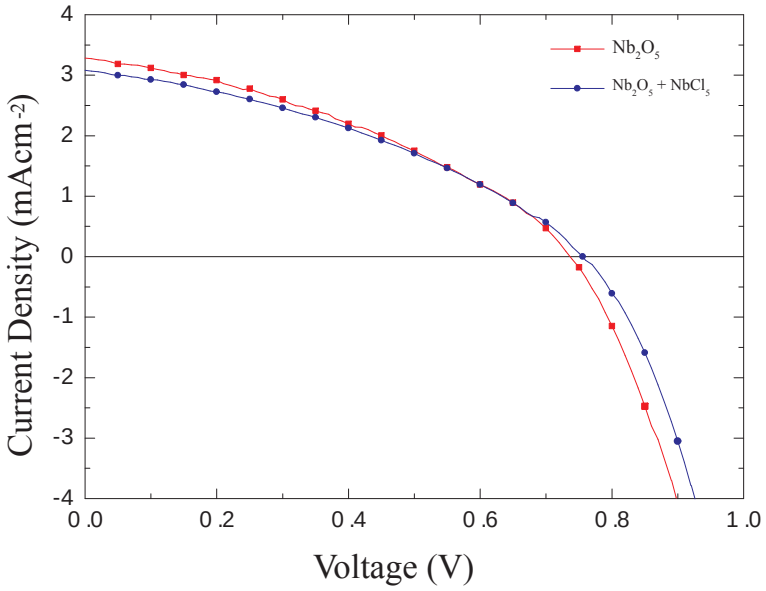

Figure 8.7: Current-voltage characteristics of a Nb_2O_5 liquid electrolyte DSC for devices fabricated from non-treated and $NbCl_5$ treated films of the mesoporous Nb_2O_5.

with a platinized FTO substrate and a Robust liquid electrolyte was injected. The samples were measured under simulated full sun light. The device made with a non-treated film gave $J_{SC} = 3\ 28$ mAcm^{-2}, $V_{OC} = 0\ 73$ V, $FF = 0\ 37$ %, exhibiting a power conversion efficiency of 0.9 %. The $NbCl_5$ treated film gave similar results as the non-treated device, yielding an efficiency of $\eta = 0\ 87$ %. For Nb_2O_5 solar cell devices, the pore-surface treatment did not seem to improve the performance of the device, in difference to TiO_2 based devices.

8.4 Conclusions

In summary we have shown that mesoporous Nb_2O_5 can be used to produce solid state and liquid electrolyte dye sensitized solar cells. However, the performance of these devices is quite low compared to state-of-the-art. The porosity of the semiconductor material plays a crucial role for the dye uptake and filling of the pores with the hole transporter. A variation of the pores size by changing the

molecular weight of the diblock-copolymer is required to optimize the devices. As Nb_2O_5 is fully crystalline only at high temperature. Heating the powder at a temperature higher than 600 °C may improve the power conversion efficiency of the cells.

Bibliography

[1] C. O. Avellanda, A. Pawlicka, and M. A. Aegerter. Two methods of obtaining sol-gel Nb_2O_5 thin films for electrochromic devices. *J. Mater. Sci.*, 33:2181 2185, 1998.

[2] M. Gratzel. Photoelectrochemical cells. *Nature*, 414:338 344, 2001.

[3] N. Kumagai, T. Nakajima, K. Tanno, and N. Watanabe. Structural changes for Nb_2O_5 and V_2O_5 as rechargeable cathods for lithium bateries. *Electrochim. Acta*, 28:17 22, 1983.

[4] J. Lee, M. C. Orilall, S. C. Warren, M. Kamperman, F. J. DiSalvo, and U. Wiesner. Direct access to thermally stable and highly crystalline mesoporous transition-metal oxides with uniform pores. *Nat. Mater.*, doi:10.1038/nmat2111, 2008.

[5] Frank Lenzmann. *Mesoporous, nanoparticulate films of Nb_2O_5 and ZrO_2. Preparation and characterization.* PhD thesis, Ecole Polythechinique Federale de Lausanne, 2000.

[6] B. Reichman and A. J. Bard. The application of Nb_2O_5 as a cathode in nonaqueous lithium cells. *J. Electrochem. Soc.*, 128, 344-346.

[7] P. Yang, D. I. Margolese, B. F. Chmelka, D. Zhao, and G. D. Stucky. Generalized syntheses of large-pore mesoporous oxides with semicrystalline frameworks. *Nature*, 396:152 155, 1998.

CHAPTER 9

Conclusions

In this thesis I have discussed the development of inorganic material systems based on organic precursors, their application in thin films and pastes, and the patterning of these films using soft lithography. The materials studied here might have various technological applications, such as in magnetic data storage or in dye sensitized solar cells.

Ferromagnetic nickel metal was obtained via a spin-coatable nickel naphthenate resist. This resist had a good electron beam sensitivity and contrast, and therefore, with the help of electron-beam lithography, 10 - 14 nm wide lines were written. The transformation of the nickel naphthenate into Ni metal slightly reduced the width of the lines to 7 - 9 nm. Keeping the lines in air, oxidized the Ni and no further measurements could be performed. Unpatterned films showed a good magnetization saturation and a satisfactory electrical resistivity.

The major part of this thesis is focussed on the improvement of the performance of dye sensitized solar cells. The materials that are the key in obtaining efficient solar cells are an electron conducting semiconductor, a dye, and a hole transporter. Our objective was to improve the electron conducting semiconductor material (e.g. TiO_2 and Nb_2O_5). For this, the diblock-copolymer PI-*b*-PEO, used as sacrificial material, was combined with a precursor material, yielding mesoporous materials via self-assembly of the block-copolymer. The block-copolymer consists of a hydrophilic and a hydrophobic block. The metal precursor was chosen in such a way that will swell only the hydrophilic block (PEO in our case). This way a PI phase in a matrix of PEO mixed with the precursor was obtained. To transform this precursor into the required oxide material, the polymer-precursor mixture was heated at different temperatures under an inert atmosphere and oxygen. One of the advantages of this method is the improvement of the semiconductor crystallinity without collapsing of the pores. The morphology and the pore sizes can be also controlled by the molecular weight of the polymer and the amount of added precursor. Here, we were mainly focussed on TiO_2 and Nb_2O_5 semiconductors and their application in DSCs.

The TiO_2 dye sensitized solar cells were fabricated using two techniques. One was a spin-coatable TiO_2 precursor followed by heating. The other approach consists of the manufacture of a mesoporous bulk material followed by the preparation of a paste, which was subsequently used to manufacture the active layers of a DSC. In both approaches, the pore size of 15 nm - 70 nm was controlled by the molecular weight of the polymer (15.5 $kgmol^{-1}$ - 84.4 $kgmol^{-1}$). To further increase the porosity, the amount of precursor was decreased to 25 %, 50 % and 75 % from the original amount. These films were used to fabricate solid state dye sensitized solar cells. We obtained a power conversion efficiency of 1.5 % for a 1.2 μm thick TiO_2 film using an intermediate molecular weight of the PI-PEO and 2:0.5 ratio between the polymer and precursor.

To further increase the film thickness, up to 30 μm, we fabricated a paste from

a mesoporous powder mixed with a binder and solvent. The films were prepared by doctor-blade technique. Liquid and solid state dye sensitized solar cells were prepared from these films. DSCs incorporating a 3.5 μm thick TiO_2 film, measured under simulated full sun light gave a power conversion efficiency of over 6.4 %, while under low light intensity the efficiency increased to over 8 %. These results demonstrate that soft templates exert a better control over mesopore formation than other material fabrication techniques. Another advantage of this material is the enhancement of light scattering, which plays an important role in enhancing the efficiency of solar cells. Light scattering increases the effective optical path-length in the active medium thereby enhancing the light absorbtion near the band edge , where the extinction coefficient of the dye is low. A 1.2 μm thick TiO_2 film fabricated with the paste, incorporated into a solid state DSC gave a power conversion efficiency of 1.7 %.

This procedure is applicable to a large number of mesoporous materials, and to prove this, Nb_2O_5 system was also studied in this thesis. Only some preliminary results are shown, but we demonstrated that Nb_2O_5 can be used to fabricate dye sensitized solar cells. More investigation of this system is necessary.

The performance of dye sensitized solar cells fabricated with this kind of mesoporous material can be further improved. A better control of the particle size by improving the grinding protocol can yield a more homogeneous film, resulting in a better filling of the pores by the hole transporter. This is especially important for solid state DSCs. It has to be determined whether the assumption that a higher crystallinity of the electron conductor improves the solar cell performance is correct. The efficiency can be also improved by using dyes with a higher extinction coefficient. They may pave the way for devices with thinner active layers and a higher power conversion efficiency.

Publications and Conferences

Publications

- *"Pattern formation by temperature-gradient driven film instabilities in laterally confined geometries"* - **M. Nedelcu**, M. D. Morariu, S. Harkema, N. E. Voicu and U. Steiner, **Soft Matter**, 1, 62-65 (2005)

- *"Block-copolymer directed synthesis of mesoporous TiO_2 and its applications in solid state dye-sensitized solar cells"* **M. Nedelcu**, J. Lee, E. J. W. Crossland, M. C. Orilall S. C. Warren, U. Wiesner, U. Steiner and H. J. Snaith, **In preparation**

- *"High efficiency dye-sensitized solar cells employing mesoporous TiO_2 structured from diblock copolymers"* - **M. Nedelcu**, J. Lee, E. J. W. Crossland, C Ducati M. C. Orilall, S. C. Warren, U. Wiesner, U. Steiner and H. J. Snaith, **In preparation**

- *"Soft lithography of hard materials"* - O. Gobel, **M. Nedelcu** and U. Steiner, **Advanced Function Materials**, 17, 1131-1136 (2007)

- *"The biocontinous double gyroid dye-sensitized solar cell"* - E. J. W. Crossland, M. Kamperman, **M. Nedelcu**, C. Ducati, U. Wiesner, D. M. Smilgies, G. E. S. Toombes, M. A. Hillmayer, S. Ludwigs, U. Steiner and H. J. Snaith, **Submitted to Nature**, 2008

- *"Block copolymer morphologies in dye-sensitized solar cells: probing the photovoltaic structure-function relation"* - E. J. W. Crossland, D. Corbett, **M. Nedelcu**, C. Ducati, S. Ludwigs, M. A. Hillmyer, U. Steiner and H. J. Snaith, **Submitted to Nano Letters**, 2008

Conferences

- *"Block-copolymer directed mesoporous TiO_2 for solar cell applications"*, Materials Research Society (MRS), Boston, USA, November 2007 - Poster
- *"Pattern formation in polymer films"*, PolyFilm Meeting, Mulhouse, France, September 2006 - Oral presentation
- *"Direct patterning of metals and ceramic materials using e-beam lithography and soft lithography"*, ICN+T Nanoscience and Technology, Basel, Switzerland, August 2006 - Poster
- *"Soft lithography of hard materials"*, IRC Summer School, Tsukuba, Japan, July 2006 - Oral Presentation
- *"Structure formations from polymer based ceramic materials"*, Bayreuth Polymer Symposium, Bayreuth, Germany, September 2005 - Poster